CHALMERS
UNIVERSITY OF TECHNOLOGY

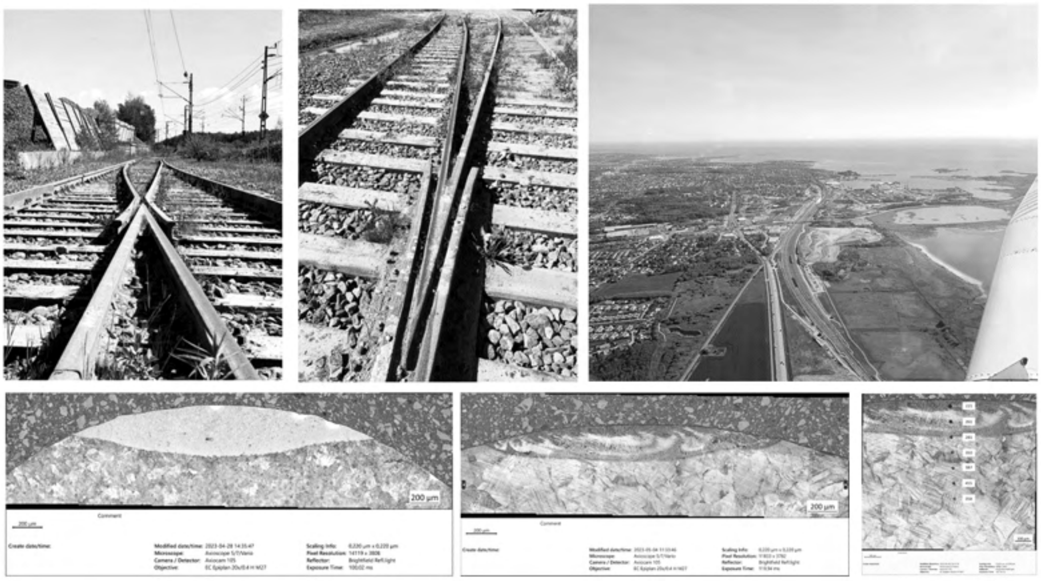

Formation and characteristics of white etching layers on austenitic steels

An experimental study and evaluation of hardness distribution and changes in the microstructure for austenitic manganese steel with associated comparison of pearlitic steel.

Master's thesis in Materials Engineering

CAROLINE ANDERSSON

Department of Industrial and Materials Science
CHALMERS UNIVERSITY OF TECHNOLOGY
Gothenburg, Sweden 2023

Master’s thesis 2023:26

Formation and characteristics of white etching layers on austenitic steels

An experimental study and evaluation of hardness distribution and changes in the microstructure for austenitic manganese steel with associated comparison of pearlitic steel.

CAROLINE ANDERSSON

Department of Industrial and Materials Science
Division of Engineering Materials
Chalmers University of Technology
Gothenburg, Sweden 2023

Formation and characteristics of white etching layers on austenitic steels
An experimental study and evaluation of changes in the microstructure for austenitic manganese steel with associated comparison of pearlitic steel.
CAROLINE ANDERSSON

Supervisors: Prof. Johan Ahlström, Lic eng Erika Steyn Industrial and Materials Science, Prof. Anders Ekberg Mechanics and Maritime Sciences.
Examiner: Prof. Johan Ahlström, Industrial and Materials Science.

Master's Thesis 2023:26
Department of Industrial and Materials Science
Division of Engineering Materials
Chalmers University of Technology
SE-412 96 Gothenburg
Telephone +46 (0)31-772 1000

Cover: Formation and characteristics of white etching layers on austenitic steels. Chalmers University of Technology®. Retrieved 20-02-2023

Typeset in LaTeX
Printed by Chalmers Reproservice
Gothenburg, Sweden 2023

Formation and characteristics of white etching layers on austenitic steels. An experimental study and evaluation of changes in the microstructure for austenitic manganese steel with an associated comparison of pearlitic steel
CAROLINE ANDERSSON

Department of Industrial and Materials Science
Division of Engineering materials
Chalmers University of Technology

Abstract

Transport by train for passengers and for industrial logistics require advancements on the maintenance and demand a deeper understanding of the damages that influence the railway system. Railways experience significant mechanical and thermal loads at the wheel and rail interface, which demand materials with high durability and to prevent failure mechanisms. While fine pearlitic steel (R260) is the predominant material used in Europe, certain areas such as switches and crossings *S&C* employ alternative materials like Mn13, Hadfield steel, or bainitic steel to withstand high dynamic impact.

By examining the microstructural changes and hardness variations in these railway steels, this study contributes to a deeper understanding of the effects of mechanical deformation and thermal exposure in the wheel and rail interface. These findings can provide information to improve maintenance strategies aimed at preventing failures and increasing the lifetime of railway systems.

This project aims to characterise the microstructural changes and evaluate the hardness properties of two railway steels, R260 and Mn13, in the heat-affected region. By subjecting the materials to mechanical deformation and thermal pulses, this study seeks to gain insights into the damage interactions that may occur at the wheel and rail interface.

The result confirms that R260 steel transforms to martensite, forming a thin layer known as a white etching layer (WEL) at the surface after thermal pulses. The rolled austenitic manganese steel instead remelts and forms a layer with a combination of dendrite and columnar structure, similar to cast or welded Mn13. Notable observations include the increased presence of segregated carbides along the heat-affected zone, grain boundaries, and solute accumulation in between the dendrites.
Microhardness and microstructural evaluations were conducted on both untreated bulk materials and those subjected to deformation and thermal exposure. In the thermally exposed region, the R260 steel shows an increase in hardness, while the hardness instead decreases in Mn13. Insights into what affects the hardness and why the microstructure changes are presented in the report.

Keywords: White etching layers WEL, austenitic manganese steel, Mn13, phase transformation, railway steel, microstructure, hardness

Acknowledgements

I am indebted to the incredible individuals who have been involved and have played a crucial role in advancing this work. I would like to express my gratitude to Ove Wahlbeck for generously allowing me to conduct heat treatment on my samples at Alpha Laser. I would also like to extend my thanks to Alf Johansson for taking the time to accompany me on a study visit along the railway, providing valuable insights into the practical aspects of railway construction and maintenance. A special acknowledgment goes to Antonio Mulone for his exceptional training on the equipment in the material lab. I am extremely grateful to have had Johan Ahlström as my examiner and supervisor. Your presence within the academic field has been a great inspiration, and your remarkable ability to explain and guide students has been truly invaluable. I would like to express my gratitude to Voestalpine for providing me with samples of damaged field components. Your provision of these samples has allowed me to gain invaluable insights into the nature of real damage and its impact. Comparing real damage to experimental damage has provided a deeper understanding of the subject matter. I sincerely appreciate the time and support you and your team have dedicated to this project. Lastly, I would like to express my sincere appreciation to Erika Steyn for her absolutely outstanding supervision. Your involvement, unwavering support, and dedication throughout the entire project have meant a lot to me. The guidance and assistance you provided will have a lasting impact on my personal and professional journey.

The work is part of activities within the Centre of Excellence CHARMEC, `http://www.chalmers.se/charmec`. Parts of the study is funded within the European Union's Horizon 2020 R&I programme in Shift2Rail project In2Track3 under grant agreement No. 101012456 and in the Europe Rail project IAM4RAIL under grant agreement No. 101101966.

Caroline Andersson, Gothenburg, 38 2023

Contents

List of Figures

List of Tables

1

Introduction

In railway operation, thermal loads by frictional heating causes temperatures that reach close to the melting temperature. Mechanical loadings by impact causes both accumulation of plastic strains, and impact loadings with high local stresses and strains. This study will examine the phenomena that occur when austenitic high manganese steel and pearlitic steel is subjected to both impacts.

Trains are widely utilised for transportation purposes, including freight trains, for various industries. To ensure reliable operations and extend the service life of railways, proper maintenance is crucial to preventing failure mechanisms. Existing rails are exposed to varying types of loads and temperatures, which force the material to undergo a metallurgical transformation. Different types of damaging mechanics can be found, rolling contact fatigue (*RCF*) or wear and plastic accumulated deformation for instance. These failure modes are particularly common within railway systems [1].

The primary material employed in railway tracks is pearlitic steel (R260), which exhibits sensitivity to both thermal and mechanical loads. However, due to its relatively low fracture toughness, it may not be the optimal choice for switches and crossings (*S&C*) components that experience high dynamic impacts. Although R260 is occasionally used in these applications, a more advantageous option is austenitic high manganese steel, also called Hadfield steel. This type of steel offer superior impact toughness and work hardening properties [2].

One way to prevent failure and increase the lifetime of railways is to develop knowledge of the materials. In this report, changes in microstructure, and their hardness distribution in the heat-affected region are analysed for two typical railway steels, austenitic manganese steel (*Mn13*) and fine pearlitic steel (*R260*).

Frictional and mechanical loads from acceleration, deceleration, and sliding, between the wheel and rail give rise to local thermal shock. At this temperature, pearlite ($\alpha + \beta$-phase) transforms to austenite (γ-phase). Due to the short time of contact between the rail and wheel, self-cooling occurs immediately after passage due to a large temperature gradient between the surface and the bulk material. The high cooling rate will lead to a layer of a martensitic structure defined as a white etching layer (*WEL*) [3]. A WEL can be visible at the surface when thermal impact and rapid cooling occur, this phenomenon gives rise to new mechanical properties. There are two hypotheses on how the WEL occurs, one originates from repeated plastic deformations, which lead to increased strain in the cementite at the same time as grain refinement takes place, referred to as a nanocrystalline microstructure. The other hypothesis is phase transformation due to heating and rapid cooling. How these hypotheses interact is still unknown [4]. The wheel-rail interface experiences a unique combination of mechanical and thermal stresses, which affects the understanding of why a failure has occurred and it can be difficult to identify the cause. This is because the surface is gradually modified by the loads and exposed to temperature changes [5] and the pressure between the wheel and rail decreases slightly the austenitic temperature [6]. The WEL is estimated to be 20-100 μm in thickness and the hardness varies in the range of 700 to 1200 HV [7]. Because of the low resistance to crack propagation, the lifetime decreases with a formation of WEL [1].

1.1 Material and alloy composition for railway systems

Railway steels in the running rails are often a type of pearlitic steel. In Europe R260 is common, which is a fine pearlitic steel [1]. In turnouts, manganese steel or bainitic steel are often used. There are different grades of high manganese steel, Hadfield steel, and Mn13 are two examples. Both of them contain a high percentage of manganese. The specimens examined in this report consist of a composition declared in table 1.1. All values are specified in weight percent [wt%].

Table 1.1: Main alloying elements [wt-%] for pearlitic and manganese steel balance with Fe [1]

Material	C	Cr	Si	Mn
R260	0.76	0.04	0.20	0.93
Mn13	1.14	0.18	0.36	12.25

Pearlite is a two-phase structure consisting of lamella of ferrite and cementite. It has an interlamellar spacing of 100-150 nm with a colony size of 10 μm. Manganese steel consists of austenite, which is a single phase, in comparison, manganese steel has a grain size up to 500 μm [8].

1.2 Problem description and aim

The objective of this project is to analyse the susceptibility of Mn13 and R260 to microstructural alterations under the influence of combined mechanical and thermal loads. The primary aim is to assess and characterise the behavior of the steel in both deformed and non-deformed states, focusing on the distribution of hardness and evaluating any changes in the microstructure. The goal is to gain insights into the effects of thermal heating on both non-deformed and deformed materials.

The main research questions are:

- Is Mn13 prone to microstructural change after the mechanical and thermal impact?

- Does recrystallisation occur in Mn13 and are there any associated changes?

- How do R260 and Mn13 respond to the same type of initiation of deformation and heat treatment?

- How does the hardness distribution of Mn13 and R260 change after mechanical and thermal impact?

2

Theory

The upcoming chapter provides essential information to facilitate understanding and interpretation of the results. It encompasses the equations employed for interpreting the data generated from the experiments. Furthermore, it incorporates equations that derive and elucidate the phenomena necessary for interpreting the information. The theoretical section presents previous studies conducted on Mn13 and R260, along with an exploration of how prior research has addressed the behavior of these materials which can be relevant to interpret the result provided in this project.

2.1 Railway geometry and material application

The project includes an investigation of fine pearlitic steel used as a common rail material and Mn13 used in turnouts. The term switches and crossings (S&C) is often used as a general term for curved rails which includes different parts, in some cases the terminology *turnout* is used instead, but both are referred to the same components. In a turnout, it is common to use high-manganese steel for example Mn13, since it provides lower contact force compared to maraging steel. This is because manganese steel has higher adaptability, and the material is favorable since the material in turnouts needs to withstand plastic deformation and wear, to lower the maintenance cost [9]. R260 steel is used as a common rail defined as *running rails* or just rail. Below there are figures describing the different parts, where figure 2.1 *a*) shows a turnout and *b*) shows a crossing nose. In perspective, a freight railway is shown in figure 2.2.

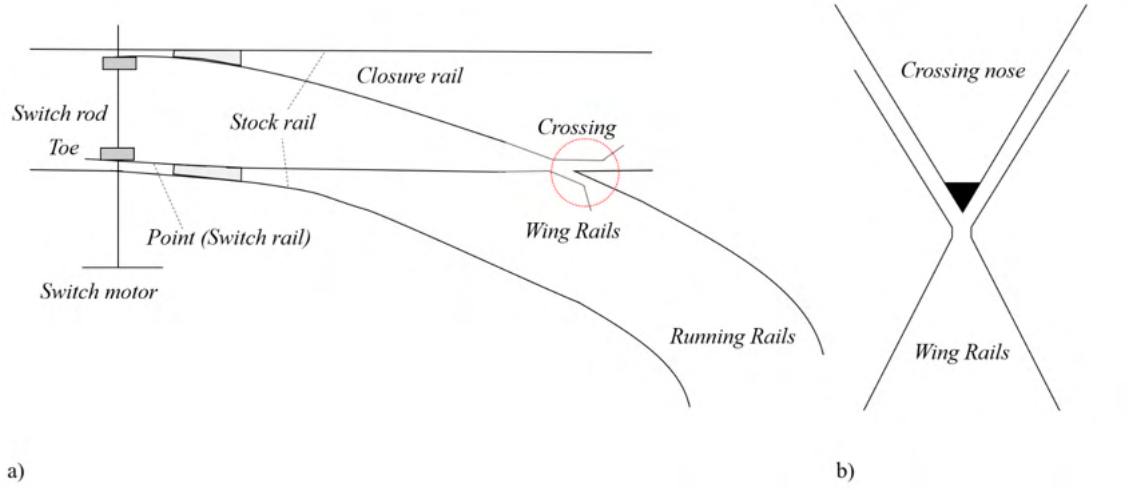

Figure 2.1: a) Turnout components b) a crossing nose

Figure 2.2: Field example of a) a turnout and b) a crossing nose from a freight railway located outside Gothenburg

2.1.1 Theory of contact mechanics

Hertzian theory describes a simplified model of the contact between rails and wheels and can be used to describe the contact forces created between the components [10]. It is based on rolling-sliding conditions between the components and describes normal and tangential load [11]. Because the contact between these components can give rise to thermal shock due to friction and mechanical loads from acceleration, deceleration, and sliding these conditions can have an unfavourable impact on the microstructure [1]. The theory is based on assumptions regarding the profile of *wheel-rail* contact, it is stated to be *constant*. The contact at the interface is assumed to be an ellipse, with a pressure profile of a semi-ellipsoid [10]. To establish the theory the surface needs to be *flat and smooth, with no friction. The stiffness of both components needs to be equal; the material is ideal elastic and the contact area in relation to the profile needs to be small* [11]. Figure 2.3 shows an illustration of the wheel-rail profile, where the lower image shows the rail in profile.

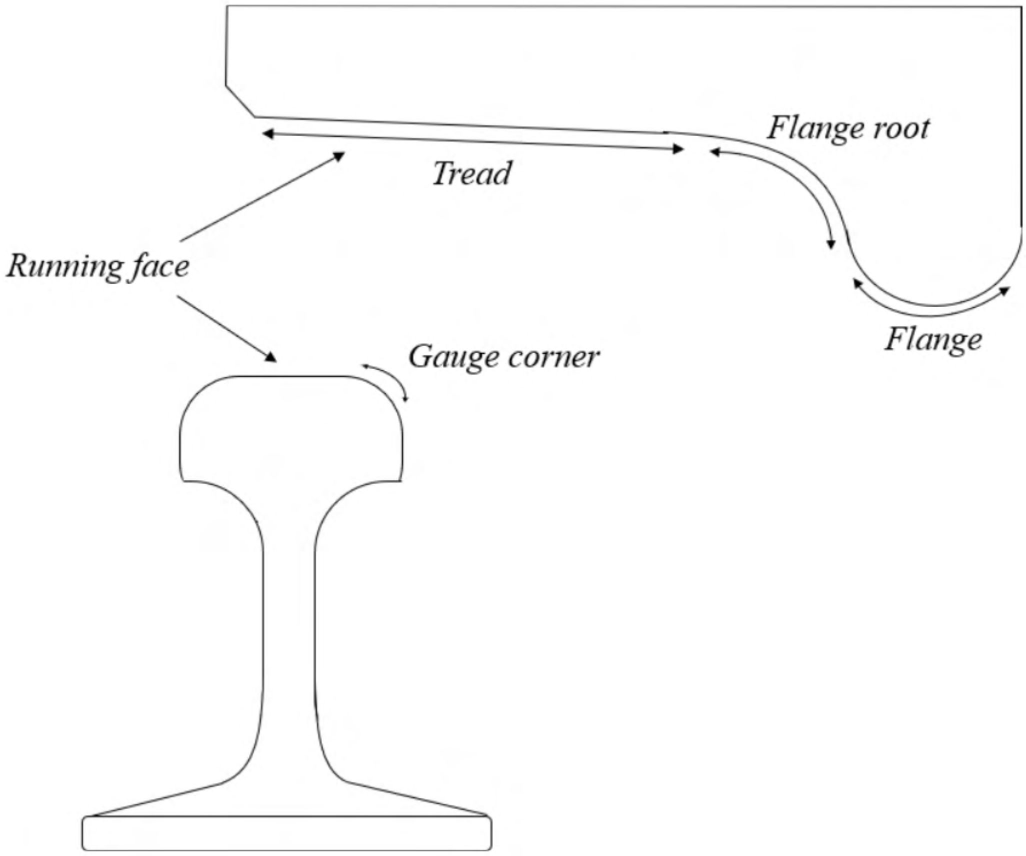

Figure 2.3: The wheel and rail profiles respectively

2.1.2 Sliding wear behavior of Hadfield steels

During sliding on manganese steel, the relationship between force, wear rate, and surface oxide has been studied by analysing mass losses after friction induced by force and velocity. With increased load and increased wear rate, the oxide on the surface of the manganese steel increases. However, this is only valid to a limited value of the force. After a limit value has been received, the mass loss starts to decrease. A decrease in mass loss represents a higher force which increases plastic deformation, adhesion, and abrasion at the oxidation layer [12].

When the oxide layer is destroyed or worn, the contact between the wheel and rail increases. After a while, the oxidation layer forms again but will be uneven on the surface. It could also establish that martensite arises in the manganese steel due to the force applied, which confirms that manganese steel can undergo a phase transformation via friction-induced wear [12].

2.2 Microstructure development and phase transformations

Phase transformation refers to the process in which one phase transitions into another. A phase, as per its definition, represents a homogeneous system with similarities in both properties and chemical composition. Thermodynamics provides a useful framework for describing phase transformation, as the system aims to achieve a state of stability. In metals and alloys, the objective is to minimise the Gibbs free energy, which characterises the relationship between enthalpy H, Entropy S, and temperature T, as depicted in equation 2.1 [13].

$$G = H - T \cdot S \tag{2.1}$$

A phase transformation is when the crystallographic structure changes, and corresponds to lattice changes as well as the properties of the material. It depends on temperature, time, and cooling rate [14]. Temperature makes it easier for grain growth, diffusion, and dissolution of carbides. Time and temperature give accommodation for grain growth and diffusion. The cooling rate decreases the ability for diffusion and designates the final microstructure [15].

Within phase transformation, terms such as Gibbs free energy, energy barriers, and stable and metastable phases are used. Generally, this means that a material strives to obtain the lowest possible free energy, which influences the material to diffuse under solid conditions to lower the free energy. A metastable phase is a locally stable phase, for instance martensite. The energy barrier or activation energy describes the extra energy needed for a transformation to take place.

As previously stated that defects, like dislocations, have an influence on phase transformation, for nucleation; of the martensitic phase, dislocations provide heterogeneous sites for nucleation to grow, since dislocations provide interaction energy that lowers the transformation, see equation 2.2 [14]. Where $V\triangle G_v$ is the volume free energy release, $A\gamma$ is the free energy increase, $\triangle G_{strain}$ interfacial strain, and $\triangle G_{dislcation}$ is the dislocation interaction energy.

$$\triangle G = -V\triangle G_v + A\gamma + V\triangle G_{strain} - \triangle G_{dislcation} \tag{2.2}$$

2.2.1 Crystallographic structures and its planes

Metals are crystalline materials that obtain a crystal lattice with their atoms. The atoms are placed on defined planes. The plane of the unit crystals is defined based on *Miller indices*, namely (h, k, l)-indices where the [100] direction is the side faces of the crystal [16]. The lattice of solid metals acquires an almost fixed position in relation to each other. When similar crystals are repeated, a three-dimensional lattice is formed, called a space lattice. When the crystals grow in the same direction, a grain is created. Where two differently oriented crystals meet, a grain boundary (*GB*) is formed. The type of crystal a metal consists of primarily determines its behaviour. Face-center cubic (*FCC*) has more active slip planes and provides a greater opportunity for ductile properties. While a hexagonal-close-packed (*HCP*) crystal offers little or no ductility [17].

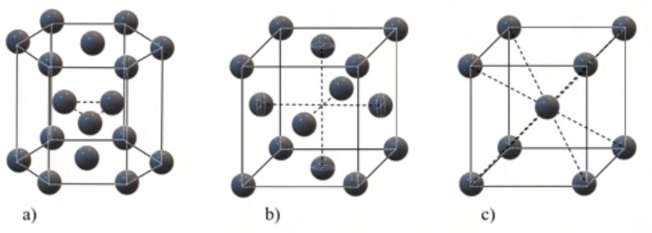

Figure 2.4: Different types of unit cells a) HCP b) FCC c) BCC

Common crystals are FCC, body-centered cubic (*BCC*), and HCP. Crystallography describes the location of atoms, sliding system [18], and this influence mechanical properties such as yield strength, ductility, and hardness varies. Stiffness is independent and almost unchanged [8].

Crystal planes are determined where the atomic density is high. By using Miller index notation, a plane can be described with three or four crystal axes, which originate from the origin in cartesian coordinate system. The negative direction is described as an integer with a dash above it; $[\overline{111}]$ is the opposite of [111], for instance. FCC contains four atoms, BCC contains two, and HCP a total of 6 atoms per unit cell. Each unit cell corresponds to an atomic coordination and describes the number of nearest neighboring atoms, where both FCC and HCP is equal to 12 and BCC only 8. The crystallographic analysis defines how a crystal is deformed if it is exposed to stress and its ability to store residual stresses within the metallic structure [19]. A crystal system describes the symmetry of the unit cell, where *a,b* and *c* are the scalar magnitudes and α, β and γ describes the angle, see table 2.1[20].

Table 2.1: Crystal systems

Crystal system	Unit cell size	Unit cell angles
Cubic	a=b=c	$\alpha = \beta = \gamma = 90°$
Tetragonal	a=b≠c	$\alpha = \beta = \gamma = 90°$
Hexagonal	a=b≠c	$\alpha = \beta = 90°, \gamma = 120°$

2.2.1.1 Stacking fault energy

Stacking fault describes an interruption of the closed-packed planes. This interruption gives rise to stacking fault energy (*SFE*). When there are stacking faults in the close-packed plane of the crystal, dislocation glide is affected, which affects the properties of the material [21]. This type of interruption is described as a planar defect that arises due to voids between atoms. Since the atoms are placed on top of each other, some voids between the layers generate interruptions in the stacking pattern. Figure 2.5 *a*) shows a typical FCC pattern (*ABC*-*ABC*), but in *b*) interruptions in the pattern are visible, (*ABC*-*ABA*). This mistake creates a stacking fault. This interruption can only be formed in closed-packed systems and occurs due to grain growth or dislocation movement. Metals that are prone to produce this interruption in the pattern, are said to have a low SFE. In general, SFE is related to the surface energy, corresponds to the width of the interruption, and acts opposite to the dislocation energy [22].

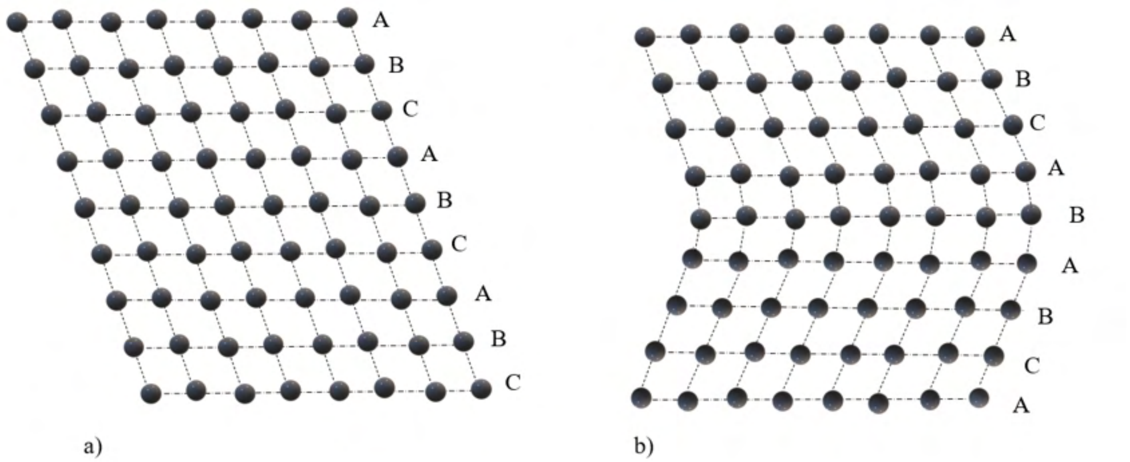

Figure 2.5: a) A perfect crystal, b) stacking fault

2.2.1.2 Diffusion

Interstitial and substitutional diffusion are processes that describe the movement of atoms within a metal lattice, known as *atomic mobility*. In interstitial diffusion, small atoms can easily find available sites to diffuse into, facilitating their movement within the lattice. On the other hand, substitutional diffusion requires vacancies and significant oscillation for atomic movement to take place [13]. This phenomenon is depicted in figure 2.6.

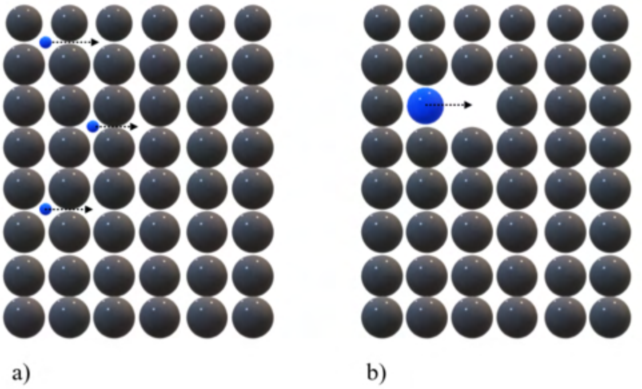

Figure 2.6: a) Interstitial and b) substitutional diffusion

2.2.2 Austenite

Austenite is a solid phase in steel that remains stable at high temperatures. Its crystal structure is FCC, and it is commonly denoted as γ-phase. The grain size of austenite is influenced by time and temperature, with larger grain sizes observed at higher temperatures; <A_3. The grain growth in austenite is controlled by a phenomenon known as the "pinning effect." This phenomenon occur when solutes or alloying elements hinder grain growth by impeding their movement.

Austenite exhibits high ductility due to the presence of multiple slip planes in its FCC crystal structure. It is typically obtained in the upper temperature range, as it tends to be more thermodynamically stable compared to other phases under such conditions. However, there are exceptions where austenite becomes a stable phase at lower temperatures. This occur during the process of solution hardening, which involves the addition of high concentrations of nickel or manganese to the steel. In such cases, the resulting steel exhibits good ductility and toughness as it can leverage the slip planes within the FCC crystal structure.

The concept of "prior austenitic grains" is often used as a reference to describe the size of grains in austenite at elevated temperatures. When martensite is formed, these prior grains can be identified because martensitic grains only grow within the boundaries of the prior grain, without crossing over to neighboring grains[23].

2.2.3 Martensite

Martensite is a hard phase that forms in steel when it is heated to the austenitisation temperature and then quenched rapidly. The formation of martensite is characterised by athermal kinetics, meaning that no thermal activation is required for the phase transformation to occur. Quenching, which involves rapid cooling, limits the time for atomic diffusion, resulting in a diffusionless phase transformation.

In steel, martensite formation occurs when the starting microstructure is austenitic, and the rapid cooling prevents diffusion. As a result, the composition from the austenitic phase is retained in the martensite, and carbon is trapped in the octahedral sites of the BCC crystal structure. Since BCC cannot fully dissolve all the carbon, a distorted crystal structure known as body-centered tetragonal (BCT) is formed, leading to changes in the distance between lattice parameters c and a. The tetragonality of the structure is influenced by the carbon content and can only be relieved through reheating. At a certain temperature, carbon atoms can diffuse into the material and replace the martensitic phase with ferrite and cementite (Fe_3C) due to the instability of the martensitic phase. The characteristic structure of martensite is often described as acicular or needle-like, with elongated and thin crystals, exhibiting unique crystallographic features [24].

The total formation of martensite can be impossible to achieve. The phases will then be a mixture of martensite and retained austenite. This is because martensite is formed depending on the alloying elements with a large influence of the proportion of carbon. This is usually described by Andrews equation, see equation 2.3 [25].

$$M_s(\circ C) = 539 - 423(C) - 30.4(Mn) - 12.1(Cr) - 17.7(Ni) - 7.5(Mo) \tag{2.3}$$

2.2.3.1 Morphology of pearlite

Pearlite is a two-phase microstructure consisting of ferrite (Fe) and cementite (Fe_3C) that grow into alternating lamellae, as depicted in figure 2.7. The formation of pearlite occurs through an eutectoid reaction during the cooling process from austenite. This can be achieved through either isothermal cooling or continuous cooling methods. In the case of isothermal cooling, the transformation of austenite takes place at a constant temperature over a specific period of time, often represented by a time-temperature-transformation diagram (*TTT-diagram*). Continuous cooling, on the other hand, involves a continuous decrease in temperature to transform the austenitic phase into a pearlitic structure.

Both isothermal and continuous cooling methods result in the formation of nodules and pearlite colonies, which are characterised by alternating lamellar structures. The interlamellar spacing within the pearlite microstructure is influenced by the cooling rate, either increasing or decreasing depending on the rate [26]. A continuous cooling transformation is also a way to control the pearlitic structure [27]. The interplay between cooling rate and interlamellar spacing has an impact on the final microstructural characteristics of the R260 steel. Both the CCT and TTT diagrams for R260 steel are illustrated in appendix A figure A.1.

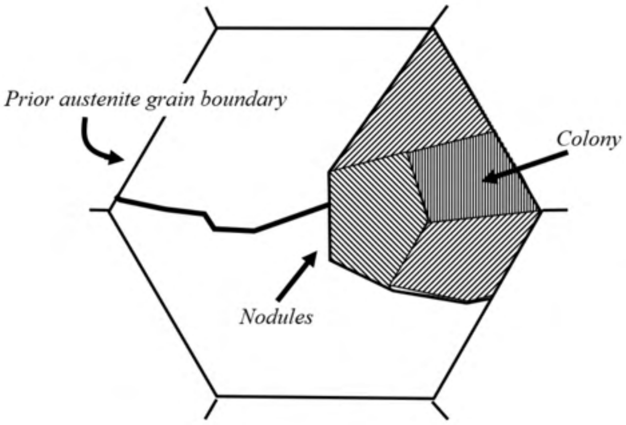

Figure 2.7: The morphology of Pearlite; black lines within the colony is Fe_3C and white is Fe

2.2.4 Pearlitic R260 steel

The mechanical properties of R260 steel are influenced by the manganese and carbon content, as they play a role in determining the pearlitic morphology. Carbon content contributes to dispersion strengthening and affects strain hardenability, while manganese influences the eutectoid composition and serves as a solid solution hardener, controlling grain growth [28]. Pearlite formation follows isothermal kinetics and occurs when the temperature decreases below the A_1 temperature with respect to time [24].

2.2.5 Austenitic manganese steel

Austenitic manganese steel is known for its good impact toughness and work-hardening which make it suitable for various industrial applications, such as railway, mining, construction, and military applications [2]. But because of its high properties in terms of ductility, wear-resistance, and strength, affect the possibility of good machinability, and the material is classified as difficult to machine [29].

In S&C materials with high resistance to dynamic impacts must be used, which means that the material must obtain high toughness, making austenitic manganese steel or Hadfield steel a more advantageous option. This steel is often produced via monoblock casting. The manganese in the steel makes the austenitic phase stable at lower temperatures [30], which means that the advantages of the FCC crystal in terms of toughness can be used [23].

Carbides are often accumulated in this material. This has been proven if the material is aged, where carbides forms along the GB of Mn13 [31] [32]. This affects the material negatively, as the carbides are brittle and reduce toughness. Carbides are also formed during welding which makes the material difficult to process. If the material is welded, the risk of forming carbides increases.

Another weakness that can be found in the assembly of Mn13 to other steels, since Mn13 expands significantly more than for example R260. Mn13 has a 60% higher thermal expansion coefficient than R260. To join R260 and Mn13, a thin layer of stainless steel is used in between, due to the poor weldability of Mn13 [30].

Figure 2.8: Weld between turnout and rail from a freight railway located outside Gothenburg

2.2.6 Cast and rolled high manganese steel

There are two ways of producing high manganese steel, namely cast or rolled. Independent of the method, the end result will still be an austenitic phase. To ensure that the material gets the right properties at the end, both need to be annealed and quenched in the last step. Cast Mn13 is primarily used in crossing noses and rolled Mn13 is primarily used for rails connecting the S&C. The grain size differs between the methods, where the rolling process results in larger grains. Casted materials are also characterised by a greater proportion of pores. The hardness varies between 340-480 HV for rolled Mn13 [33].

Mn13 presents difficulties for casting, as it acquires properties that complicate the process. For example, Mn13 obtains a high coefficient of thermal expansion, which makes the process more difficult. The expansion depends on the high percentage of alloying elements. However, this is not the only reason for difficulties in processing, Mn13 also exhibits a slow solidification rate. Due to these properties, Mn13 has a tendency to solidify and form a dendritic structure where solutes segregate and accumulate between the dendrites. With this obtained structure, the quality of the material decreases and the good properties of Mn13 are no longer present. It is common to grow dendritic grains in cast austenitic high manganese steel. For continuous slab casting, a casting speed of 0.9 m/min was reported to avoid excessive dendrite formation and instead obtain a higher proportion of equiaxed grains [2]. Phase transformation for Mn13 are attached in appendix A figure A.2 it describes the relationship described in section 2.2.3.1. The diagrams should correspond to which phase is formed in Mn13 depending on whether isothermal or continuous cooling is performed.

2.3 Laser heating

Laser welding has been used in earlier investigations to produce an experimental martensitic microstructure on pearlitic R-260 steel. This technique can be used for experiments to create a uniform starting condition. Calculation of heat input [*J/mm*] can be calculated with the following equation, see equation 2.4. The quantities are welding current [*A*], arc voltage [*V*] which can be replaced with applied power in watt [*W*], and travel speed in [*mm/s*].

According to the convention in equation 2.4, the speed of the scan determines the outcome of heat input, as higher speed reduces heat input and vice versa. An increase in heat input generates a larger area where the material is affected by heat and a greater chance of being transformed [34].

$$Heat\ input\ [\frac{J}{mm}] = \frac{Applied\ power\ [W]}{Travel\ speed\ [\frac{mm}{s}]} \tag{2.4}$$

In addition to the area that is directly exposed to heat input, the surrounding area is also exposed, through thermal conductivity. Metals are conductive and heat is easily spread by conductivity, Fourier’s law describes how the heat is spread in the nearby area via an expression based on how heat spreads from high to low temperature. Where q is the heat flux in *[W/m^2]* in uniform with convenient *x, y, z* for direction, k the thermal conductivity, and T the temperature [35].

$$q_x = -k \cdot A \cdot \frac{dT}{dx} \tag{2.5}$$

$$q_y = -k \cdot A \cdot \frac{dT}{dy} \tag{2.6}$$

$$q_z = -k \cdot A \cdot \frac{dT}{dz} \tag{2.7}$$

Heat flux can be rewritten as a vector denoted by the temperature gradient instead, see equation 2.8

$$\overrightarrow{q} = -k\overrightarrow{\nabla} T \tag{2.8}$$

2.3.1 Welding theory

According to the definition of laser welding, the bulk material is melted and undergoes a phase transformation from solid to liquid state. When the laser source is removed, the material transforms back to a solid state. Laser welding can be performed either as a continuous weld or as single spots. Laser stands for *Light amplification by stimulated emission of radiation.* There are two ways to achieve different welds produced by a laser; *conduction welding* which is based on conductivity and realises heat to the bulk material, or by *deep penetration keyhole* which corresponds to a hole in the bulk material, which penetrate the walls of the hole, movement of the heat source will force the liquefied material to solidify [36]. The heat-affected zone (*HAZ*) is the region from the fusion line out to the bulk material, this is shown in figure 2.9. This is an area that has not been heated enough to undergo a phase transformation but due to the heat conduction, it receives enough energy to change the microstructure compared to the bulk material, for instance, grain coarsening, grain refining and recrystallisation.

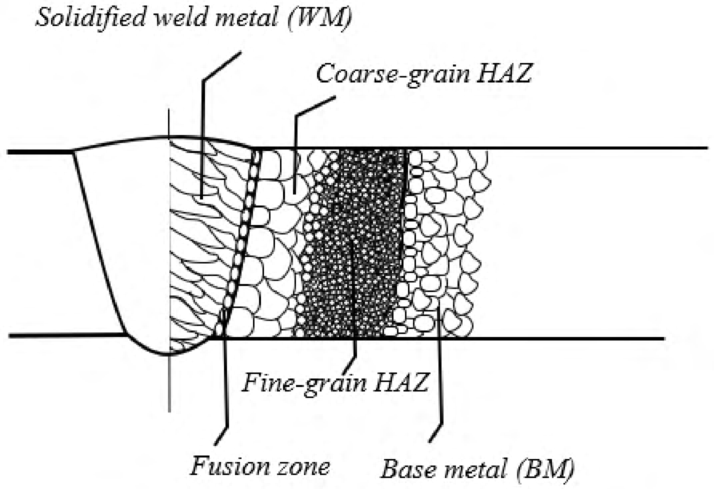

Figure 2.9: Welding theory, provided by WM, fusion zone, and HAZ

Laser focus energy via a nozzle, the type of laser depends on the desired result of the weld. The most common is a laser provided by carbon dioxide CO_2, depending on the source, altering results of the laser beam and wavelength will arise. For a CO_2 source, the wavelength is in the infrared spectrum. What characterises welds produced by the laser is the size of the weld and its impact on the surrounding area. The nozzle is not in contact with the metal piece, since the laser beam emits energy through the air. Via neodymium: yttrium-aluminum yarn *Nd:YAG*, the laser beam is carried out via fiber optics. Like other methods, laser welding requires shielding- or inert gas to prevent oxidation.

Laser welding is narrow and can penetrate deep into the metal piece. The heat source in a laser is considered to be low or lower compared to other methods, this indicates that the area around the weld will be less affected in relation to other methods, the speed of the laser beam's movement is also faster, with a speed of 5-10cm/s compared to 2 -3 cm/s from other methods. This means that the heat-affected zone *HAZ* becomes smaller for laser welding [37]

2.3.2 Weld solidification

Steels can contain different alloying elements, but similarities in the solidification structure can be found for pure steel. During solidification, columnar grains will most likely grow from previous grains in the bulk material closest to the liquid phase at the fusion zone. This is referred to as epitaxial growth. Since the grains grow in the same direction as the parent grains at the fusion line, anisotropy will occur. The growth takes place in the same direction as the heat flow. Grains that have their growth direction in the <100> direction as well as parallel to the direction of the heat flow, will have faster growth. These grains will ultimately have a wider grain in the final stage extended away from the fusion line [38].

2.3.3 Dendrite growth

Dendritic grains are a common structure observed in welds or cast materials, resulting from the solidification of metallic materials. During this process, there exists a significant temperature gradient between the phases, leading to the nucleation of crystals. These crystals exhibit a distinct characteristic as they grow in the opposite direction to the heat flow, forming elongated grains, similar to columnar grains. The temperature gradient plays a crucial role in determining the resulting structure. Lower temperature gradients lead to the formation of equiaxed grains [39]. This is reflected on a study where high manganese steel was subjected to laser remelting. The structure became a mixture of superficial equiaxed, internal columnar grains and carbon and oxygen that segregated to the dendrites [40].

What characterise dendrites is the special shape, see figure 2.10, where dendrite arms and tipp are illustrated, this is often referred to as a branched shape. It allows it to grow into the liquid phase due to constitutional supercooling. During solidification solute atoms or concentration in the liquid phase will increase [41]. Dendrites formation arises due to instability in the system, and there are two common options which can be single-phase or two-phase instability. The single-phase is characterised by the fact that a part has been more constitutionally undercooled, if this occurs dendrites and interdendritic eutectic arises, which causes the growth rate to increase in these parts. In the case of two-phase instability, a cellular structure similar to eutectic colonies is instead created. The type of instability depends on the alloying elements and concentrations of the allowing elements a material contains. Single-phase characteristic occurs if the material contains a binary system. With more substances, two-phase instability is formed instead. In that case, a layer is created between the interfaces of the phases, in this way, they are separated and eutectic colonies can be formed [42].

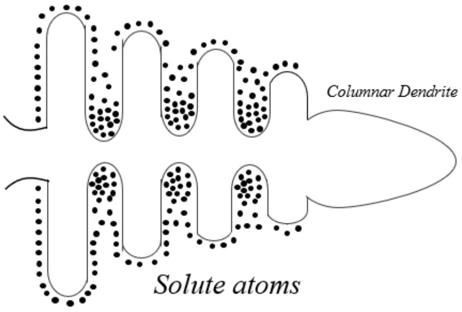

Figure 2.10: Dendrite structure with segregated carbides

2.3.3.1 Dendrite kinetics

Dendrites differ in their growth from other types of grain growth. It is more complex because there are factors that are unknown, for instance, the radius of the tip R of the arms, defined as dendrite tips. The complex growth of dendrites is because growth is a function of the unknown variables. Instead, a numerical function called the *phase field method* can be used to describe the relationship between the radius and the rate of growth v. To fully express the growth of dendrites *capillary length, solute diffusion length, solid-liquid interfacial energy, entropy of fusion, the interval of solidification, and tangent of the liquid surface* need to be known to express the solute gradient of the interface close to the tip. By this convention, the radius can be calculated by *Kurz and Trived formula* [43]. As dendrites grow along a favorable direction in the metal, the mechanical properties will change from the original base metal, it is therefore important to understand the growth such as the length and direction of dendrites to satisfy the component's properties [44]. Below an illustration of the solidification direction and dendrite envelope are declared, see figure 2.11. Modeling of dendrites and its kinetics is omitted from the work.

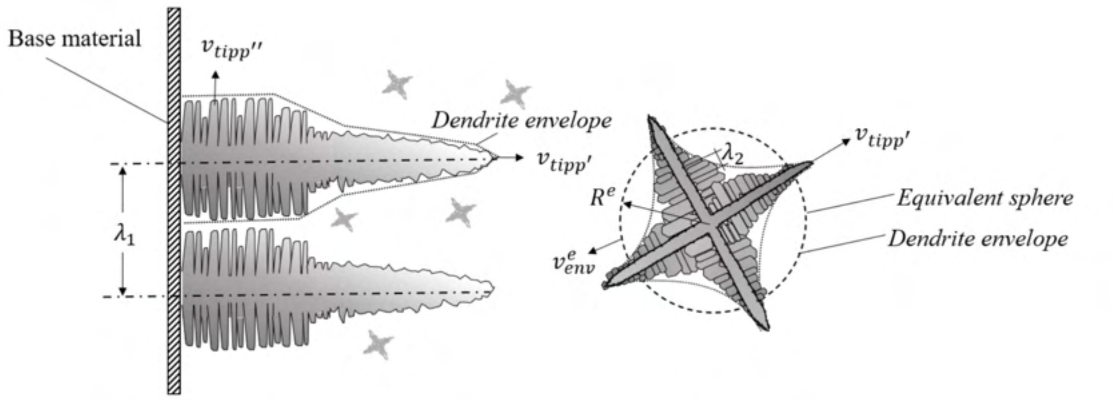

Figure 2.11: Dendrite kinetics and dendrite envalope

2.3.4 Welding defects

There are different types of defects that can occur during welding and the solidification of a weld. The type of defects depends on the welding method and the base material. Hot cracks are common defects that can be found in welds. Between the partially melted zone (*PMZ*) and the HAZ it is common to find *hot cracks.* They occur because the liquid obtains different concentrations of solutes which means liquid can exist even at lower temperatures than the solidus equilibrium temperature. This entails the liquid does not solidify at the same rate as the rest of the weld. To distinguish these cracks, solidification hot cracks at the fusion zone are defined as a crack that occurs due to insufficient solidification, liquation crack occurs at the PMZ and occurs due to reheating or multipass welds. Both of these are hot cracks that occur but for different reasons [45]. See figure 2.12 for an illustration of the different zones.

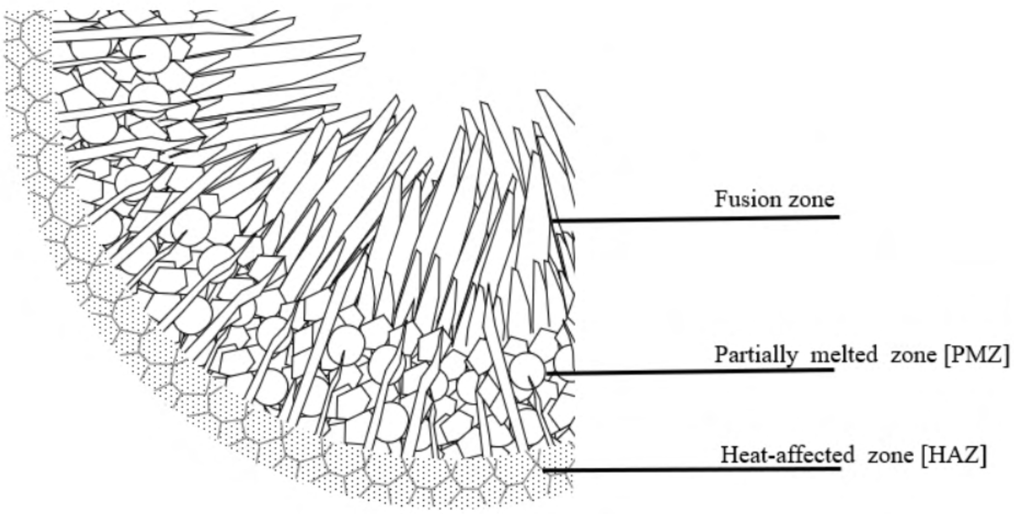

Figure 2.12: Welding theory and general welding structure, and shows the different zones HAZ, PMZ and fusion zone

2.3.4.1 Solidification hot crack

Solidification hot cracks in welding can be observed along the solidification GB. There are two hypotheses of why this type of crack occurs in the solidification of welds. That the crack forms due to shrinkage during solidification, which is referred to as *intrinsic restraint*, where shrinkage occurs due to changes in the volume during solidification [45], which is convenient for altered unit crystals [18]. Apart from the difference in volume, there are differences in the material properties between the phases. The other hypothesis is that cracks occur due to *extrinsic restraint*, which depends on mechanical fixturing. In addition to these, there are also various theories that explain the origin of crack growth in solidified welds, the most common of which are *shrinkage-brittleness theory and strain theory.* figure 2.13; shows how the grains grow together before the weld has been filled by the melt. Right; shows how shrinkage appears in the opposite direction to grain growth or the direction of the solidification [45].

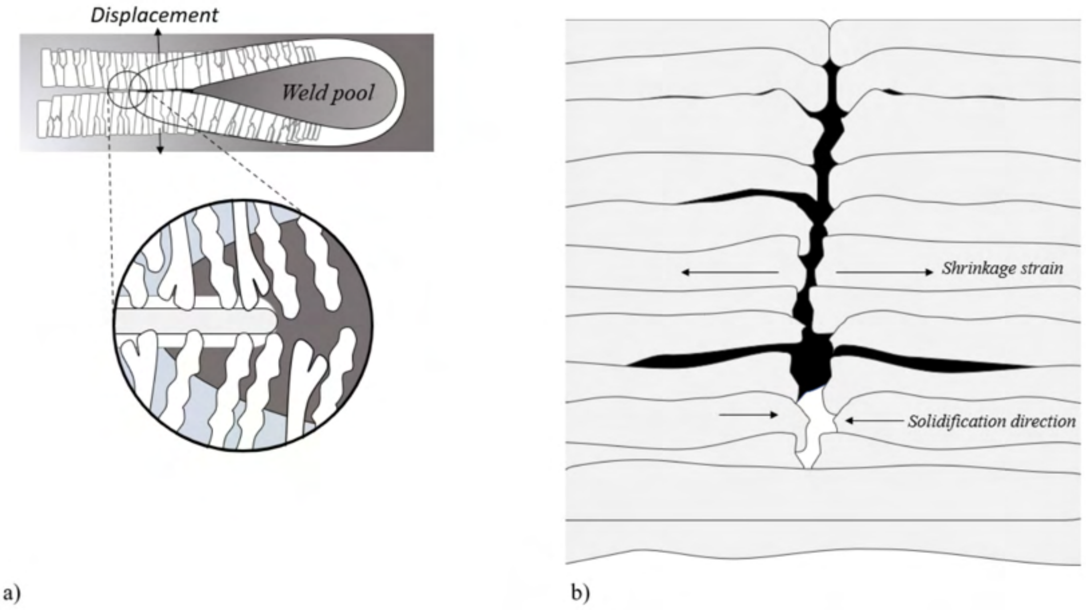

Figure 2.13: Solidification cracks in welding

2.3.4.2 Formation and influence of solidification hot cracking

Solidification hot cracks form during the solidification of welds and are more prone to occur if the metal exhibit poor thermal conductivity and large thermal expansion. These cracks often arise if both welding speed and solidification rate are high, since it proved thermal tensile strain in the remaining liquid [46], This results in shrinkage in the opposite direction to the solidification direction [45]. However, there are additional contributing factors that can lead to this phenomenon. For example, the presence of alloying elements can lower the melting point, making the material more susceptible to hot cracking. Additionally, the formation of micro-cavities within the material serves as a site for initiation of micro-cracks, which can propagate and eventually result in hot cracking as the strain in the material increases. The risk of solidification hot cracks is also more prone to occur if grains or misorientation of grains exhibits high-angle boundaries. The reason why the misorientation influences are because it is related to the liquid film. It is most common to find cracks in a transgranular direction to the welding direction [46].

2.3.4.3 Liquation cracking

Liquation cracks can be observed in the region of the PMZ and HAZ, due to reheating in the form of multipasses or prepared welds. The location of the crack signifies the type of crack. Liquation cracks occur at the solidification grain boundaries or at migrated grain boundaries (*MGB*). The crack appears because the reheating dissolves the old boundaries [45]. Another explanation for the appearance of these cracks is the heating of the material at the interface is above the eutectic temperature, which weakens the grain boundaries in the PMZ. In this scenario, during solidification in the PMZ tensile stresses, and strains are generated, this in turn, leads to the development of visible cracks [47].

2.3.5 Weldability evaluation of manganese steel

It is stated that Mn13 shows poor weldability, due to their high thermal expansion, low thermal conductivity [30], and also for the poor material properties it achieves. During welding high manganese steel forms carbides along the grain boundaries and thermal initiation should be avoided, since it accelerates early failure. In rail-road crossing, turnouts or crossing noses work-hardening by impact loading occur, and the maintenance is performed by grinding and maintaining the components. But sometimes even welding is required, in that case, nickel is added since increased carbon content increases the risk of martensite formation. Distinct levels of alloys have been studied to prevent the weld from becoming brittle. Temperatures below 300°C do not lead to carbide formation. To avoid affecting base material in the near region *arc welding* prevents best maintenance welds [48].

Even in other steels with a comparable high manganese content, subpar welding properties are observed. In such cases, significant attention is placed on the segregation of carbides around the dendritic arms, which contributes to the occurrence of solidification cracks. These cracks are attributed to the specific conditions during solidification. Additionally, these steels may exhibit deteriorated mechanical properties, including decreased ductility [49].

2.3.6 Precipitates and carbides in austenitic manganese steel

Previous studies have provided evidence that mixed carbides tend to accumulate at the GB during the aging process of Mn13 steel. Material homogenisation is achieved at a temperature of 1050 °C. Heat treatment of the material at 475 °C for two hours leads to the precipitation of carbides at the GB. Transmission electron microscopy (TEM) analysis of the precipitates identified them as $(Fe, Mn, Cr)_{23}$ and $(Fe, Mn, Cr)_7$ [31]. The proportion of carbides increases when the cooling rate or solidification rate is slow [32].

Aging between 400 and 500 °C results in a low carbide content, which is temperature-dependent and increases with higher temperatures. At 600 °C, Hadfield steel reaches the temperature for eutectoid transformation, where ferrite (α-Fe) and cementite become visible. The precipitates formed at lower temperatures are mainly composed of M_3C carbides, although there is a lack of research on the crystallographic characteristics under low aging temperature conditions. Normalising and quenching treatments have been found to have no significant impact on the microstructure. However, annealing, tempering, and cold working induce notable microstructural changes. Tempering of Mn13 steel leads to the formation of a fine distribution of carbides, while annealing results in precipitation at and within the grain boundaries. Cold working reveals twin boundaries and compressed carbides that have grown along the previous grain boundaries, martensite in the form of a needle-like structure can also be visible. From X-ray diffraction this is reported as HCP Mn_15C_4 and Fe_3C and γ-Fe [50].

2.4 Thermal damages in railway steel

Thermal damage is common in railway steel and requires maintenance, to avoid increased and unanticipated costs. Maintaining thermal damages can be made by grinding and milling to remove the damages at the surface. The influence of thermal damage is changed mechanical properties, residual stresses, and microstructure degradation. In contact between wheel and rail at the interface between flange and tread, there are elaborated high loads and in this intersection, the frictional forces cause local thermal heating. Thermal damage leads to phase transformation at the surface, called the White etching layer [28].

2.4.1 White etching layer

Friction and mechanical loads caused by acceleration, deceleration, and sliding between the wheel and rails generate local thermal heating when the contact friction gives rise to an increase in the temperature to austenitisation temperature. At this temperature pearlite ($\alpha + \beta$-phase) transforms to austenite, (γ–phase). Because of the short time, the rail and wheel are in contact, self-cooling will occur due to the large temperature gradient. Because of the high cooling rate, this will lead to a layer of a martensitic structure [3].

Several plastic deformations increase strain in the cementite and promote grain refinement, influencing the phase transformation under varying pressure conditions. The presence of higher pressure, combined with elevated temperatures, can accelerate the transformation. The application of pressure results in a slight reduction of the required temperature. A complete phase transformation can therefore be a result of pressure and temperature interacting [51]. The interfacial contact is estimated to be momentary, lasting milliseconds, further limiting the time for transforming more than the surface before self-cooling occurs [4]. Consequently, a white etching layer (WEL) with a thickness of 20-100 μm is expected, exhibiting hardness ranging from 700 to 1200 HV [7].

A WEL is a thin layer of a martensitic structure sometimes defined as nanocrystalline martensite, austenite, and cementite. The WEL consists of martensite with high dislocation density, occasional twins, and cementite particles. The appearance of the WEL can vary depending on factors such as temperature, strain, strain rate, hydrostatic pressure, and cooling rate, as it is influenced by the history of the sample. It is named white because of its appearance in an optical microscope, which makes the phase appears as a white layer. The reason depends on corrosion resistance when it is etched with Nital [5]. The presence of the WEL leads to changes in material properties, such as increased hardness and brittleness. Because of the low resistance to crack propagation, the lifetime decreases [1]. There are also cases where a brown etching layer is visible, which is a consequence of tempered martensite. After martensite has formed tempering under austenitic temperature leads to a brown layer of martensite [3].

The phenomenon of the white etching layer (WEL) can be observed in various components. While the term "WEL" is commonly used in the railway industry, similar phenomena occur in other components and may be referred to by different terms. For instance, in the case of core teeth of cylinder disks used as saw blades, the microstructure observed at the surface is referred to as troostite [52] rather than a white etching layer. Regardless of the specific terminology, these structures are characterised by the presence of a martensitic surface layer formed by thermal increase and rapid cooling.

2.4.2 Influence of oxidation on white etching layers

The interface between wheels and running rails receives high load drops due to acceleration, deceleration, and sliding, often referred to as the contact mechanism. This gives rise to local thermal shock forming WEL on the surface. It has been found that oxidation has great importance since WEL has only been created on oxidised surfaces, however, wear could be observed more clearly on surfaces where oxidation has not occurred [53].

2.5 Hardness testing

The hardness of a material can be determined using various methods and units. The Vickers method is commonly used, but other methods such as Rockwell are also utilised. The key distinction among these methods lies in the indentation process [54], [55].

Hardness can be measured in Vickers, which uses several indentations with a diamond pyramid to decide the hardness of a material. Hardness equates to characterisation in determining the degree of deformation created on the surface of an object when a hard object is pressed against it with a predetermined force. According to the definition, hardness is determined based on the penetration into the surface of a perceived object. A material is said to have high hardness if it can resist the penetration of an object. This can be calculated using A. Marten's expression, see equation 2.9. Where H is the hardness of the test object, F in *[N]* is the force that is predetermined and A is the area in m^2 of the indentation surface [54].

$$H = \frac{F}{A} \tag{2.9}$$

The Rockwell method is a widely used technique for measuring the hardness of materials. It involves penetration of an indenter into the material under controlled conditions. The indenter leaves an indentation mark on the material, and the depth of this mark is used to determine the material's hardness. The Rockwell method utilises either a ball or a spheroconical diamond as the indenter shape. The test procedure involves applying a predetermined minor load, typically around 10 kg, followed by a major load, which can range up to approximately 150 kg [55].

2.6 Mechanical deformations

There are two major ways a metal can be deformed, either elastic or plastic, which indicates a reversible and irreversible deformation. It is a critical value defined as the yield point which separates the two deformations apart, after the yielding the material will either deform plastic or immediately break which corresponds to a permanent deformation [56]. The movement of deformation for plastic deformation can proceed in different ways. [57].

2.6.1 Slip bands

A slip band is visible as a line on a polished surface [58]. The phenomenon comes from the definition of physics of plasticity and is defined as a slip in a crystal due to shear stresses. All crystallographic structures have different slip planes and the slip plane for a given crystal defines the amount of plasticity. When slip bands in a grain increase, dislocation movement decreases and the material decreases its ability to further strain. The initiation of defects increases the accessibility of a phase transformation to occur since the nucleus can grow on defects such as slip bands and dislocations [59].

Slip according to the definition is a plastic deformation that is irreversible and occurs due to shear displacement between two nearby crystals and describes the direction on a specific plane [60]. Slip occurs within the plastic region, which indicates a residual deformation. It occurs either as a slip over a plane or slip over layers of atoms [57]. The direction of slip is according to the definition called slip direction and enables the crystallographic direction of the slip. The direction can be observed in slip bands, which is accumulated closed packed slip lines, and it can be observed as parallel lines in a grain, see figure 2.14 b) [60] The orientation of the slip bands is parallel in a single grain but differ between other grains, such as in *Grain 1, 2 and 3* in figure 2.14 b). It should be mentioned that metals of similar crystallographic structures slip on the same slip plane, in the same direction, even though the adjacent grains may have a different direction from each other. Why slip occurs is because the shear stress between the planes has overcome a critical value, to cause a slip, the force needs to be higher than the force provided by the friction between the planes which comes from the metallic bonds [57].

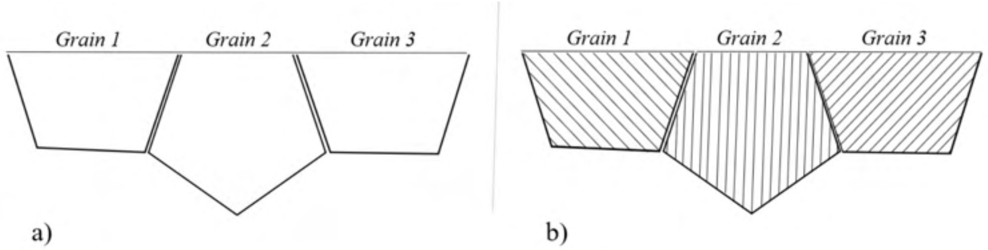

Figure 2.14: Characteristics of three grains in two different states a) without mechanical deformation, no slip bands b) with induced mechanical deformation, visible slip bands.

The possibilities for slip differ between different crystals, this is because the slip plane varies between the crystals. In the case of a uniform crystallographic structure, the displacement will be uniform, since the displacement will occur at the same plane. Since slip in reality occurs gradually, there are instances where displacement is not completely penetrating the plane, this is more commonly known as dislocations, see figure 2.15 [57].

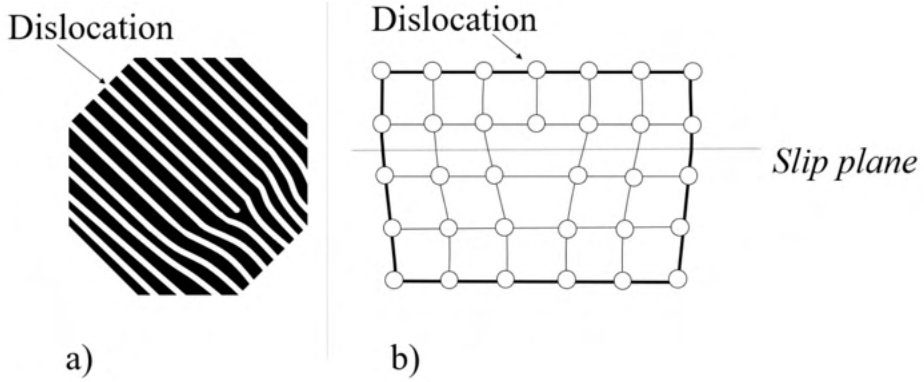

Figure 2.15: a) Dislocation b) edge dislocation with a slip plane.

2.6.2 Dislocation theory

Plasticity occur due to movement of dislocations, which are line defects. Dislocation movement decides how the metal will respond to increased stress, and it is measured in *dislocation density* [*units* m/m^3] which is an expression of how many dislocations there is in a given material [61]. There are several different types of dislocations, the most common once are edge- and screw dislocations or a combination of both. The procedure of how the dislocations differ is declared in figure 2.16. An edge dislocation moves inwards an atomic spacing, the movement causing one extra half-plane in the upper face. In figure 2.16 a) the dashed plane illustrates the separation between slipped and unslipped area, by movement the dashed plane will move to the unslipped side, movement according to the red arrow. The blue line is what a theoretical edge dislocation can be illustrated as. In figure 2.16 b) an illustration of the screw dislocation is declared, and the dashed line illustrates the burger vector. A screw dislocation will move in the same direction as the normal to the slip [57].

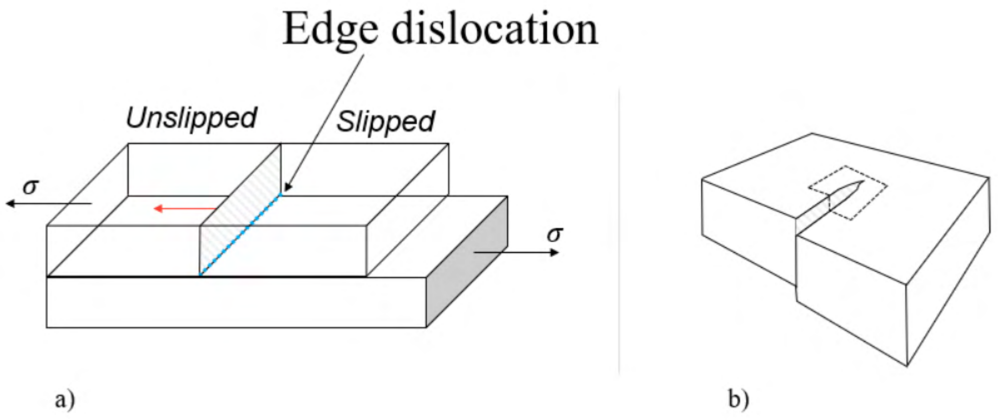

Figure 2.16: a) Edge dislocation b) screw dislocation.

Movement of dislocation is based on *Burgers vector* and the activation barrier, so called *Peierls stress*. If the applied stress overcomes the Peierls stress slip occurs. When dislocations move, only a certain position of the dislocation can move freely within the lattice, because parts of the dislocation will be stuck at defects and interruptions which prevents dislocation motions. For example, grain boundaries, stacking fault inclusions and pint defects [61].

Cold working or strain hardening is a technique that strengthens materials by increasing the density of dislocations within the material. As the dislocation density increases, the movement of dislocations decreases, resulting in the hardening of the material. This method is typically employed at temperatures ranging from room temperature (T_R) up to 30% of the material's melting point (T_m). In addition to the strengthening effect, cold working can also lead to grain refinement as the grains become disrupted during the process [62].

2.6.3 Mechanical twinning

Another mechanical deformation that can appear within plastic deformation is deformation twinning. Twinning gives rise to plasticity due to applied strain [61]. Iron has a tendency to deform by twinning or by *Neumann bands* and the difference between twinning and slip is how the atoms move. By twinning every single atom in each plan can move by different distances because of the shear and it will rearrange the lattice of the crystal. By moving different distances the twinning plane exhibits a mirror-like structure around the plane [56]. In the case where slip band is hard to initiate, twinning can be performed instead to achieve plastic strain. Depending on which crystallographic structure the material exhibits the outcome will differ. For HCP crystals where only one slip plane is possible, twinning has a huge influence because it enables deformation to occure. For HCP crystals the value of c/a has a great influence. A c/a is calculated as the ideal axial ratio where a is the interatomic distance and c is the stacked plane. The value comes from stacking faults which describe two-dimensional planar defects within a crystal. For HCP crystal due to the c/a value the crystal will deform anisotropic [61], how c/a value is measured is illustrated in appendix A, figure A.3.

2.6.4 Mechanical deformation by biaxial Torsion-compression

Biaxial torsion-compression can serve to experimentally simulate a severely deformed surface layer, and replicate what is observed in a worn railway. This technique involves applying mechanical deformation to cylindrical test bars through controlled twisting using a predetermined force or torque. The application of biaxial torsion induces slip bands and deformation twins, effectively activating the material's deformation characteristics [26].

3

Methods

3.1 Experimental procedure

The project focused on inducing mechanical and thermal damages in two different railway steels through experimental methods. The main objective was to evaluate and analyse the microstructural changes and hardness variations in the damaged zones. A comparison was also made between the damaged zones and the respective bulk material for each test.

Both Mn13 test bars and field samples from damaged turnouts were assigned for this study. Field samples were provided by Voestalpine Railway Systems. The test bars were machined by rolling, while the field samples were manufactured through casting. In the case of R260, it comprised test bars and a section of rail that had remained unused. The test bars were machined from bulk material, which was initially undamaged in its virgin state. However, to investigate the initiation of mechanical stresses in connection to thermal damage, these samples needed to undergo predeformation. The field samples, on the other hand, were induced with thermal damage only. All material samples experienced deformation through Rockwell C testing to study the hardness after mechanical deformation had been initiated. The mechanical impacts in field are difficult to achieve in a laboratory study, but indentation testing at least give large plastic strains locally, and can be used for interpretation.

The study entails simulated frictional heating in railway operations using laser heating. This approach has the limitation that it can lead to surface melting. Consequently, the heating in the experiment is more aggressive that in railway operation. However, at larger depth, the material experiences heating cycles similar to what the surface experiences in field operation. Also, crossing noses are often repair welded, and there evidently temperatures exceed the melting temperature, and the experiments done in this study tells how the material could behave during repair welding in field.

The composition of both steels is provided in 1.1. In the subsequent chapter, the analysis methodology for this project is outlined. It encompasses all the necessary steps that were performed in this report

3.2 Mn13-steel, field samples

The components provided for analysis were sourced from damaged crossing noses. Figure 3.1 and 3.2 displayed the specific regions from which the field samples were extracted. *Sample 1* represented a crossing from 2017, and *Sample 2* was from 2015. None of the specimens consisted of repair welds.

Figure 3.1: *D* (2017); field sample of a damaged turnout.

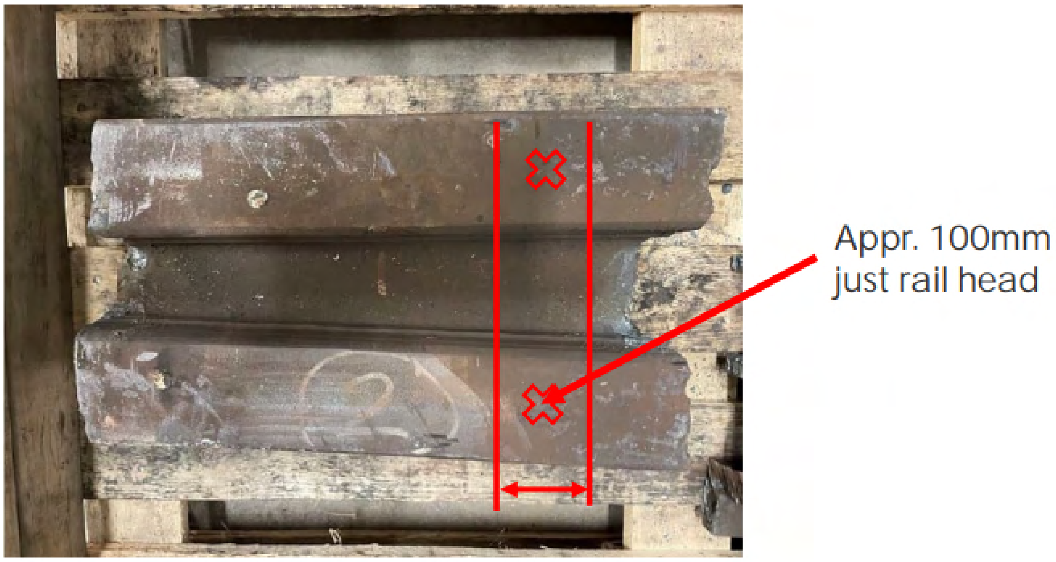

Figure 3.2: *S* (2015); field sample of a damaged turnout

3.3 Predeformation via biaxial twisting

For the experiments, cylindrical test bars were utilised. All specimens had a similar cross-sectional area, with slight variations within a tenth of a millimeter. To ensure force control, the cross-sectional area was measured for the gauge length of each specimen. The force was calculated using the normal tensile test ratio, and an initial nominal stress of -500 MPa [8]. In total, there were nine samples of Mn13 and R260, respectively. The force applied varied slightly among the samples, as indicated in appendix A in table A.1, to ensure a nominal stress of -500 MPa.

.

Predeformation was employed as a method to simulate the appearance of the material when used in an actual railway application. This process triggered the initiation of slip bands and resulted in significant surface deformation. By applying stress slightly above the yield stress, slip bands and deformation twins were induced within the plastic region. Biaxial twisting was only used as a method to perform several deformations at the surface.

The samples were delineated by lines that enclosed the specimen, with a separation of two millimetres. Afterwards, 45° were marked around the sample. The lines together formed a perpendicular grid, as depicted in figure 3.3 *c*). The grid was used for measuring the severely deformed surface layer and served to indicate the total surface shear strain achieved once the test was concluded.

The MTS 809 Axial Torsion machine was employed to enable controlled rotation of the specimens. By utilising the normal tensile test ratio, the forces applied to all specimens could be determined to maintain a stress level of -500 MPa. The rotation cycles were divided into 90-degree increments, with each cycle corresponding to a rotation from -45° to 45°. During the testing, each sample was rotated until the maximum values were reached. Once the specimen had been rotated 90°, the stress and pressure were released, returning the sample to its initial position. The rotation process was then repeated until the specimen reached its maximum torsional capacity and could no longer be rotated further. Figure 3.3 shows the methodology for predeformation in the starting position. The samples were held together at both ends in a fixed position, and the grip was sufficient to prevent the samples from sliding when the lower part rotated. It also shows the insertion and how the grid looked before rotation. Figure 3.4 shows the sample appearance after it had been rotated, where the grid had acquired a different geometry due to the rotation. In appendix A, figure A.4 provides a visualisation of the forces acting on each specimen throughout the duration of the testing process. The testing of all samples was dependent on the failure torque, which was a predetermined value of -2 Nm.

Figure 3.3: Predeformation, a) assembling the specimen in the desired configuration, b) Specimen fixed at both ends c) initial state of the Mn13 sample before any predeformation occurs.

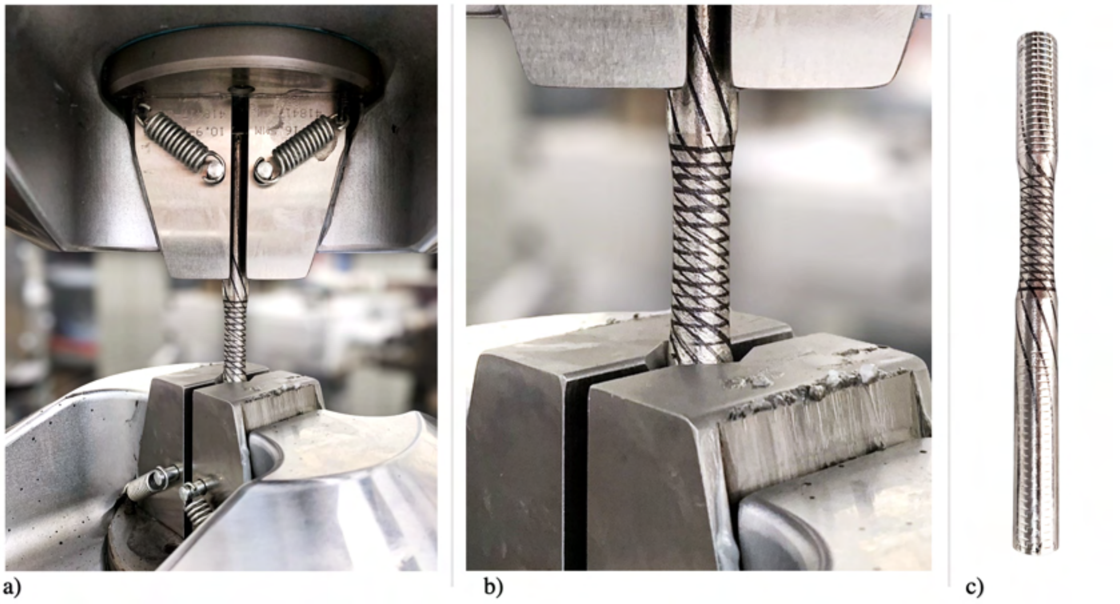

Figure 3.4: Predeformation, a) the samples are rotated until they reach fail torque b) deformed grid, c) test bar after completing the test.

3.3.1 Analysing the result from MTS 809 Axial Torsion

Each specimen was subjected to twisting until it reached its maximum torsional capacity; the torque-threshold was reached. The data were analysed with respect to the spring back effect. During each cycle, relaxation occurred, representing the regression of the specimen due to the elastic region. Table 3.1 represents the number of cycles and the actual rotation given in degrees. The spring back effect is illustrated in figure 3.5, where *a)* describes the plane of rotation, *b)* illustrates the rotational motion applied to the samples, *c)* depicts the spring-back effect, and *d)* represents the actual rotation. The value for position *d)* are the cumulative sum of all cycles and represents the total angle of rotation.

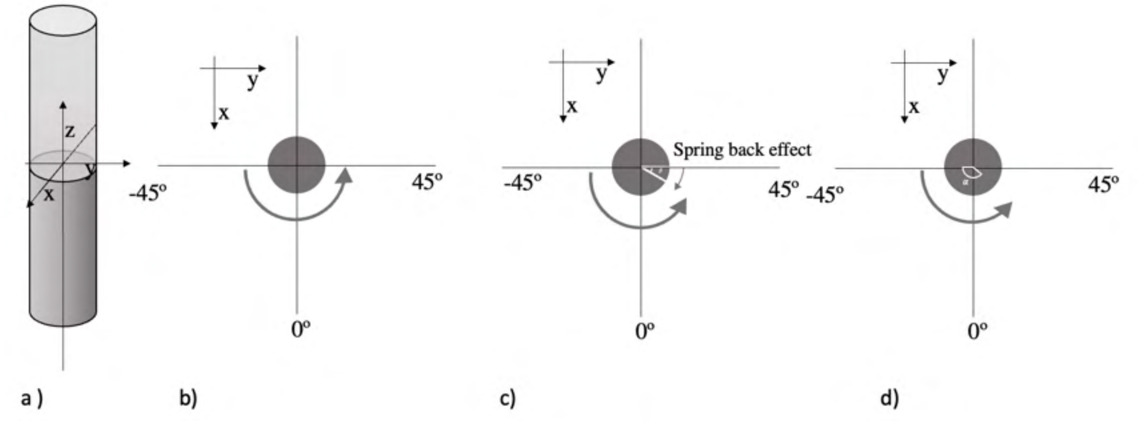

Figure 3.5: Predeformation; a) describes the plane in which the sample is rotated, b) is how the samples are twisted, c) describes the spring back effect and d) is the actual rotation

3.3.2 Surface shear strain

Each specimen was marked with a perpendicular grid. Manual measurements of the angles were performed, as seen in figure 3.6. Angle α was used in equation 3.1, where γ represents the surface shear strain. In table 3.1, the values of γ are given. Multiple measurements were taken for each specimen at various points along the grid.

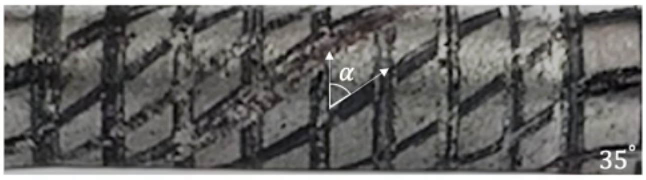

Figure 3.6: Measurement of surface shear strain, angle α is measured and used to calculate γ, which represent surface shear strain

$$\gamma = tan(\alpha - 90°) \tag{3.1}$$

Table 3.1: Surface shear strain for R260 and Mn13

Material_Specimen	Total cycles	Angle of rotation	Surface shear strain γ
R260_R1	5	375°	40°
R260_R2	4	293 °	35°
R260_R3	4	295 °	34°
R260_R4	4	328 °	37°
R260_R5	4	316 °	40°
R260_R6	4	316 °	35°
R260_R7	4	295 °	35°
R260_R8	4	325 °	35°
R260_R1	4	328 °	30°
Mn13_M1	11	823 °	58°
Mn13_M2	11	824 °	55°
Mn13_M3	10	772 °	54°
Mn13_M4	7	520 °	42°
Mn13_M5	6	365 °	29°
Mn13_M6	6	442 °	34°
Mn13_M7	10	756 °	55°
Mn13_M8	10	750 °	58°
Mn13_M9	10	768 °	62°

3.4 Inducing thermal damage with a laser source

Thermal heat pulses were applied using Fiber Laser ALF 900 W to locally generate thermal heat. The samples were exposed to local heating on a predeformed and non-deformed surface. Self-cooling occurred in a similar manner to ordinary railway rails. Due to the significant temperature gradient, heat was conducted into the bulk material, eliminating the need for quenching.

The Fiber Laser ALF 900W was utilised as the equipment for achieving heat initiation. Table 3.2 shows the capacity of the equipment, and the selected setting for this project was a spot diameter of 2 mm whit a flat power profile. Although the equipment is typically used for welding with a narrow welding profile, it demonstrated notable efficacy in generating thermal pulses. Figure 3.7 illustrates the equipment, where *a)* displayed a photograph of the equipment, *b)* demonstrate the expedient arrangement of the samples, and *c)* shows the outcome of a heat pulse at a magnification of 20.5x in R260 steel.

Table 3.2: Fiber Laser AL-F 900 W capacity

Fiber laser 1070 nm	Average power	Peak pulse power	Pulse energy max	Pulse duration	Pulse frequency	Welding Spot
Fiber-900 F	900 W	9kW	90 J	0.2 ms-CW	0-100 Hz	0.3-3 mm optional 1.1-4 mm

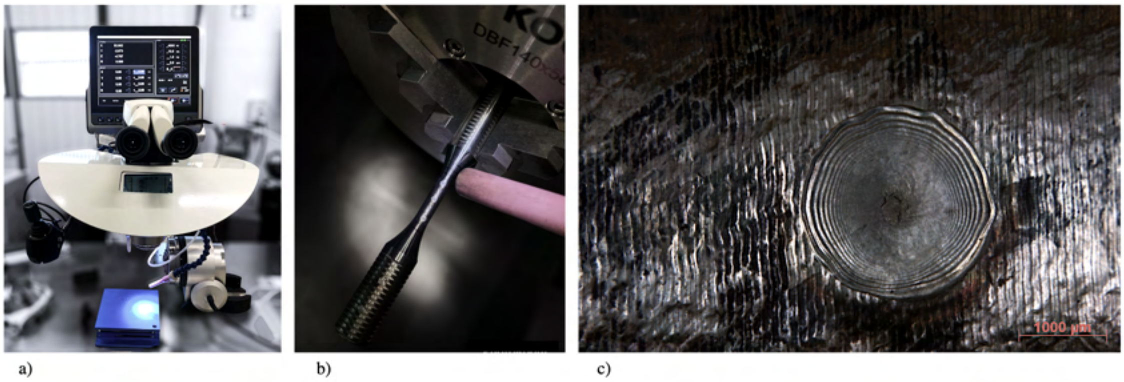

Figure 3.7: Method description of LHT, where a) displays the equipment Fiber Laser AL-F 900 W. b) demonstrates the attachment of the sample and the location of the heat points for R260-R9 and c), the appearance of the local heat points is depicted with a magnification of 20.5 for Mn13-M5

3.5 Sample preparation for metallography

Sample preparation was a necessary step before analysis in an optical microscope. All specimens had a cylindrical shape with a diameter deviation of a tenth of a millimeter, while there was a significant deviation in gauge lengths. Since only a small portion of each sample would be analysed, the effect of this deviation was assumed to be minor and not of concern. The sample preparation process began with cutting out a suitable size from the initial shape of the specimen. The cutting procedure are illustrated in figure 3.8 and 3.9. The incisions were made approximately fifteen millimeters apart and symmetrically around the heat pulse. This approach allowed for the examination of interesting areas such as the heat pulse and the region for possible recrystallisation.

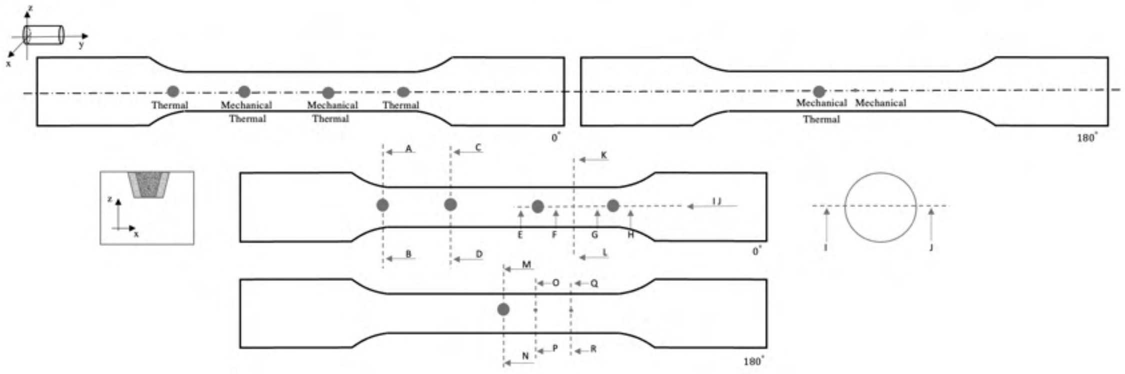

Figure 3.8: Cutting technique for sample Mn13-M5

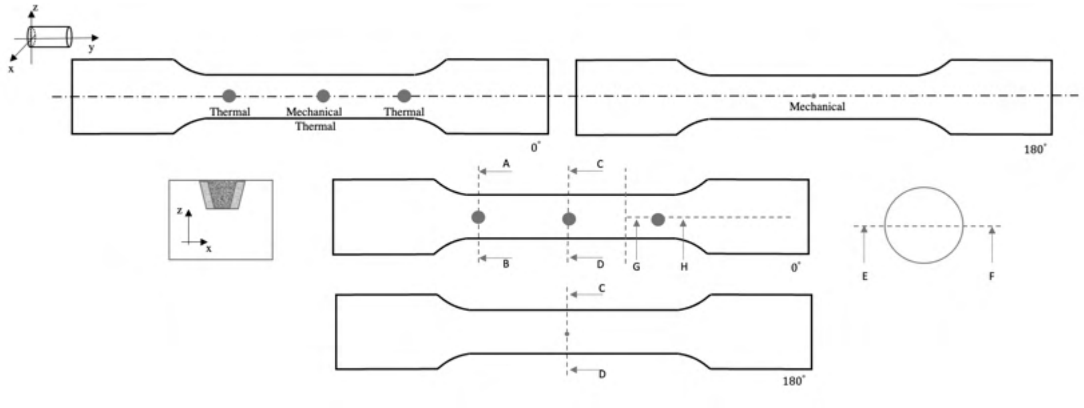

Figure 3.9: Cutting technique for sample R260-R9

The cutting can be performed manually or automatically, depending on the machine setting. Since it was significantly important not to contaminate the samples with other heat sources, each incision had to be relatively quick to prevent microstructural influences from saw blades. After the samples were cut, the surface edges had to be ground. Manual grinding was carried out using a *Struers Labopol-21.* This step aimed to remove any rough edges from the cut surfaces.

After the edges of the samples had been ground, the specimens needed to be mounted. This was done using the *citopress, 20 hot mounter.* Each sample was

Table 3.3: Polishing methodology for pearlitic and manganese steel

Step	Speed [rpm]	Time [min]	Force [N]	Rotation	Suspension	Grit/polishing cloth
1	300	7	15	↺↻	Water	2000 μm
2	150	7	20	↺↻	Water	4000 μm
3	150	9	15	↺↻	Diamond suspension	9 μm
4	150	9	20	↺↺	Diamond suspension	3 μm
5	150	9	20	↺↺	Diamond suspension	1 μm
6	150	5	15	↺↺	OP-S Colloidal silica	0.04 μm

mounted with a conductive polyfast resin, which is typically used for scanning electron microscopy (*SEM*). The Citopress could accommodate two different sizes, and in this case, 20 ml of polyfast resin was used for each sample. The estimated time for mounting each sample was approximately five minutes. Once the samples had been mounted, the surfaces needed to be ground to remove any excess material. This step was necessary because the samples had become embedded in the polyfast resin. The samples were ground flat to ensure a smooth and even surface.

The penultimate step involved polishing the samples using the *TegraPol-31 machine*. All steps are specified in table 3.3. The TegraPol-31 machine have the capability to polish six samples simultaneously. After each polishing step, it was necessary to clean the samples thoroughly with water to remove any residual particles and impurities. The final step in the sample preparation was etching, where *nital 2 %* was used as the etchant. Nital had been commonly employed for etching samples in previous investigations of pearlitic steel, and it was also utilised in this study for the etching of austenitic manganese steel samples.

Each sample was immersed in a 2% Nital solution for a duration of five seconds, followed by immediate rinsing in 96% ethanol and subsequent drying using compressed air. As the etching process could occur rapidly, each specimen was carefully monitored every five seconds. The sample was repeatedly immersed in the Nital solution until noticeable changes were observed on the surface, ensuring the desired etching effect was achieved. Finally, the samples were thoroughly cleaned using ethanol and dried using compressed air. To ensure proper etching had been carried out, each sample was subjected to analysis under an optical microscope.

3.6 Optical microscopy

Optical microscopy (*OM*) provides analytical information about the materials' surface and internal structures, it allows analysis of the material's morphology, structure, grain, phase, embedded phases, and particles. The results are declared subsequently as magnified images. The technology behind OM involves reflected light from the surface of the sample, and the reflection subsequently creates a digital image. The study of grains and phases is determined by the ability of an image to create contrasts, which are manifested as variations in local colors and resolutions under different lighting conditions [63].

The methodology employed in this study involved the metallographic sample preparation of the specimens. The prepared samples were then examined under the lens of an optical microscope, with the lens positioned perpendicular to the sample surface. The microscope was equipped with various functions that worked together to produce magnified and clear images. These functions included magnification, sharpness, and brightness. The images were stored and analysed in Zeiss Zen, a software adapted for microscopy.

3.7 Hardness testing

Hardness testing for material characterisation was made by *Struers DuraScan 70 machine* with respect to Vickers scale (HV). The method was based on pressing a diamond into the material with a predetermined force. The hardness of the diamond was well-known, and by considering factors such as the angle of the diamond tip and the force applied, the pressure exerted on the material could be determined, thereby enabling the calculation of its hardness, as depicted in figure 3.10.

The machine is equipped with a microscope lens that enabled the analysis of the material's surface and facilitated the selection of specific grains or phases for examination. Once the appropriate surface was selected, the diamond indenter was brought into contact with the material's surface. The force applied gradually increased until it reached the predetermined value set for the hardness test. Once the predetermined force was reached, it was held constant for a specific duration of time. After this holding period, the force was released, and the indenter was removed from the material.

The indentation that was formed was analysed immediately after the force was released. Both d_1 and d_2 were measured as shown in figure 3.10. The Vickers hardness value was calculated based on the previously discussed theoretical principles, which involved dividing the applied force by the surface area A of the indentation. Manual calculations were not required as the Struers DuraScan 70 machine was equipped with software that automatically performed these calculations.

Microhardness was evaluated as a line profile between the thermal pulse and bulk material, as well as close to the deformed surface and slightly beyond for thermal and/or mechanical spots. Illustrations of the different profiles are presented in figure 3.11. The method was used to study changes in the hardness of the microstructure of bulk material as well as deformed or altered material. The settings provided by microhardness were HV 0.1, with a spacing of 0.1−0.2 mm between each indentation. The method description followed the previously stated method, but the force applied during indentation was significantly lower compared to valid hardness profiles.

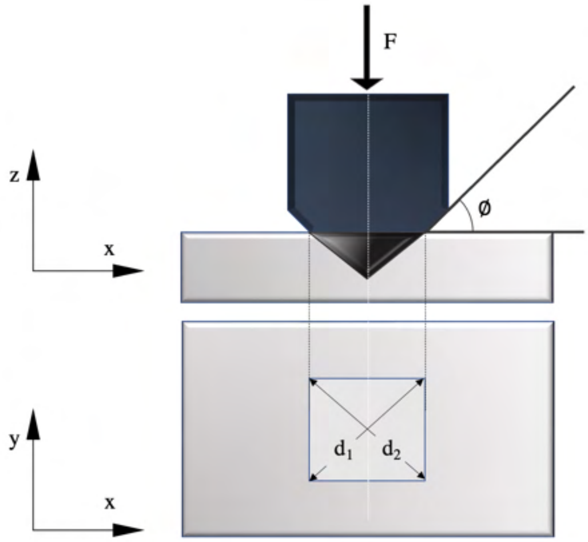

Figure 3.10: Methodology hardness testing via Vickers hardness.

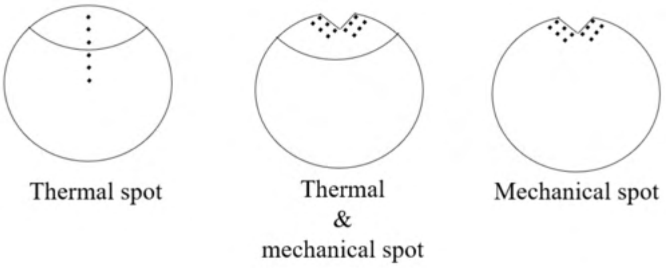

Figure 3.11: Hardness evaluation for different types of deformed/changed sample a) demonstrate a line profile b) demonstrate the hardness profile at a thermal pulse with an indent and c) demonstrate hardness profile around an indent

3.8 Deformation by Rockwell C testing

The methodology for analysing resistance to mechanical deformation involved deforming the material using a specific force and subsequently measuring the resulting hardness change near the indentation. The Rockwell C testing method was employed to perform the indents. This technique utilised a Rockwell indenter, in this case, a spheroconical diamond, which was applied with a predetermined load of 150 [*kgf*]. To ensure proper contact between the specimen and the indenter, a preload of 3 kgf was initially applied to the sample. The test was initiated by operating the arm of the Wolpert machine. As the arm reached its highest position, a dwell time countdown of 10 seconds commenced for these specific samples. Once the dwell time elapsed, the test for the particular sample was considered complete. The machine setup is illustrated in figure 3.12, while two indentations are depicted in figure 3.13. Indentations were made on the surface of predeformed specimens and in thermal spots.

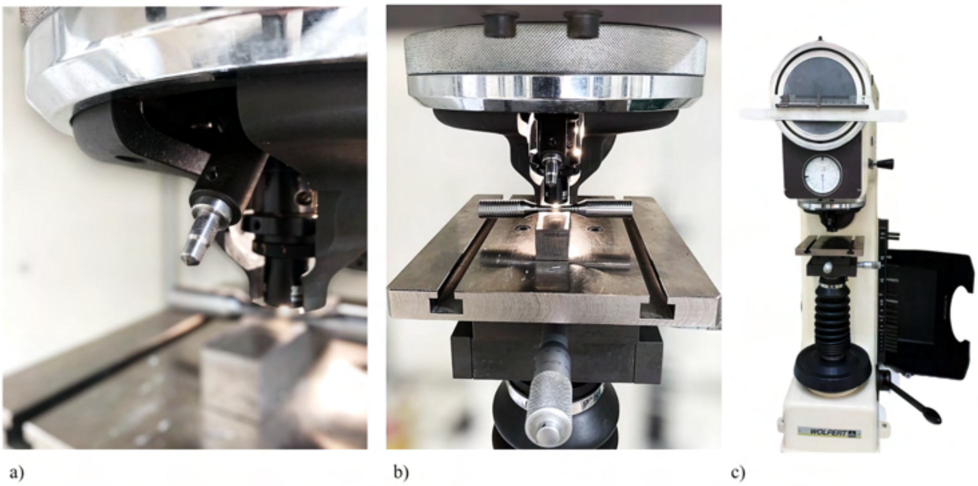

a) b) c)

Figure 3.12: Wolpert machine test set up with a) Rockwell indenter *spheroconical diamond*, b) sample and indenter in contact c) Wolpert machine

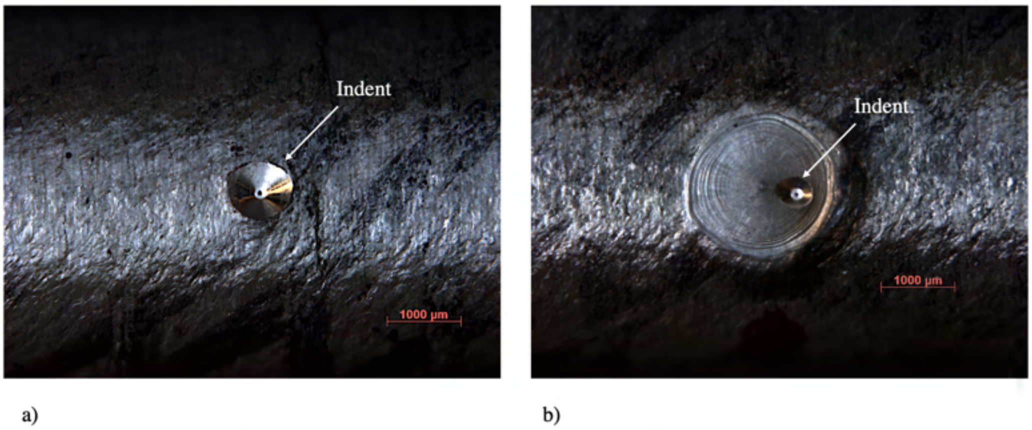

a) b)

Figure 3.13: Indents made in the following locations: a) on a predeformed surface of R260 steel, and b) in a thermal spot of R260 steel

The Rockwell C testing technique was utilised to induce surface deformation at the thermal spot. The penetration of the indenter generated residual deformation at the surface. This method was employed to investigate the alteration in hardness of the material when mechanical loads were applied subsequent to thermal loads.

3.9 Assumptions and deviations for tests and preparation for tests

The test bars were inspected using a simple micrometer, although slight deviations may have arisen due to the manual reading of the measuring tool. As many of the preparation methods for optical microscopy (OM) relied on the manual operation of machines, variations in spot size and roughness occurred, particularly during grinding and polishing procedures. The duration of etching played a critical role in the clarity with which phases and grains were revealed in OM. In certain instances, over or uneven etching resulted in difficulties in interpreting the results.

4

Results

The following chapter presents the results of the hardness profiles and microstructural characterisation for both materials. Furthermore, any defects that occurred during the testing process are reported.

4.1 Results of hardness analysis

The microhardness profiles for both materials are reported. Hardness profile show variations in hardness along the indentations from Rockwell c testing and line hardness between phases of thermally affected material and unaffected material. The hardness values provide information on the differences in phases and areas of the exposed materials.

Hardness profiles were performed for the combinations to which the materials were exposed to:

- Thermal pulse effects on virgin material
- Thermal pulse effects on severely deformed surfaces
- Thermal pulse and deformation by spheroconical diamond on severely deformed surfaces
- Deformation by spheroconical diamond on severely deformed surfaces
- Thermal pulse effects on field samples
- Thermal pulse and deformation by spheroconical diamond effects on field samples
- Deformation by spheroconical diamond effects on field samples

The samples tested are assigned specific abbreviations for ease of reference. The table 4.1 provides an overview of the abbreviations used to identify each sample. The number of addresses to each specimen is only used to indicate the batch.

Table 4.1: Specific abbreviations used for test batches

Abbreviation	Explanation
V	Virgin material subjected to thermal pulses
T	Predeformed and subjected to thermal pulse
M	Predeformed and subjected to mechanical impact
T+M	Predeformed and subjected to thermal and mechanical impact
F	Field sample

4.1.1 Hardness distribution of sample Mn13_V$_1$

Two line profiles, as depicted in figure 4.8, illustrate the characteristics of an undeformed Mn13 sample subjected to a thermal pulse. Each line was positioned approximately 0.1 mm from the surface, with a spacing of 0.1 mm between each indentation. The findings revealed variations in hardness within the thermal pulse and the bulk material. The highest hardness was observed near the HAZ.

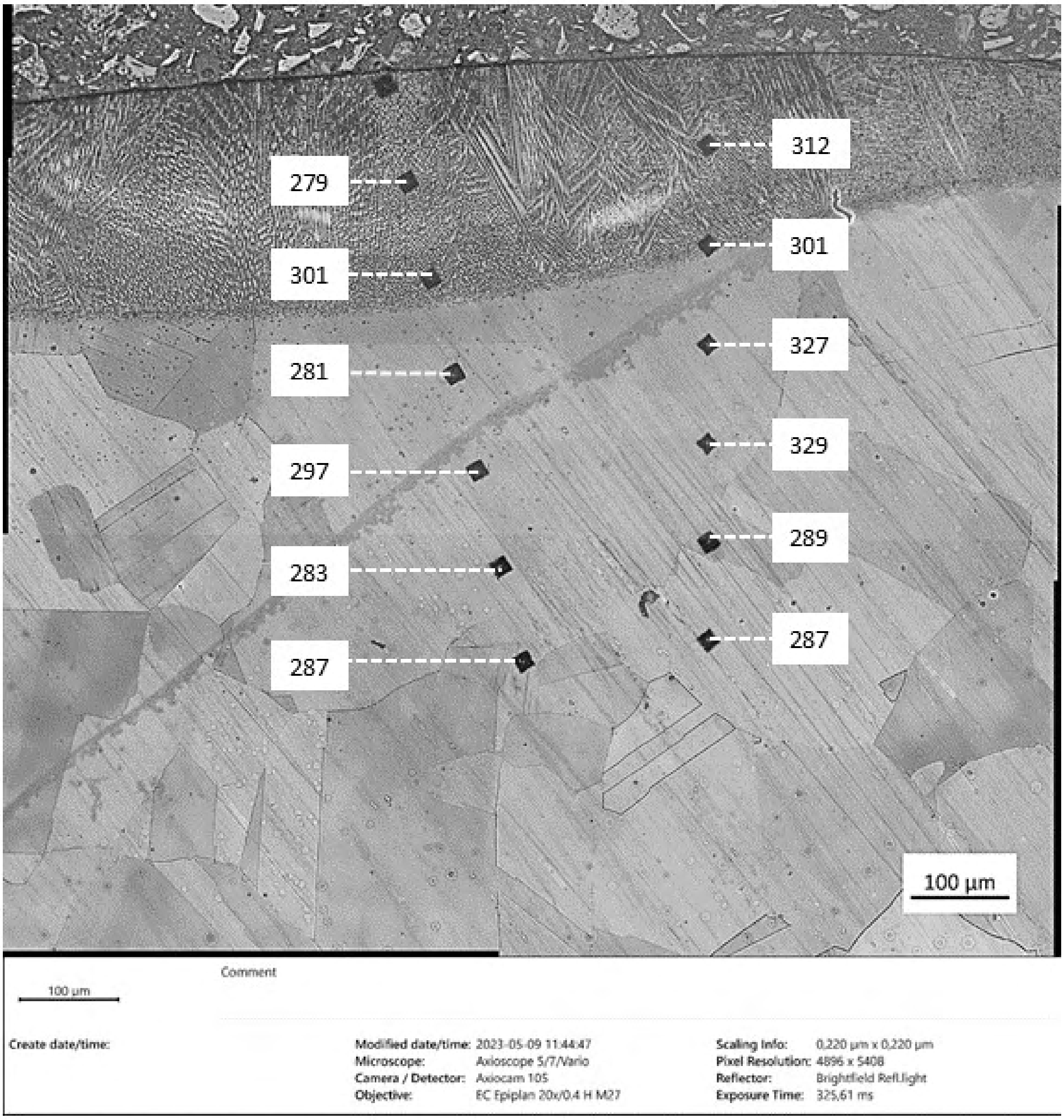

Comment

Create date/time:

Modified date/time: 2023-05-09 11:44:47
Microscope: Axioscope 5/7/Vario
Camera / Detector: Axiocam 105
Objective: EC Epiplan 20x/0.4 H M27

Scaling Info: 0,220 µm x 0,220 µm
Pixel Resolution: 4896 x 5408
Reflector: Brightfield Refl.light
Exposure Time: 325,61 ms

Figure 4.1: Optical microscope image of Mn13_M5_V1 with microhardness indents visible, specified in HV [0.1]

4.1.2 Hardness distribution of sample Mn13_V$_2$

The second sample, similar to sample Mn13_V$_1$, consisted of undeformed material that was subjected to a thermal pulse. In this case, it was observed that the hardness profile follows a pattern; hardness increased as the distance from the surface increased. Within the HAZ, similar to sample *Mn13_V*$_1$, the hardness demonstrated an upward trend. Figure 4.2 presented the hardness profiles of the second sample. The left profile showed overall variations in hardness, indicating different hardness values at various depths. On the other hand, the right profile specifically demonstrated an upward trend in hardness as the depth from the surface increased. Notably, an increase in hardness was evident in the surrounding area of the HAZ. The difference could be due to sampling, due to the large grain size.

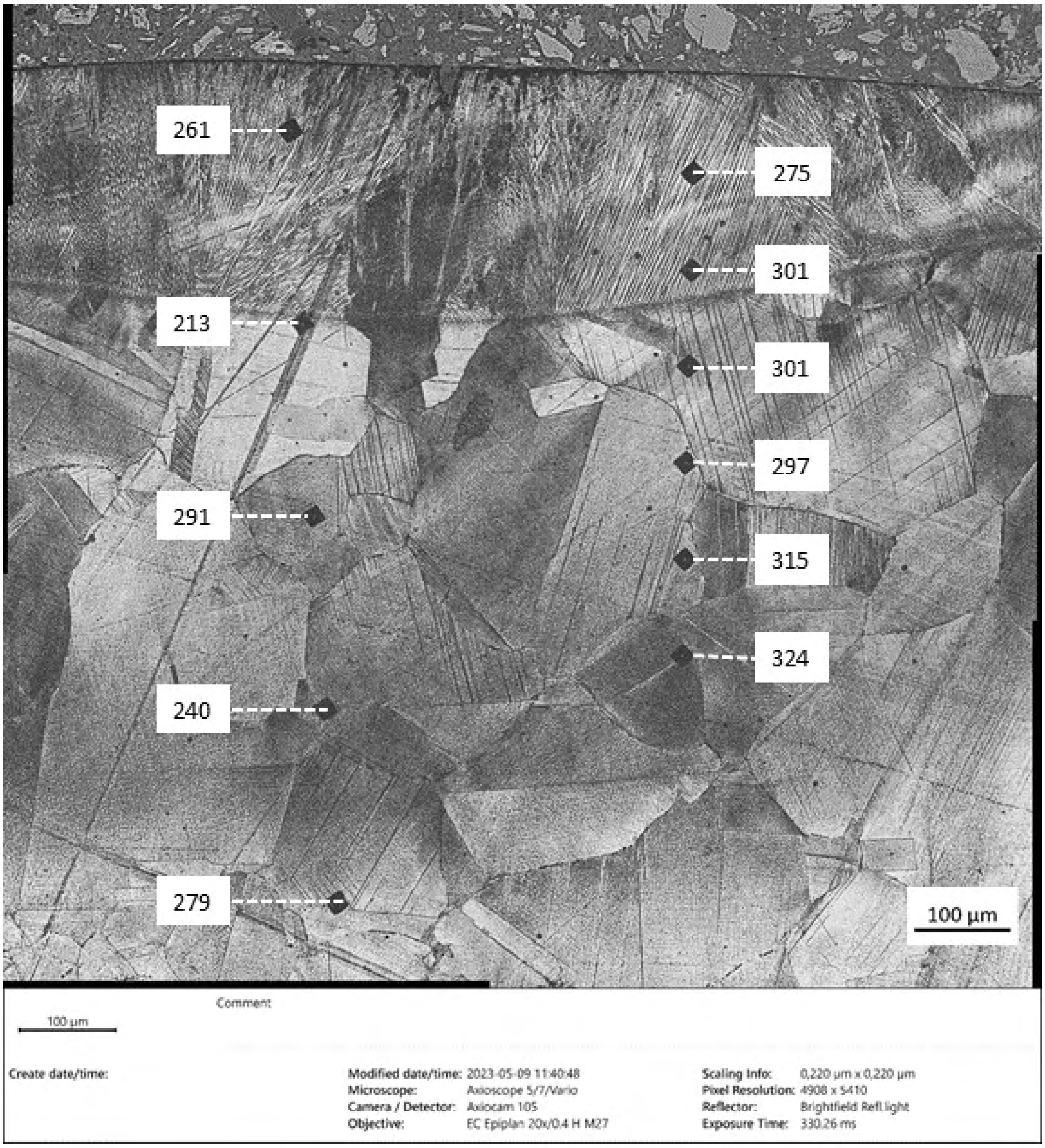

Create date/time:

Modified date/time: 2023-05-09 11:40:48
Microscope: Axioscope 5/7/Vario
Camera / Detector: Axiocam 105
Objective: EC Epiplan 20x/0.4 H M27

Scaling Info: 0,220 µm x 0,220 µm
Pixel Resolution: 4908 x 5410
Reflector: Brightfield Refl.light
Exposure Time: 330.26 ms

Figure 4.2: Optical microscope image of Mn13_V$_2$ with microhardness indents visible, specified in HV [0.1]

4.1.3 Hardness distribution of sample Mn13_T_3

Figure 4.3 displays Mn13 subjected to a thermal pulse on severely deformed surface. The hardness profile reveals an much higher increase in hardness with increased distance from the surface. The hardness measurements range from 221 to 455 HV. The indentations were made at a depth of 0.5 mm from the surface, with a spacing of 0.1 mm between each indentation. The hardness is measured at the interface between the phases and results in a hardness of 281 HV.

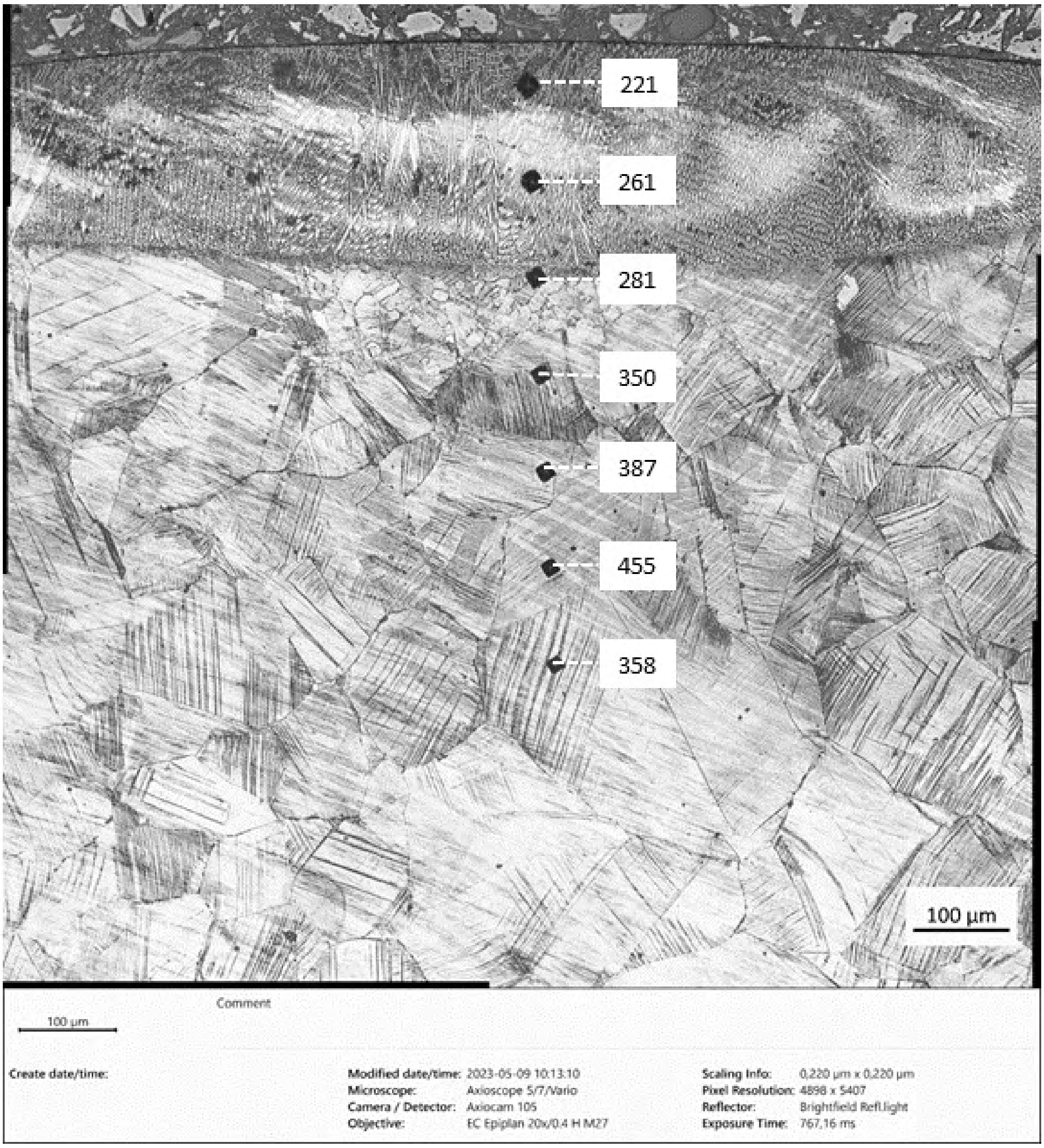

Create date/time:
Modified date/time: 2023-05-09 10:13:10
Microscope: Axioscope 5/7/Vario
Camera / Detector: Axiocam 105
Objective: EC Epiplan 20x/0.4 H M27
Scaling Info: 0,220 µm x 0,220 µm
Pixel Resolution: 4898 x 5407
Reflector: Brightfield Refl.light
Exposure Time: 767,16 ms

Figure 4.3: Optical microscope image of Mn13_T_3 with microhardness indents visible, specified in HV [0.1]

4.1.4 Hardness distribution of sample Mn13_T_4

The hardness profile of Mn13_T_4 is consistent with the results from Mn13_T_3. Figure 4.4 reveals the hardness profile. Both samples were subjected to a thermal pulse on sever deformed surfaces. In Mn13_T_4, the hardness ranged from 236 to 463 HV. The distance from the surface to the first identification point was slightly over 0.1 mm, with a subsequent indent spacing of 0.1 mm. In the proximity of the interface between the phases, a hardness value of 263 HV was observed.

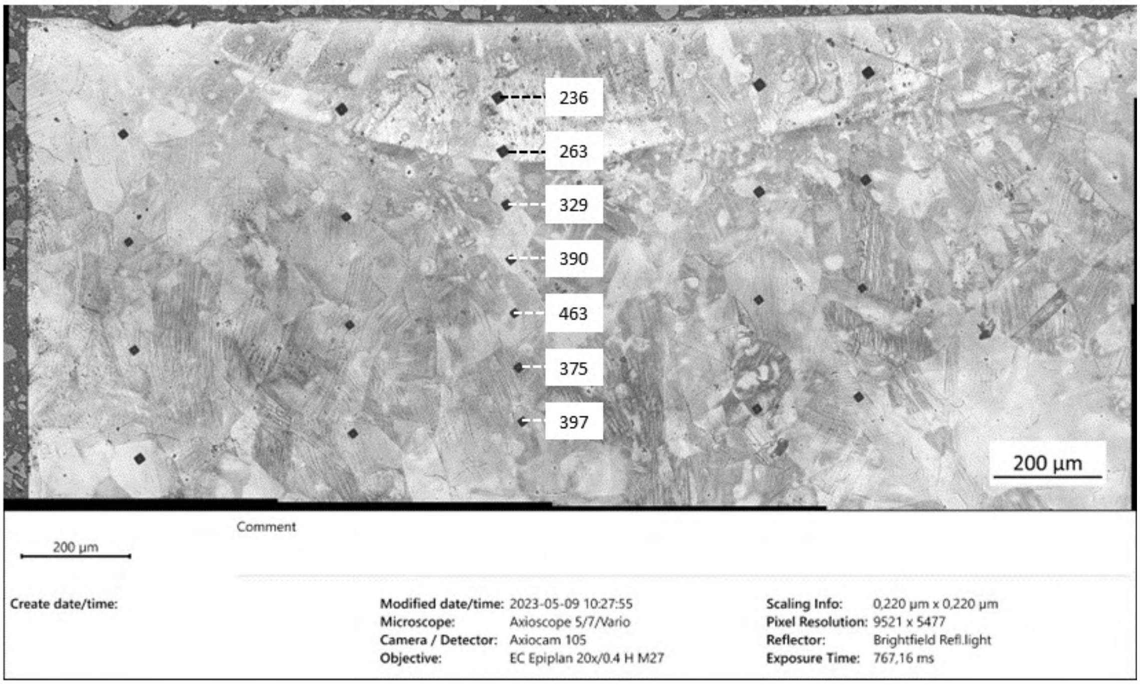

Create date/time:

Modified date/time: 2023-05-09 10:27:55
Microscope: Axioscope 5/7/Vario
Camera / Detector: Axiocam 105
Objective: EC Epiplan 20x/0.4 H M27

Scaling Info: 0,220 µm x 0,220 µm
Pixel Resolution: 9521 x 5477
Reflector: Brightfield Refl.light
Exposure Time: 767,16 ms

Figure 4.4: Optical microscope image of Mn13_T_4 with microhardness indents visible, specified in HV [0.1]

4.1.5 Hardness distribution of sample Mn13_T+M$_1$

Figure 4.5 presents the hardness profile of Mn13 sample Mn13_T+M$_1$ that had been subjected to a thermal pulse on several deform surfaces and mechanical impact by deformation with a Rockwell C testing indenter. It was evident that the region closest to the deformation caused by the mechanical impact exhibited the highest hardness, reaching up to 609 HV. In contrast, the areas located outside the thermal pulse and the deformed region exhibited lower hardness values, with the highest value of 447 HV. These results were consistent with the values obtained from other deformed bulk materials depicted in 4.3 and 4.4.

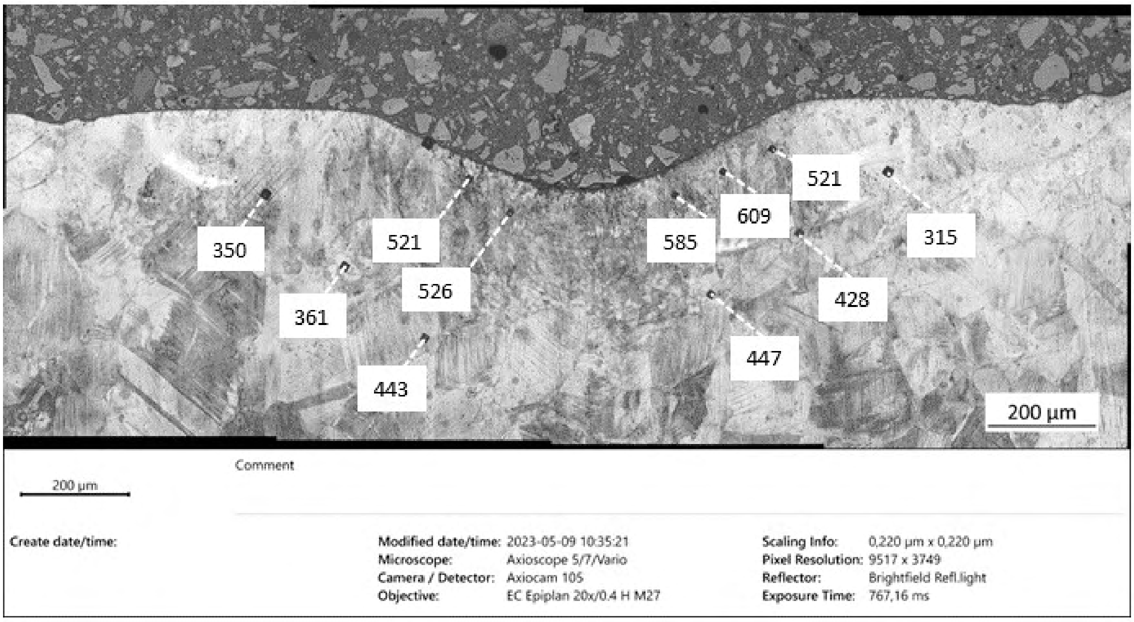

Create date/time:
Modified date/time: 2023-05-09 10:35:21
Microscope: Axioscope 5/7/Vario
Camera / Detector: Axiocam 105
Objective: EC Epiplan 20x/0.4 H M27
Scaling Info: 0,220 µm x 0,220 µm
Pixel Resolution: 9517 x 3749
Reflector: Brightfield Refl.light
Exposure Time: 767,16 ms

Figure 4.5: Optical microscope image of Mn13_T+M$_1$ with microhardness indents visible, specified in HV [0.1]

4.1.6 Hardness distribution of sample Mn13_T_5

The hardness profile of Mn13 sample Mn13_T_5 is declared in figure 4.6, which exhibited a similar range to the previous Mn13 samples that had experienced severe deformation with a thermal pulse at the surface. The indentations for hardness measurement were spaced 0.1 mm apart, and the indent near the surface was also spaced 0.1 mm. The highest recorded hardness value was 479 HV, while the lowest value was 279 HV.

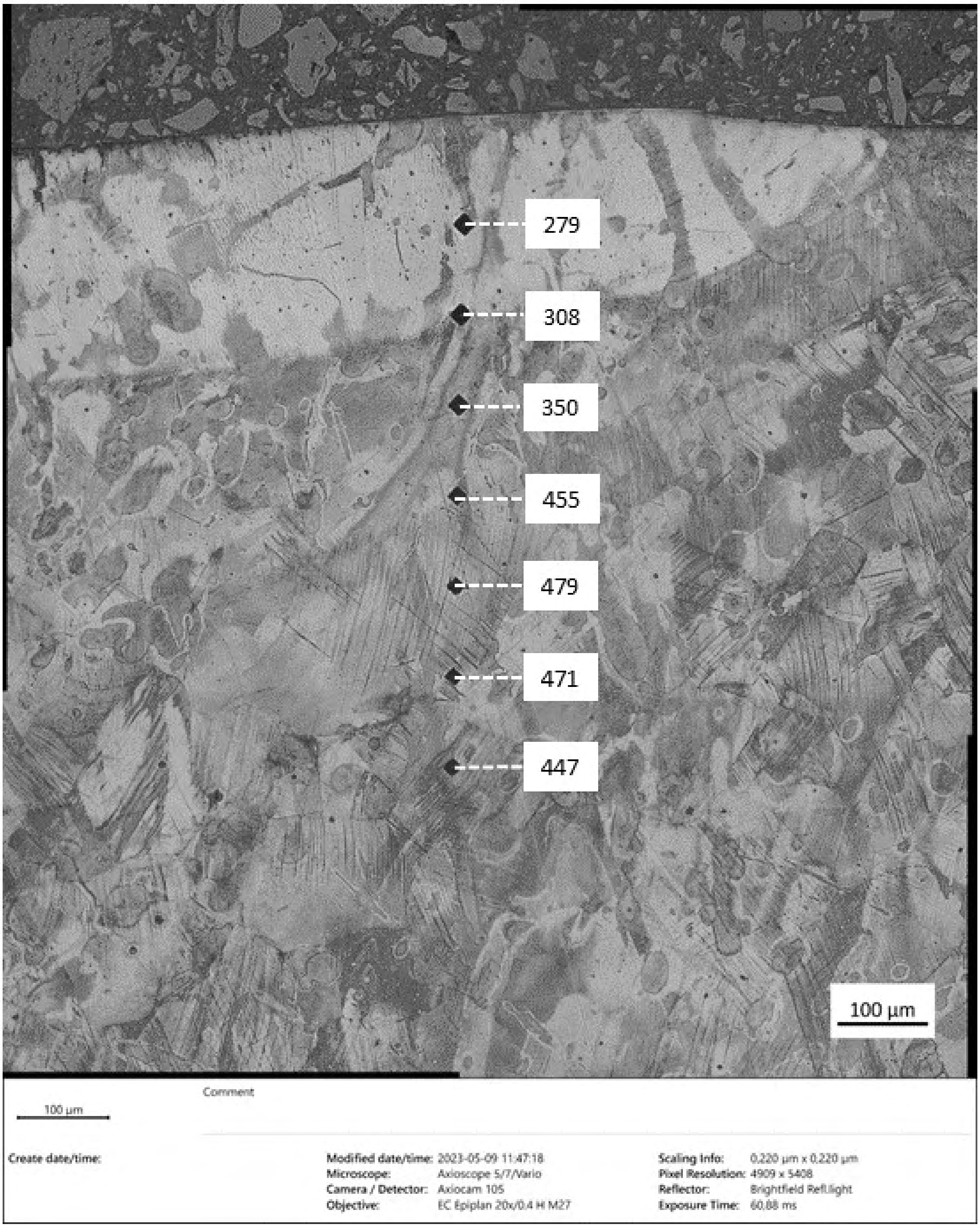

Create date/time:

Modified date/time: 2023-05-09 11:47:18
Microscope: Axioscope 5/7/Vario
Camera / Detector: Axiocam 105
Objective: EC Epiplan 20x/0.4 H M27

Scaling Info: 0.220 µm x 0.220 µm
Pixel Resolution: 4909 x 5408
Reflector: Brightfield Refl.light
Exposure Time: 60.88 ms

Figure 4.6: Optical microscope image of Mn13_T_5 with microhardness indents visible, specified in HV [0.1]

4.1.7 Hardness distribution of sample Mn13_T+M_2

The second Mn13 sample Mn13_T+M_2, with a combination of severe surface deformation, heat treatment with a thermal pulse, and deformation with an indenter, exhibited the same behaviour as Mn13_T+M_1. The hardness profile is shown in figure 4.7. Within the deformed zone from mechanical impact and a thermal pulse, the hardness reached its highest value, with a maximum measurement of 837 HV. In the region outside the deformed surface but still within the thermal zone, the hardness dropped significantly to 295 HV. Outside the area of deformation in the severely deformed surface, the hardness was comparable to the previously deformed bulk material, ranging from 369 to 516 HV.

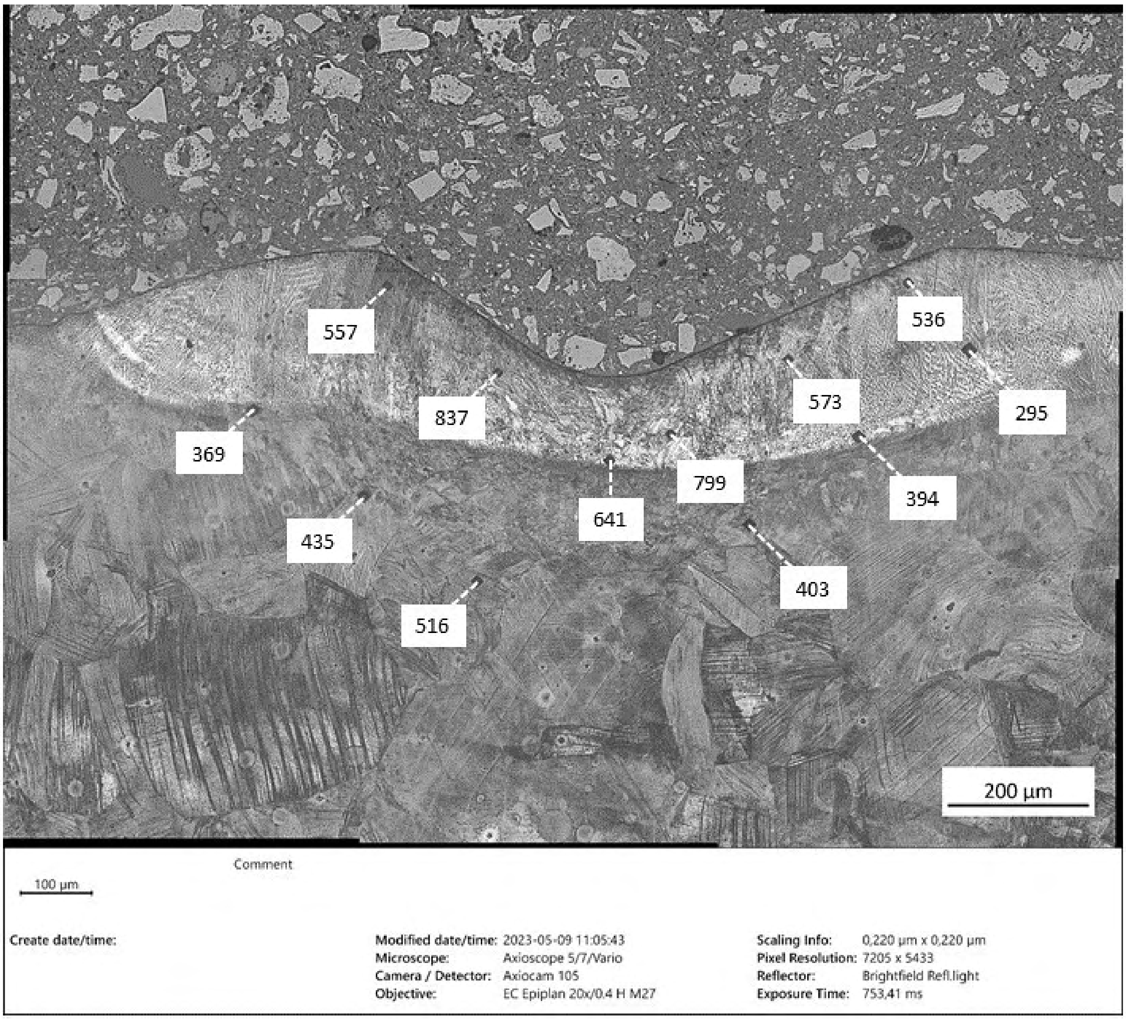

Create date/time:
Modified date/time: 2023-05-09 11:05:43
Microscope: Axioscope 5/7/Vario
Camera / Detector: Axiocam 105
Objective: EC Epiplan 20x/0.4 H M27
Scaling Info: 0,220 µm x 0,220 µm
Pixel Resolution: 7205 x 5433
Reflector: Brightfield Refl.light
Exposure Time: 753,41 ms

Figure 4.7: Optical microscope image of Mn13_T+M_2 with microhardness indents visible, specified in HV [0.1]

4.1.8 Hardness distribution of sample Mn13_M$_1$

The Mn13_M$_1$ specimen experienced a combination of severe surface deformation and mechanical impact through deformation by a Rockwell C testing indenter. The result of the hardness profile for this specimen is shown in figure 4.8. The hardness profile exhibited variations, with regions near the deformation showing high hardness values, reaching up to 729 HV. However, there were also areas along the profile where the hardness was lower compared to the hardness profile outside the deformed surface.

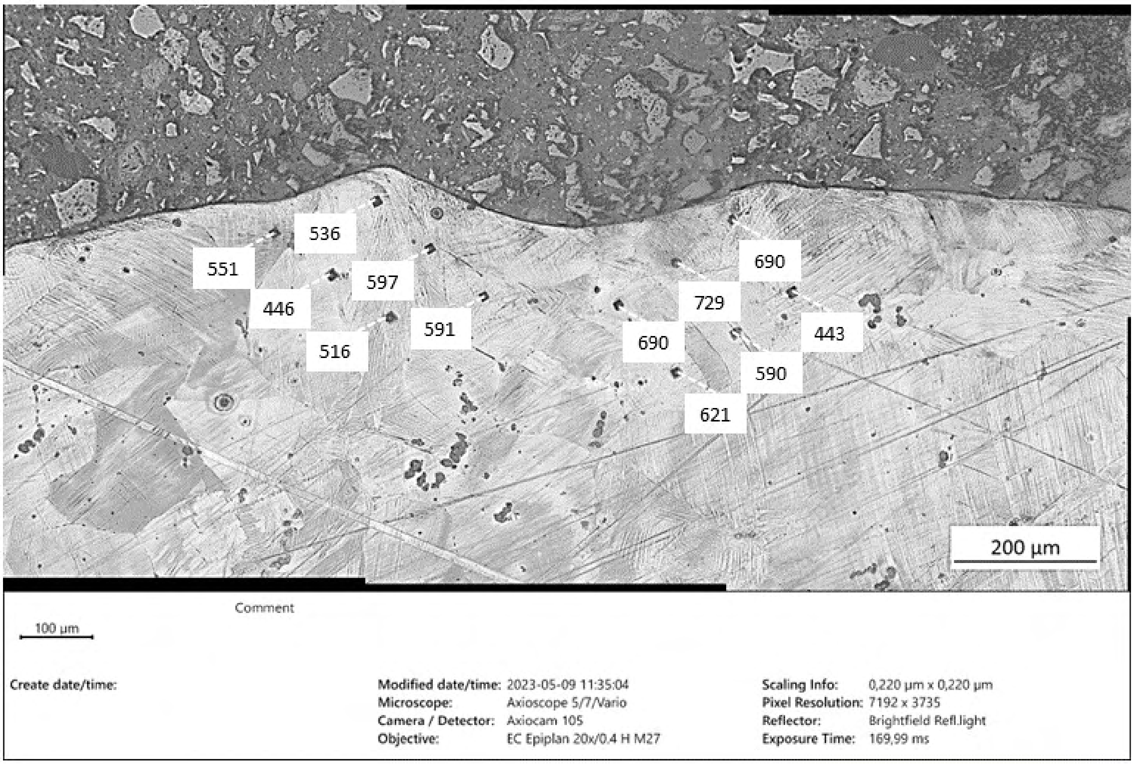

Create date/time:
Modified date/time: 2023-05-09 11:35:04
Microscope: Axioscope 5/7/Vario
Camera / Detector: Axiocam 105
Objective: EC Epiplan 20x/0.4 H M27
Scaling Info: 0,220 µm x 0,220 µm
Pixel Resolution: 7192 x 3735
Reflector: Brightfield Refl.light
Exposure Time: 169,99 ms

Figure 4.8: Optical microscope image of Mn13_M$_1$ with microhardness indents visible, specified in HV [0.1]

4.1.9 Hardness distribution of sample Mn13_M$_2$

Mn13_M$_2$ comprised the same combination as Mn13_M$_1$. The hardness profile is shown in appendix B, figure B.1. The hardness profile displayed a similar pattern to the previous observations in Mn13_T+M$_1$ and Mn13_T+M$_2$, where the highest hardness was observed in the deformed region and gradually decreased with increasing distance from the deformation.

4.1.10 Hardness distribution of sample Mn13_field sample_F_1T_1

The specimen labelled as Mn13_field sample_F_1T_1 *Specimen S (2015)*, which is depicted in figure 4.9, exhibited a hardness profile similar to that of rolled Mn13 when subjected to thermal heat. Four hardness profiles were created for analysis; one near the solidification hot crack, another near the liquation crack within a white region, and two hardness profiles at a distance of 0.1 mm from the surface to establish a stable hardness distribution between the thermal region and the bulk material. Each indentation was spaced 0.1 mm apart. The results indicated that the thermal heat received the lowest hardness within the region and increased as the depth from the surface increased. The cracks did not display any significant deviation in hardness compared to the surrounding regions within the same phase. The lowest measured hardness, recorded at 0.1 mm from the surface, was 275 HV. On the other hand, the highest hardness value, reaching 531 HV, was attained within the bulk material.

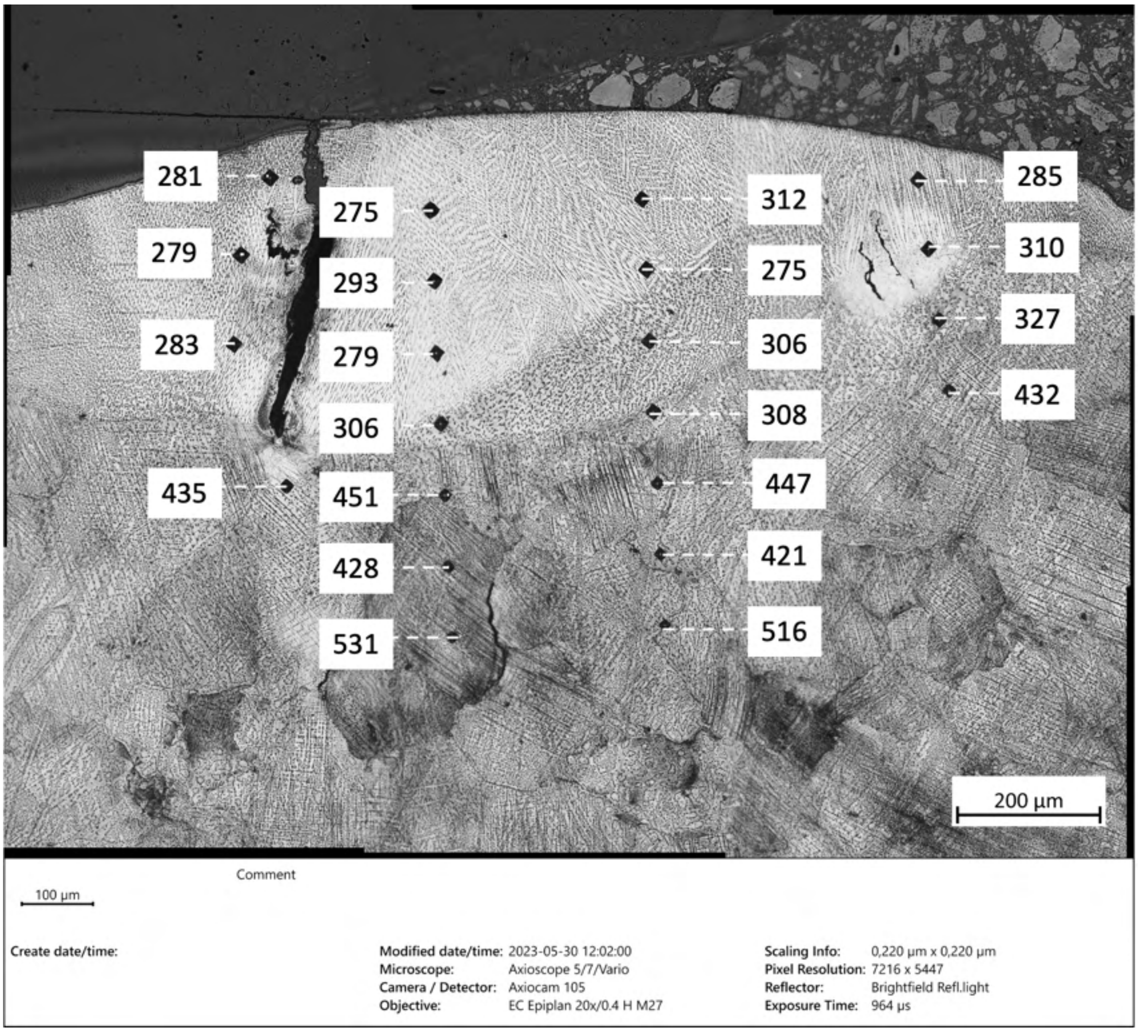

Comment

Create date/time:

Modified date/time: 2023-05-30 12:02:00
Microscope: Axioscope 5/7/Vario
Camera / Detector: Axiocam 105
Objective: EC Epiplan 20x/0.4 H M27

Scaling Info: 0,220 µm x 0,220 µm
Pixel Resolution: 7216 x 5447
Reflector: Brightfield Refl.light
Exposure Time: 964 µs

Figure 4.9: Optical microscope image of Mn13_field sample_F_1T_1 with micro-hardness indents visible, specified in HV [0.1]

4.1.11 Hardness distribution of sample Mn13_field sample F_2T_1

The hardness profile of Mn13_field sample_F_2T_1 *Specimen D (2017)* is depicted in figure 4.10. The specimen exhibited variations in hardness distribution along the hardness lines. The lowest hardness value, measured at the thermal region, was 246 HV. However, relatively lower values of 264 HV were also detected within the bulk material.

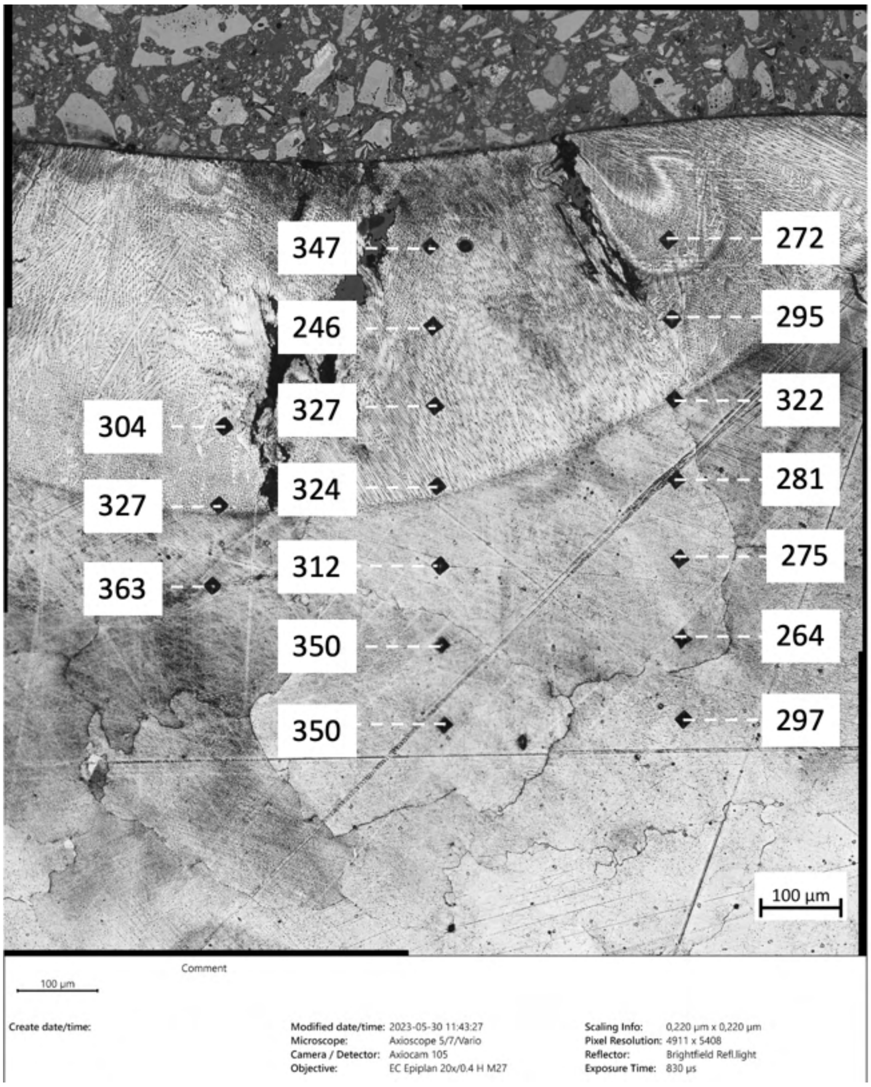

Create date/time:
Modified date/time: 2023-05-30 11:43:27
Microscope: Axioscope 5/7/Vario
Camera / Detector: Axiocam 105
Objective: EC Epiplan 20x/0.4 H M27
Scaling Info: 0,220 µm x 0,220 µm
Pixel Resolution: 4911 x 5408
Reflector: Brightfield Refl.light
Exposure Time: 830 µs

Figure 4.10: Optical microscope image of Mn13_field sample F_2T_1 with micro-hardness indents visible, specified in HV [0.1]

4.1.12 Hardness distribution of sample Mn13_field sample F_2T_2

The hardness distribution of the second sample; Mn13_-field sample F_2T_2 extracted from *Specimen D (2017)* exhibited similar behaviour to rolled Mn13. It displayed lower hardness values in the thermal region, which then increased as the distance from the surface increased. The indents were spaced 0.1 mm apart, with each indentation positioned at a distance of 0.1 mm from the surface. The hardness profile is displayed in appendix B, figure B.2, which showed two hardness profiles that illustrated this trend.

4.1.13 Hardness distribution of sample Mn13_field sample $F2T_3$

The third thermal sample extracted from *Specimen D (2017)* confirmed the previous observations, but it exhibited lower hardness values compared to the first and second samples. The hardness distribution of this sample is displayed in figure 4.11.

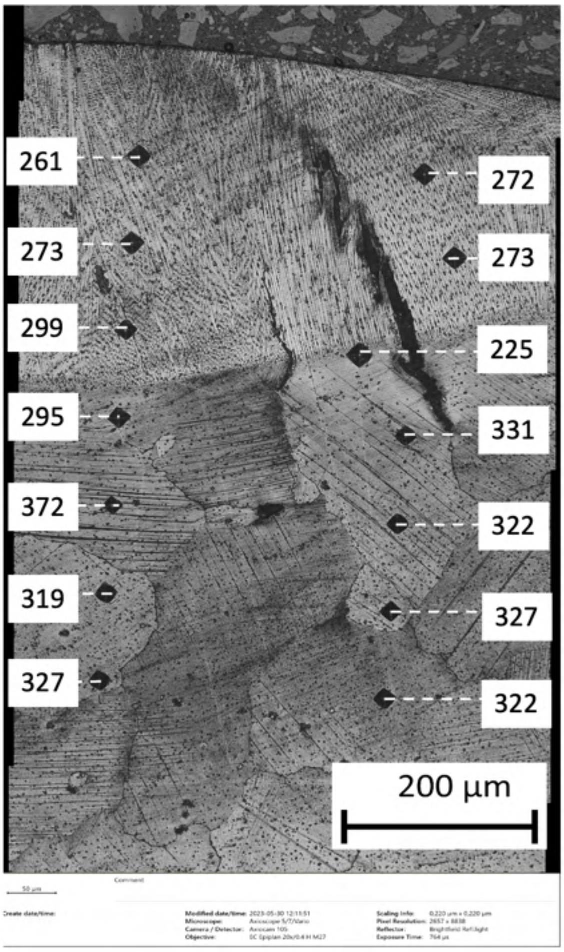

Figure 4.11: Optical microscope image of Mn13_field sample $F2T_3$ with micro-hardness indents visible, specified in HV [0.1]

4.1.14 Hardness distribution of sample Mn13_field sample_F2_M+T_1

The extracted sample, Mn13_field sample_F2_M+T_1 from *Specimen D (2017)* continued to display a low hardness distribution, as seen in figure 4.1.13, further confirming the previous observations. These samples experienced a combination of heat treatment involving a thermal pulse, as well as deformation using a Rockwell C testing indenter. However, in the case of this particular sample, the indenter was not visible. The hardness distribution of this sample is presented in appendix B, figure B.3.

4.1.15 Hardness distribution of sample Mn13_field sample_F_1_M+T_1

The second sample, Mn13_field sample_F_1_M+T_1 extracted from *Specimen S (2015)* exposed to heat treatment using a thermal pulse and experienced deformation using a Rockwell C testing indenter. Five profiles were conducted, following the same methods as previously used for samples subjected to Rockwell C testing. The hardness distribution revealed high hardness values in the deformed region, reaching up to 562 HV, as measured 0.2 mm from the surface. Additionally, one measurement outside the deformed and thermally exposed region displayed an exceptionally high value of 511 HV. In contrast, the bulk material achieved hardness values ranging from 256 to 369 HV. The hardness profile is illustrated in figure 4.12.

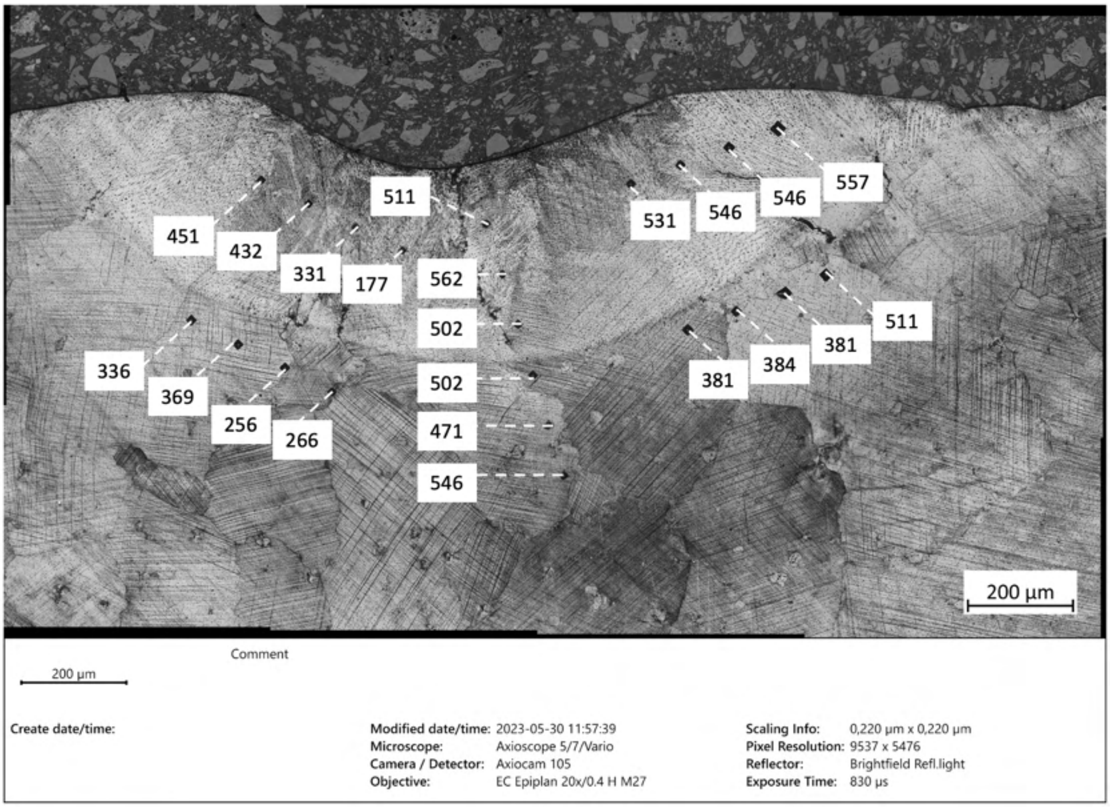

Create date/time:

Modified date/time: 2023-05-30 11:57:39
Microscope: Axioscope 5/7/Vario
Camera / Detector: Axiocam 105
Objective: EC Epiplan 20x/0.4 H M27

Scaling Info: 0,220 µm x 0,220 µm
Pixel Resolution: 9537 x 5476
Reflector: Brightfield Refl.light
Exposure Time: 830 µs

Figure 4.12: Optical microscope image of Mn13_field sample_F_1_M+T_1 with microhardness indents visible, specified in HV [0.1]

4.1.16 Hardness distribution of sample Mn13_field sample_F2_M+T_2

The second sample, Mn13_field sample_F_2_M+T_2 from *Specimen D (2017)*, which experienced a combination of a thermal pulse and deformation using a Rockwell C testing indenter, reports five hardness profiles. These profiles revealed elevated hardness values in the deformed region, reaching a maximum of 551 HV when measured at a distance of 0.1 mm from the surface. Moreover, measurements taken outside the deformed and thermally exposed region displayed higher hardness values compared to many of the hardness values within the deformed region. The hardness profile is depicted in figure 4.13.

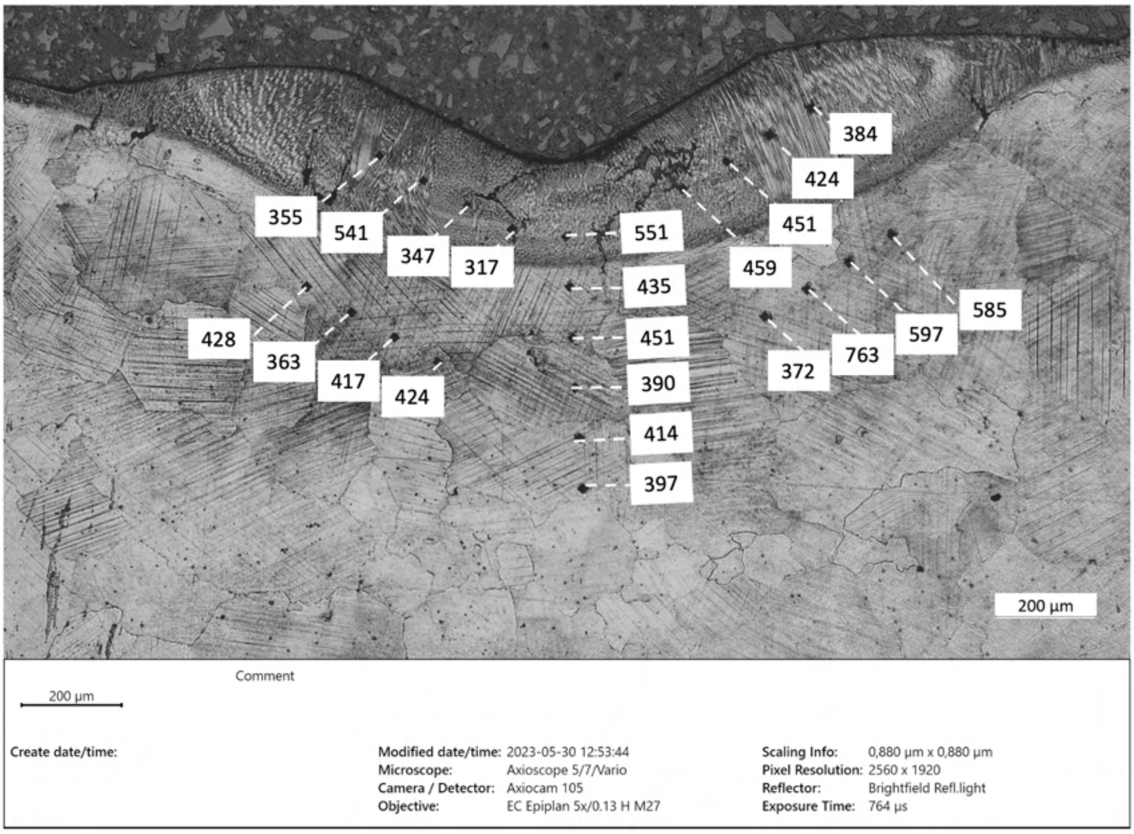

Figure 4.13: Optical microscope image of Mn13_field sample_F2_M+T_2 with microhardness indents visible, specified in HV [0.1]

4.1.17 Hardness distribution of sample Mn13_M_2

Mn13_M_2 comprised the same combination as Mn13_M_1. The hardness profile result is depicted in figure B.1. It displayed a similar pattern to the previous observations in Mn13_T+M_1 and Mn13_T+M_2, where the highest hardness was observed in the deformed region and gradually decreased with increasing distance from the deformation.

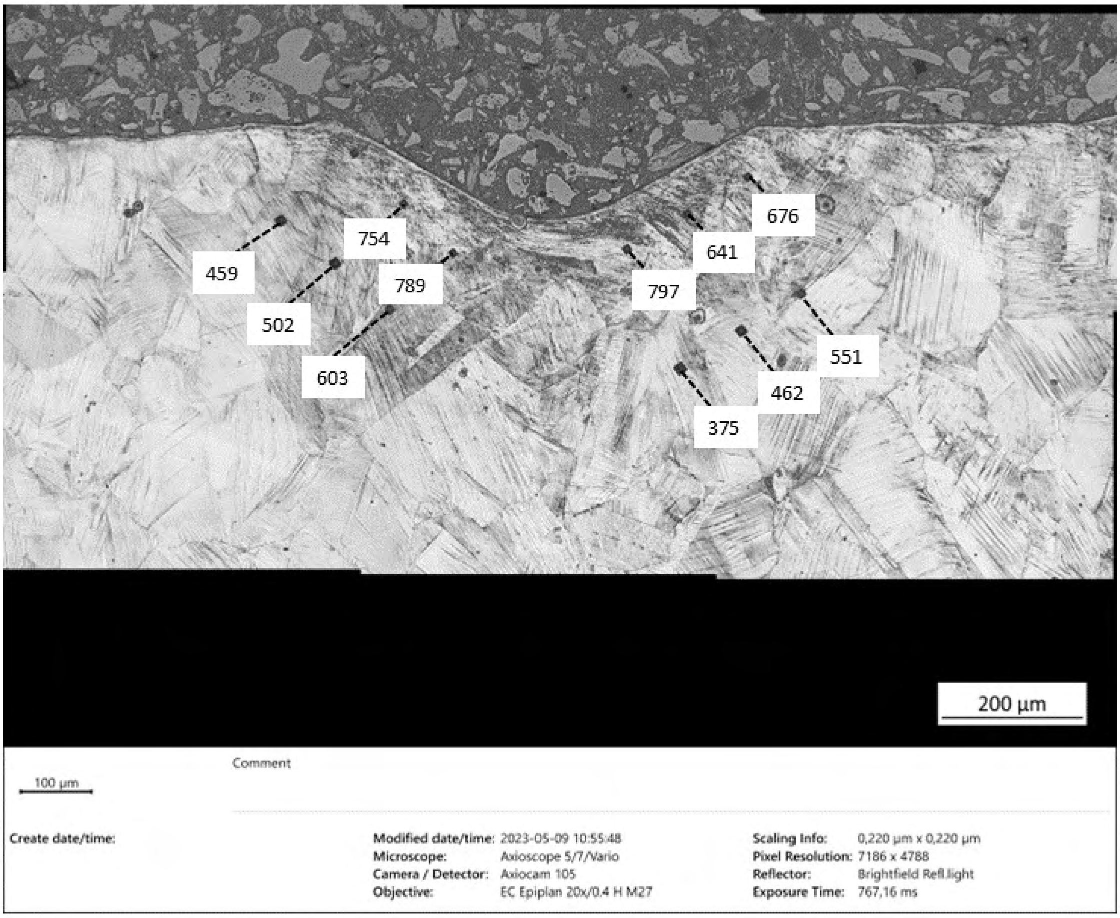

Create date/time:
Modified date/time: 2023-05-09 10:55:48
Microscope: Axioscope 5/7/Vario
Camera / Detector: Axiocam 105
Objective: EC Epiplan 20x/0.4 H M27
Scaling Info: 0,220 µm x 0,220 µm
Pixel Resolution: 7186 x 4788
Reflector: Brightfield Refl.light
Exposure Time: 767,16 ms

Figure 4.14: Optical microscope image of Mn13_M_2 with microhardness indents visible, specified in HV [0.1]

4.1.18 Hardness distribution of sample R260_V_1 and R260-V_2

The hardness profile of virgin R260 steel is depicted in figure 4.8, which shows the characteristics of an undeformed R260 sample with a thermal spot. The hardness was highest within the thermal pulse, ranging between 808 and 959 HV. As the distance from the interface between the phases increased, the hardness gradually decreased. Same behavior was observed in R260_V_2, reported in appendix B, figure B.4. Nondeformed field samples that had not been used exhibited the same pattern, with higher hardness observed within the thermal pulse, which decreased as the distance from the interface increased. The results of the hardness profiles are presented in appendix B, figure B.9, and figure B.11.

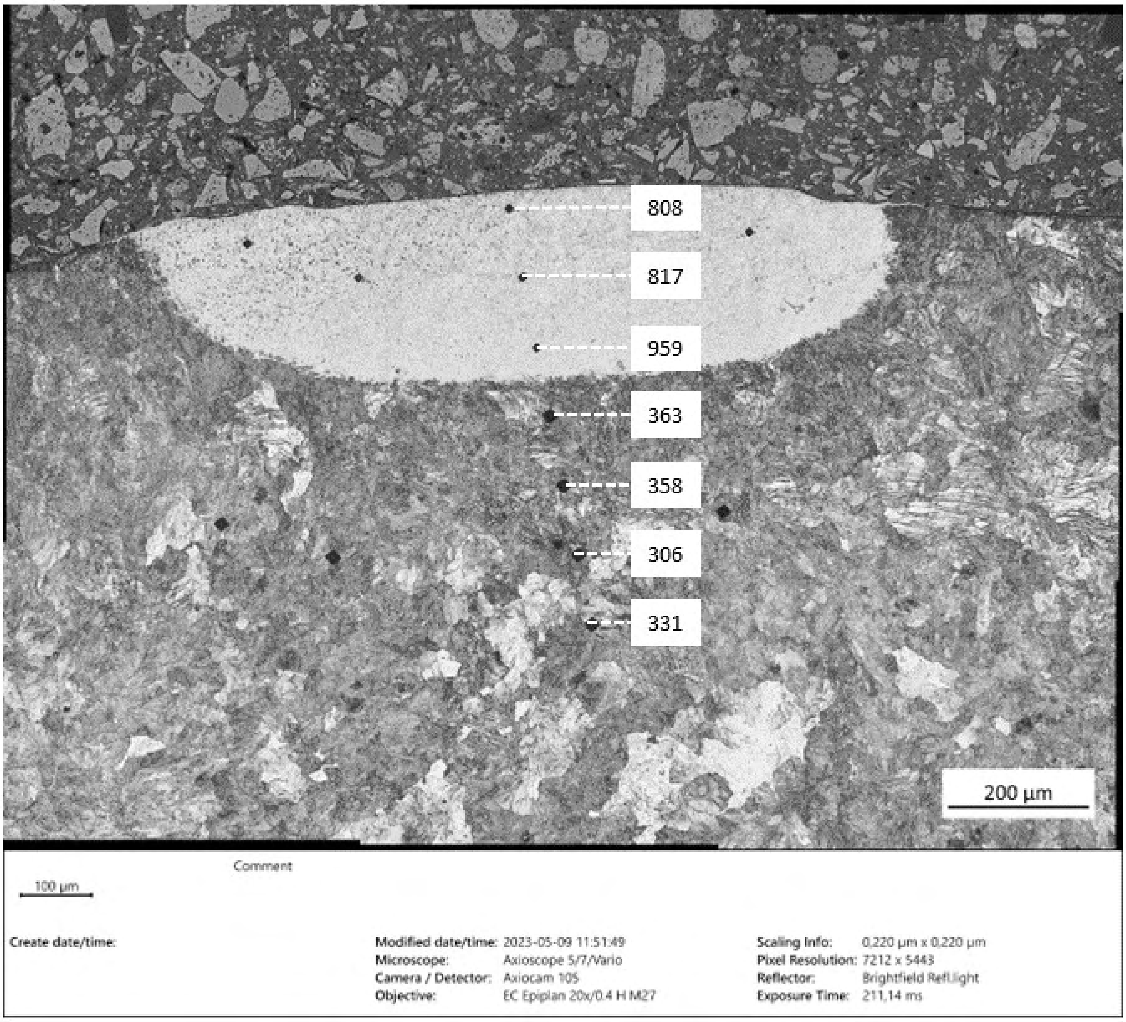

Create date/time:
Modified date/time: 2023-05-09 11:51:49
Microscope: Axioscope 5/7/Vario
Camera / Detector: Axiocam 105
Objective: EC Epiplan 20x/0.4 H M27
Scaling Info: 0,220 µm x 0,220 µm
Pixel Resolution: 7212 x 5443
Reflector: Brightfield Refl.Light
Exposure Time: 211,14 ms

Figure 4.15: Optical microscope image of R260_V_1 with microhardness indents visible, specified in HV [0.1]

4.1.19 Hardness distribution of sample R260_R9_T$_3$, R260_R9_T$_4$ and R260_R4_T$_4$

When pearlitic R260 steel was subjected to the combination of severe surface deformation and a thermal pulse, the material exhibited a hardness profile similar to that of virgin material exposed to thermal pulses. The hardness profile ranged from 971 to 361 HV. Lower values were obtained in the bulk material that had not been exposed to thermal heat. Hardness profiles for this combination can be found in appendix B, figure; B.5, B.6, and B.7.

4.1.20 Hardness distribution of sample R260_R4_M$_1$ and R260_F_M$_1$

Sample R260_R4_M$_1$ exposed to a combination of severe surface deformation and mechanical impact by a Rockwell C indenter. The hardness profile is presented in appendix B, figure B.8. The hardness profile exhibited similarities with the previously mentioned trend of higher hardness near the deformed surface, which decreased as the distance from the deformation increased. This trend also aligned with the findings from a non-deformed field sample subjected to mechanical impact. The hardness profile revealed the highest hardness values closest to the surface. However, in the case of R260_F_M$_1$, the measured hardness was higher compared to the previously mentioned samples. Near the surface, the hardness reached 837 HV, while outside the deformed region, it was measured at 447 HV. The hardness profile is shown in figure 4.16.

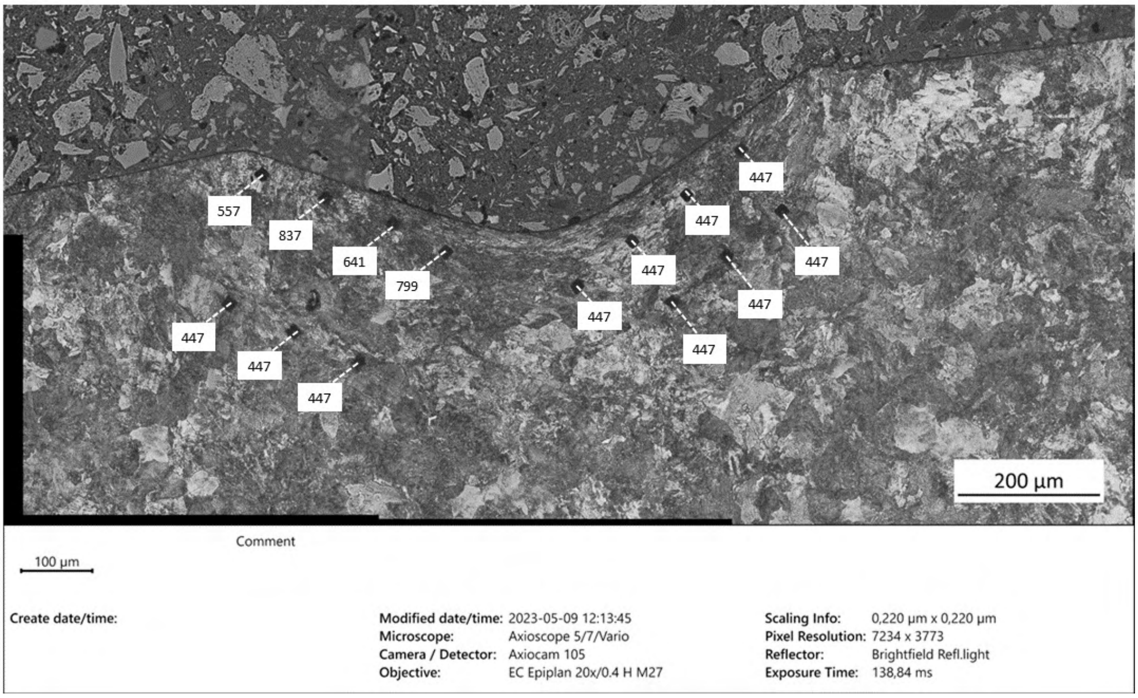

Create date/time:

Modified date/time: 2023-05-09 12:13:45
Microscope: Axioscope 5/7/Vario
Camera / Detector: Axiocam 105
Objective: EC Epiplan 20x/0.4 H M27

Scaling Info: 0,220 µm x 0,220 µm
Pixel Resolution: 7234 x 3773
Reflector: Brightfield Refl.light
Exposure Time: 138,84 ms

Figure 4.16: Optical microscope image of R260_F_M$_1$ with microhardness indents visible, specified in HV [0.1]

4.2 Results of Microstructure Analysis

Below the microstructure of both steels is shown. The result shows the impact of thermal pulses on *non-deformed* and *severely deformed surface.*

Microstructure analysis was performed on the following combinations:

- Effects of thermal pulse on virgin material
- Effects of thermal pulse on severely deformed surfaces
- Effects of thermal pulse on field samples that were unused and had defects

4.2.1 Microstructure analysis of sample Mn13_V_1

Virgin material from Mn13 steel was exposed to a thermal pulse, and the microstructure is displayed in figure 4.17. It revealed a combination of columnar and dendritic structures in the fusion zone where the thermal pulse had been initiated. The material had been selected from a virgin sample without any pre-deformation, as indicated by the absence of visible slip bands or deformation twins in the bulk material's grains. However, upon exposure to thermal heat, segregated carbides accumulated at both grain boundaries and in the heat-affected zone of Mn13_V$_1$.

Create date/time:

Modified date/time: 2023-05-04 11:47:24
Microscope: Axioscope 5/7/Vario
Camera / Detector: Axiocam 105
Objective: EC Epiplan 20x/0.4 H M27

Scaling Info: 0,220 µm x 0,220 µm
Pixel Resolution: 11813 x 3775
Reflector: Brightfield Refl.light
Exposure Time: 119,94 ms

Figure 4.17: Microstructure of Mn13_M5_V1

Clarification of the result in figure 4.17 from sample Mn13_V_1 is provided in 4.18. Figure 4.18 presented visible observations of transverse and parallel dendritic grains. Additionally, columnar grains were observed in parallel to the image. The figure also depicted black dots, which were residues from diamond suspension, presumably originating from OPS. These residues were visible within the fusion zone, at the heat-affected zone (HAZ), and within the bulk material.

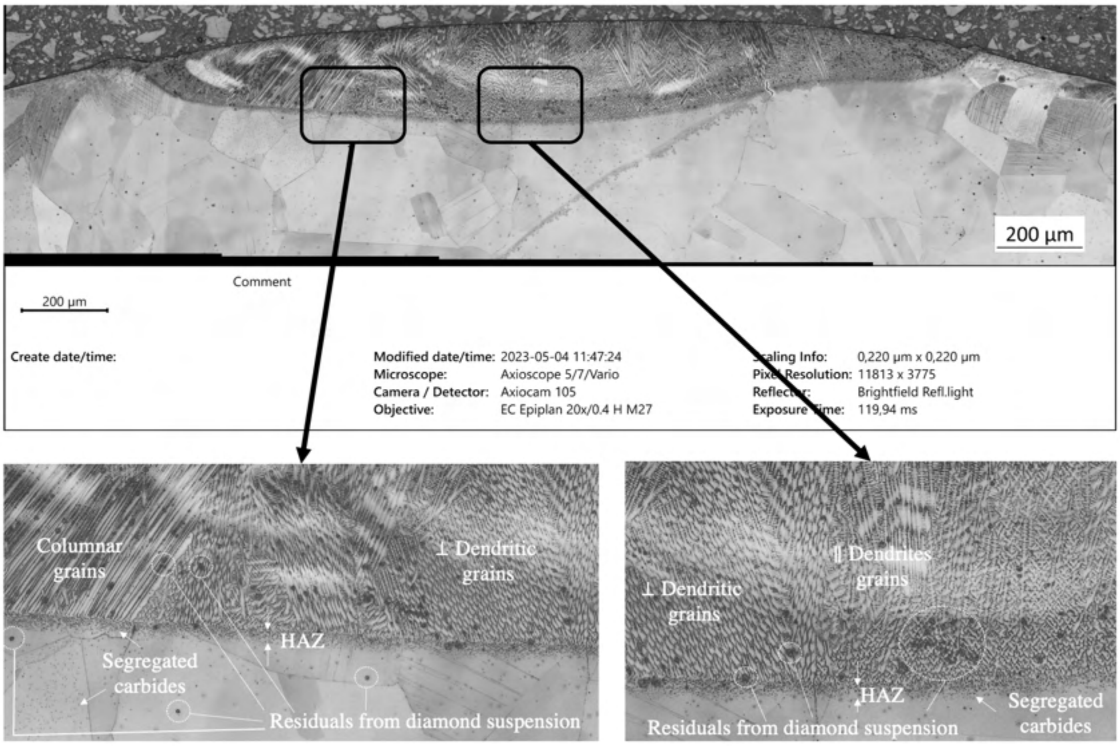

Create date/time:

Modified date/time: 2023-05-04 11:47:24
Microscope: Axioscope 5/7/Vario
Camera / Detector: Axiocam 105
Objective: EC Epiplan 20x/0.4 H M27

Scaling Info: 0,220 µm x 0,220 µm
Pixel Resolution: 11813 x 3775
Reflector: Brightfield Refl.light
Exposure Time: 119,94 ms

Figure 4.18: Explanations of the microstructure from Mn13_M5_V1

4.2.1.1 Mn13, liquidus crack

Defects were observed in sample 4.2.1. At the interface between the thermally exposed region and the bulk material, a visible liquidus crack was present, as depicted in appendix D, figure D.1. The observed crack was positioned between the grains in both the thermally exposed region and the non-exposed material. Furthermore, around the heat-affected zone (HAZ), two potential fine liquidus cracks were observed.

4.2.2 Microstructure analysis of sample Mn13_V_2

The second sample, Mn13V_2, extracted from the virgin material, exhibited an increase in slip bands, even though it had not undergone the same biaxial twisting deformation as the other samples. The thermal spot was applied to the grip section of the undeformed material; the observed deformation is a consequence of prior mechanical impact that had deformed the material at some stage. The result is reported in appendix D, figure D.2. The result shows slip bands in the microstructure, although not as distinct as in the predeformed samples; for instance, figure 4.19. Mn13_V_2 displayed similar characteristics to Mn13_V_1, with dendritic and columnar grains observed at the fusion zone. Carbides were accumulated and segregated between the grains and in the HAZ. It is worth noting that a small indent was visible on the surface, but this was not a defect resulting from solidification, as seen in other samples.

4.2.3 Microstructure analysis of sample Mn13_T$_3$

The first sample, extracted from a combination of thermally and predeformed material, exhibited a microstructure similar to the virgin samples. The microstructure of Mn13_T$_3$ is reported in figure 4.19. However, a significant increase in slip bands was observed in the bulk material. Apart from this increase in slip bands, the microstructure appeared consistent, characterised by dendrites and columnar grains in the fusion zone, along with segregated carbides accumulated between the grains and within the HAZ. Unlike the first extracted virgin samples, no visible liquidus cracks were present in this sample.

Comment

Create date/time:

Modified date/time: 2023-05-04 11:33:46
Microscope: Axioscope 5/7/Vario
Camera / Detector: Axiocam 105
Objective: EC Epiplan 20x/0.4 H M27

Scaling Info: 0,220 µm x 0,220 µm
Pixel Resolution: 11833 x 3782
Reflector: Brightfield Refl.light
Exposure Time: 119,94 ms

Figure 4.19: Microstructure of Mn13_M5_T$_3$

4.2.4 Microstructure analysis of sample Mn13_T$_4$

Mn13_T$_4$ was the fourth sample, which was exposed to a thermal pulse on a predeformed surface. The sample exhibited poor etching, resulting in difficulties in interpreting the microstructure. While the bulk material displayed visible slip bands, the area exposed to the thermal pulse was contaminated with residues from OPS, which hindered clear observation. However, in certain regions, the microstructure was consistent with the other samples subjected to the thermal pulse, characterised by the presence of columnar and dendritic grains in the fusion zone. The HAZ could not be determined. The corresponding figure can be found in appendix D, figure D.4.

4.2.5 Microstructure analysis of sample Mn13_T$_5$

The microstructure of Mn13_T$_5$ also exhibited poor etching, with residues from OPS hindering clear visualisation of the microstructure. However, it was still evident that the microstructure followed the same pattern observed in the previous samples examined from Mn13. The HAZ could not be determined. The corresponding figure can be found in appendix D, figure D.5.

4.2.5.1 Mn13, hot cracking

Solidification hot cracks were visible in all Mn13 samples, including the field samples. Although the cracks may not have been apparent in all micrographs. The cracks were observed in the stereo optical microscope before the samples were cut, as depicted in figure 2.13 in appendix C. Images were captured at the surface after the thermal pulse revealed the presence of solidification hot cracks. Notably, the Mn13 sample labelled as Mn13_T_5 displayed a visible solidification hot crack in its mimeographs from LOM, prompting further investigation using a scanning electron microscope (SEM) to confirm its origin as a solidification hot crack.

The SEM images depicted four instances of solidification hot cracks in various field samples, as shown in figure C.1 in appendix C. These cracks originated from the outer edge of the thermal heat pulse and extended toward the center. An image demonstrated the positioning of the indentation in these samples and the continued presence of cracks afterwards. Upon closer examination, the SEM observations revealed the appearance of the cracks at higher magnification, exhibiting the direction of solidification and shrinkage. Additionally, a significant accumulation of segregated carbides was visible, particularly in the thermal heat pulse and around the grains closest to the solidification hot crack. Further magnification revealed the presence of smaller hidden cracks in the region, which also exhibited an increased proportion of carbides. The area closest to the surface was susceptible to the accumulation of segregated carbides as well. Figure 4.20 *a*) displayed the largest crack, while figure 4.20 *b*) presented additional cracks near the surface. Furthermore, figure 4.21 *a*) displayed the middle section of the crack, and 4.21 *b*) showed the end of the crack, located closest to the interface between the phases.

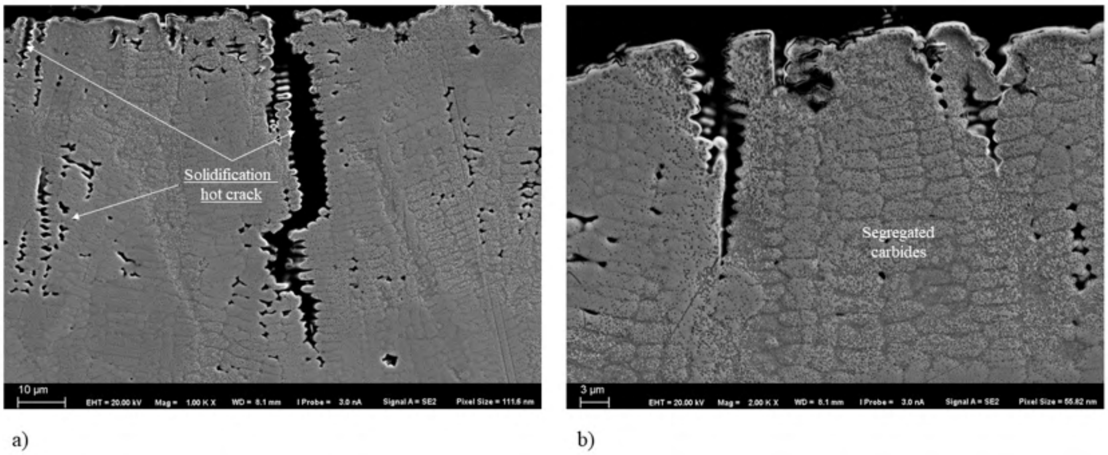

Figure 4.20: Two solidification hot cracks performed via SEM for Mn13-T_5

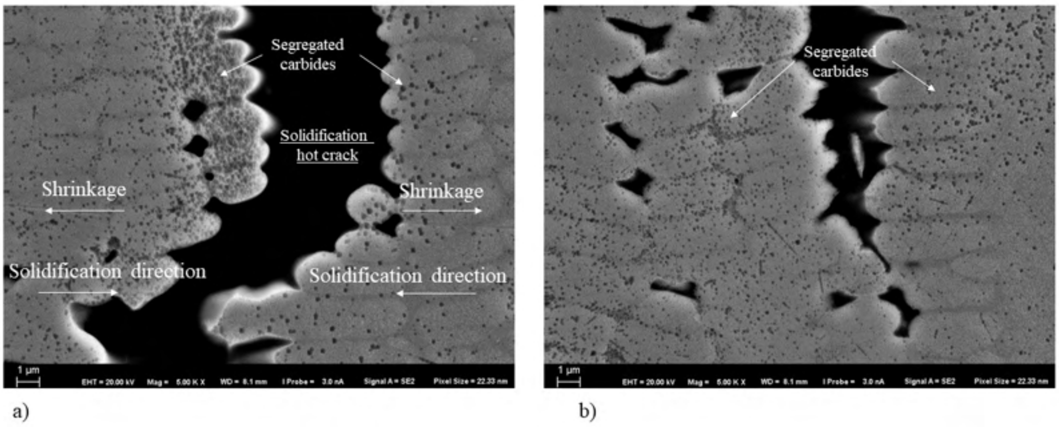

Figure 4.21: Solidification hot crack a) at the middle b) at the end near the interface between the phases for Mn13-T_5

4.2.6 Microstructure analysis of sample Mn13_field sample F_1T_1

From the specimen labelled as Mn13_field sample F_1T_1 extracted from *Specimen S (2015)*, the material that was subjected to one thermal pulse is shown in figure 4.23. The material exhibited a microstructure similar to rolled Mn13 when exposed to a thermal pulse. The fusion zone displayed a combination of columnar and dendritic grains. In figure 4.23, epitaxial growth was evident, as the grains in the fusion zone grew in the same direction as the preexisting grains within the bulk material close to the melt pool. While the HAZ was not clearly visible due to poor etching. significant defects were present in the sample, in the thermal region, a large solidification hot crack was observed, penetrating from the surface down to the interface of the bulk material. The crack was further examined using SEM, as depicted in figure 4.24, 4.25, and 4.26. Additionally, there were visible liquidus cracks at one location at the interface of the partially melted zone (PMZ). It could be observed that a crack below the thermal spot was present around the grain boundaries, as seen in figure 4.22.

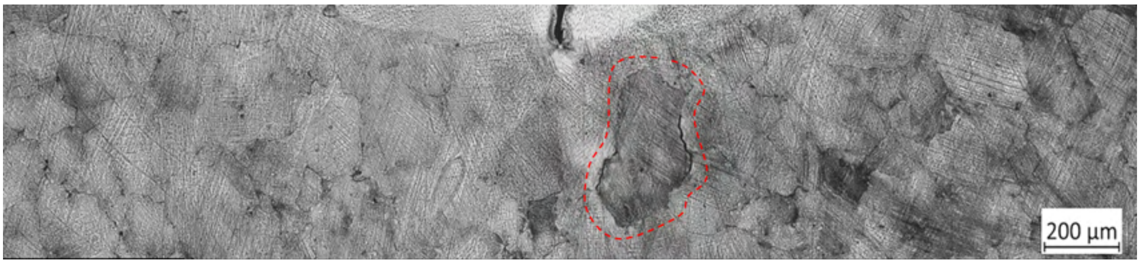

Figure 4.22: Crack around the grain boundaries in the bulk material for sample Mn13-field sample F_1T_1

Since this sample was extracted from a damaged turnout, deformation from mechanical impact was observed in the microstructure of the bulk material. A high percentage of slip bands were detected, especially closest to the surface of the sample.

Create date/time:
Modified date/time: 2023-05-30 09:15:51
Microscope: Axioscope 5/7/Vario
Camera / Detector: Axiocam 105
Objective: EC Epiplan 20x/0.4 H M27
Scaling Info: 0,220 µm x 0,220 µm
Pixel Resolution: 14131 x 5537
Reflector: Brightfield Refl.light
Exposure Time: 3,1 ms

Figure 4.23: Microstructure of Mn13-field sample F1T1

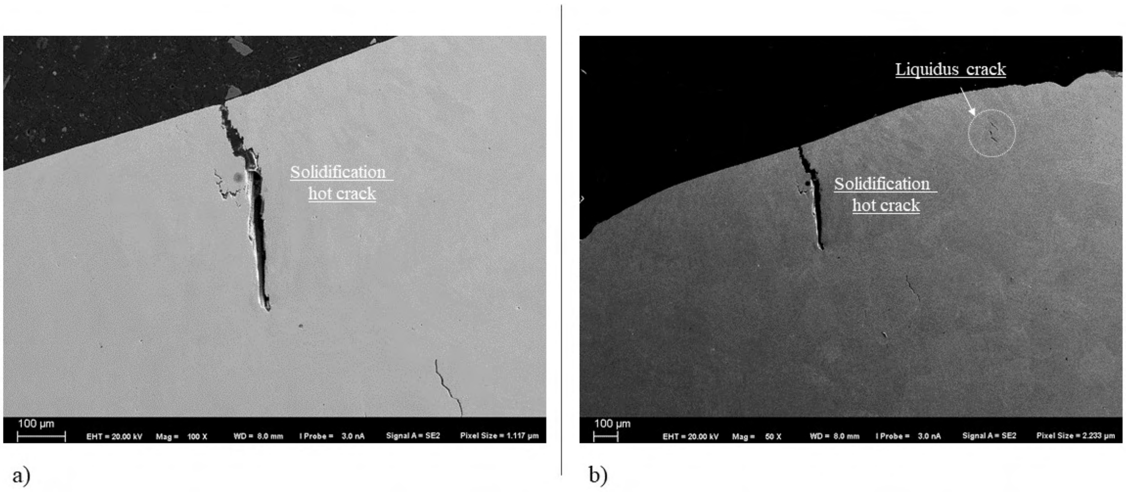

EHT = 20.00 kV Mag = 100 X WD = 8.0 mm I Probe = 3.0 nA Signal A = SE2 Pixel Size = 1.117 µm

EHT = 20.00 kV Mag = 50 X WD = 8.0 mm I Probe = 3.0 nA Signal A = SE2 Pixel Size = 2.233 µm

a) b)

Figure 4.24: Solidification cracks of Mn13-field sample F1T1 performed via SEM

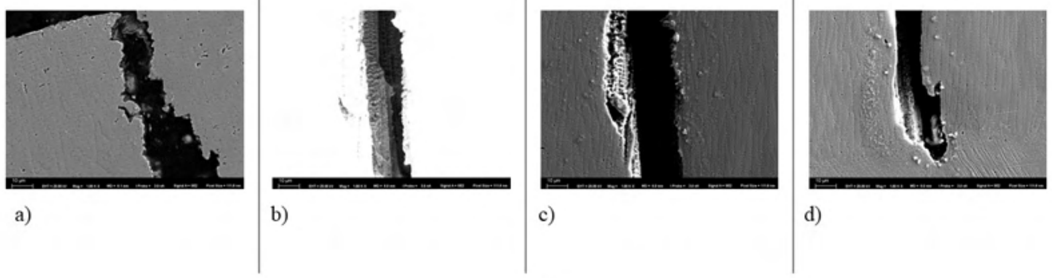

Figure 4.25: Different sections of solidification cracks of Mn13-field sample F1T1 performed via SEM

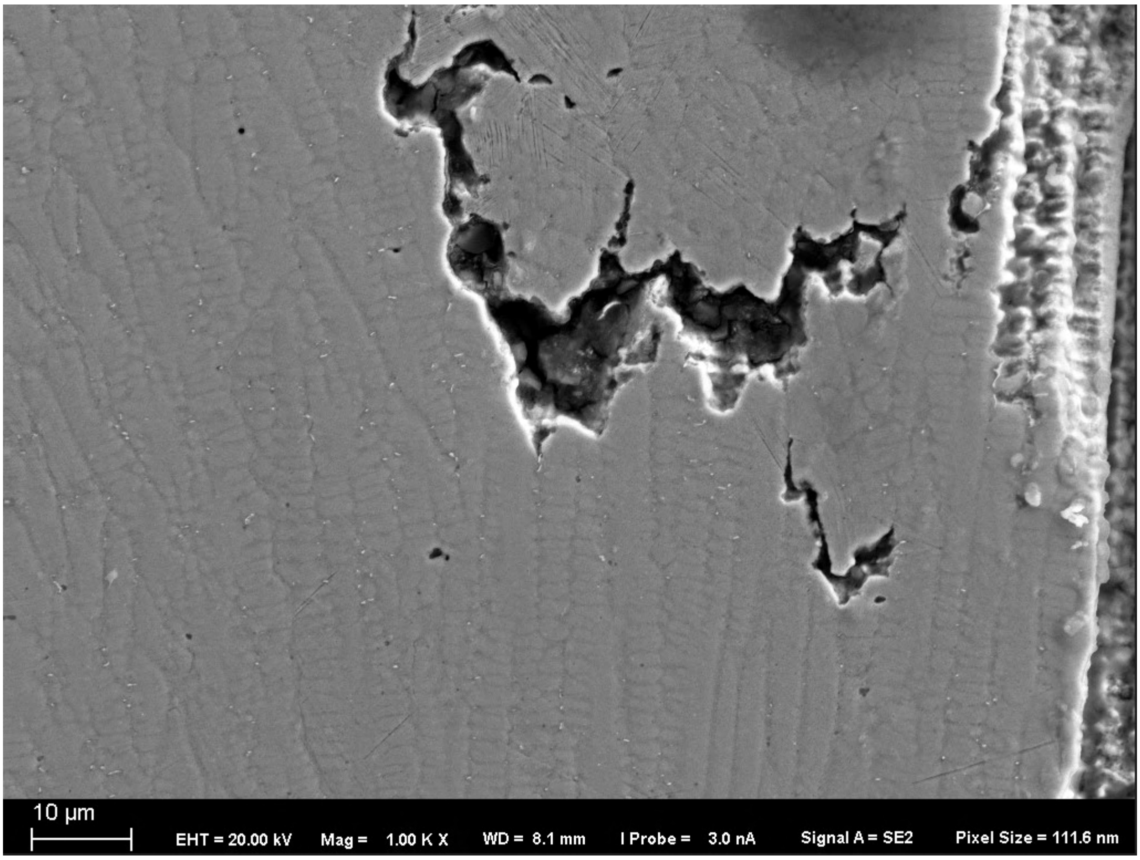

Figure 4.26: Branching of solidification hot crack of Mn13-field sample F1T1 performed via SEM

4.2.7 Microstructure analysis of sample, field samples

The other samples extracted from *Specimen S (2015)* and *Specimen D (2017)* are document appendix D and depicted in figure D.10 to D.14. The microstructure of these samples did not show any significant variation and remained similar to each other, including the observed defects. The samples were obtained from both the flat and curved sides of the turnout, and no notable differences were observed based on the sampling location.

4.2.8 Microstructure analysis of sample R260

The microstructure remained unchanged regardless of whether the samples underwent predeformation or were taken from the bulk material. Similarly, no significant differences were observed in the microstructure of the field sample. During the thermal pulse, the formation of WEL was evident, aligning with previous studies. The thermal pulse also led to the presence of martensite, as indicated by the substantial increase in hardness.

Figure 4.27 shows a virgin sample extracted from the bulk material subjected to a thermal pulse, and figure 4.28, represents the predeformed material subjected to a thermal pulse. Despite the difference in size, both images exhibited the same microstructure. However, it should be noted that the presence of white spots in figure 4.28 indicated uneven etching. The remaining microstructures of the samples extracted from R260 are presented in appendix D, figure D.17 to D.22.

Create date/time:
Modified date/time: 2023-04-28 14:18:00
Microscope: Axioscope 5/7/Vario
Camera / Detector: Axiocam 105
Objective: EC Epiplan 20x/0.4 H M27
Scaling Info: 0,220 µm x 0,220 µm
Pixel Resolution: 14117 x 3808
Reflector: Brightfield Refl.light
Exposure Time: 100,02 ms

Figure 4.27: Microstructure of R20_R9_V_1

Create date/time:
Modified date/time: 2023-04-28 14:35:47
Microscope: Axioscope 5/7/Vario
Camera / Detector: Axiocam 105
Objective: EC Epiplan 20x/0.4 H M27
Scaling Info: 0,220 µm x 0,220 µm
Pixel Resolution: 14119 x 3808
Reflector: Brightfield Refl.light
Exposure Time: 100,02 ms

Figure 4.28: Microstructure of R20_R9_T_3

4.3 Thermal width and dept dimensions

Table 4.2 presented measurements of various dimensions resulting from laser welding exposure, HAZ, and the width and depth of the fusion zone for each sample. The measurements are reported in table 4.2 and the results from the settings defined in chapter 3 were a spot diameter of 2 mm whit a flat power profile. *Error* indicates samples that could not be measured.

Table 4.2: Dimensions of HAZ and fusion zone

Material_Sample	HAZ [nm]	Pulse width [μm]	Pulse depth [μm]
Mn13_V_1	18100	2072	228
Mn13_V_2	9700	1980	261
Mn13_T_3	21300	2005	233
Mn13_T_4	error	error	error
Mn13_T_5	error	error	error
Field sample Mn13_F1T_1	error	>2207	444
Field sample Mn13_F2T_1	18764	2334	344
Field sample Mn13_F2T_2	13997	2375	437
Field sample Mn13_F2T_3	17824	2395	380
R260_R9_V_1	0	1067	267
R260_R9_V_2	20641	error	285
R260_R9_T_3	0	2118	363
R260_R4_T_4	0	1588	158
Field sample R260_T_1	0	2253	463

5

Discussion

This chapter is dedicated to discuss the results obtained from the study and analysing the potential factors that could have influenced these findings. It incorporates supporting evidence from the theoretical framework in chapter 2. The investigation provides a comprehensive examination of the microstructure and the hardness profiles. Moreover, since the results indicate the presence of defects, the associated discussion addressing these defects is also included.

5.1 Hardness

The hardness of R260 steel was observed to increase when it was subjected to thermal exposure, indicating a phase transformation from pearlite to martensite. Previous studies suggested that the high temperature gradient during the thermal pulse led to self-cooling of the material, facilitating martensite formation [3]. The conclusions drawn from these conducted tests were consistent with the previously mentioned observations, where the increase in hardness associated with martensite formation was evident [7]. However, it was noted in the report that the presence or absence of deformation after the thermal pulse did not significantly affect the hardness, as the region of the thermal pulse converted all phases into martensite.

In accordance with the established theory, the hardness values obtained in this study align with previous research on the WEL. The hardness range of 700-1200 HV [7] reported in earlier studies is consistent with the findings from the hardness profiles in this investigation.

The hardness of Mn13 steel was observed to increase when it was subjected to a thermal pulse and subsequently deformed by mechanical impact, specifically through Rockwell C testing. The formation of new grains during solidification was characterised by dislocation-free grains, which contributed to lower hardness. However, when the material was exposed to mechanical impact, the deformation caused the newly formed grains to experience strain and an increase in the insertion of dislocations, consistent with the theory of dislocation density increase in work hardening [62]. This cold processing of the material in the deformed area altered its properties, resulting in an increase in hardness due to large plastic strains locally. This observation is in line with previous studies that demonstrated an increase in hardness through gradual impact with Mn13 [2].

Deformation in the form of slip band initiation prior to the thermal pulse did not impact the hardness of the material, except in the bulk material. This observation suggested that the material transformed from a solid austenitic phase to a molten state. Austenitic manganese steel is known to exhibit a low solidification rate, leading to the formation of defects such as carbide segregation and welding defects [49]. Consequently, upon completion of the solidification process, the material tended to exhibit lower hardness. However, the hardness profiles might have displayed divergent values due to the formation of carbides, which possessed significantly higher hardness than the surrounding bulk material [31] [32]. When hardness tests were conducted on these carbides, they contributed to an increase in local hardness at the testing point, thereby yielding somewhat misleading results. The SEM images in figures 4.20 and 4.21 provided clear evidence of carbide segregation and accumulation at the grain boundaries, particularly along the secondary dendritic arms near the solidification hot crack and close to the surface, during the thermal pulse. These regions exhibited a significant concentration of carbides, surpassing that of the surrounding material. As a result, localised changes in hardness occurred in these specific areas due to the pronounced accumulation of carbides.

As a result of the formation of columnar and dendritic grains, Mn13 exhibited anisotropic properties, with dominance in a specific direction, as supported by [38]. This characteristic had significant implications from an operational standpoint, as the material could deviate from its intended properties. Consequently, it was advised against welding Mn13, and alternative materials, such as certain types of stainless steel, were used for connections to prevent the material from melting.

To accurately assess the hardness distribution of Mn13, it is essential to conduct a comprehensive mapping of both vertical and longitudinal hardness profiles. This mapping approach would have enabled better visualisation of variations across the material's profile. However, instead of performing this thorough analysis, only two line profiles were typically conducted, with roughly equal distances from the surface. This limited approach failed to capture the full extent of variations in the material's hardness properties.

5.2 Microstucture

Previously, it was mentioned that R260 transforms to martensite, which was evident through the occurrence of WEL formation. The figures obtained from R260 clearly demonstrated this phenomenon, indicating that the application of thermal heat to R260 resulted in a phase transformation. However, due to the etching process, the bulk material became challenging to analyse as it appeared very dark. No discernible HAZ was observed at the interface between the bulk material and the fusion zone. The material within the fusion zone displayed a consistent microstructure characterised by the presence of martensite. In comparison to Mn13, none of the R260 samples showed cracking in the form of solidification hot cracks or liquation cracks. In one of the R260 samples, a crack was observed that penetrated from the surface into the bulk material, as seen in figure D.17 in appendix D.

Previously, it was established that R260 undergoes a martensitic transformation, resulting in the formation of a white layer known as the WEL on the surface. According to existing literature, the formation of martensite typically occurs based on prior austenitic grains [23]. However, the figures provided by OM do not reveal this phenomenon.

Based on the previous statements, the formation of WEL could be attributed to either martensite [3] or nanocrystalline martensite [5]. In the present case, the transformation aligned with the hypothesis from [3], where the phase change was induced by heating and rapid cooling. The hypothesis from [5], which proposed that "repeated plastic deformations leading to increased strain in the cementite along with grain refinement, resulting in a nanocrystalline microstructure," remained untested and could not be verified based on the obtained results.

During the thermal pulse of Mn13 steel, the material transformed from solid austenite to a molten state and surface melting are reported from the findings are evident. Subsequently, the cooling process took place slower than in R260, facilitating the growth of dendritic and columnar grains originating from the weld pool. These observations aligned with the findings from previous studies in [2]. The growth of the newly formed grains occurred from the austenitic grains present at the interface with the molten material, a phenomenon known as epitaxial growth. The slow solidification rate allowed for the diffusion of carbon within the material. As solidification progressed, carbon present in the steel diffused and migrated away from the solidifying grains into the surrounding liquid. However, as the solidification process neared completion, the diffusion of carbides became restricted, resulting in their fixation around the secondary dendritic arms.

It was worth noting that these observed defects could potentially be attributed to manufacturing techniques and specimen shape. The field samples were manufactured by casting and obtained a flatter profile. Consequently, when the laser was applied, it could directly impact the surface without deviation, exposing the entire laser spot perpendicular to the surface. On the other hand, the specimens produced through rolling were typically circular specimens with a diameter of a few millimeters. When the laser interacted with these specimens, there was a possibility of deflection or interference, potentially affecting the initiation process. Given the multifaceted nature of the issue, it could only be speculated that these factors may have had an impact on the observed outcomes.

Slip bands and deformation twins affect recrystallisation. In the HAZ small grains were visible in one sample, indicating that recrystallisation had occurred. However, in the other samples where predeformation was present, this phenomenon could not be observed due to uneven etching. But it aligns with earlier statements of nucleation sites [14].

The crystal structure in R260 was observed to transform from ferrite and cementite to a BCT crystal, as indicated in [24]. However, in the case of Mn13, the initial determination of the crystal structure as FCC could not be substantiated using the methodology employed in this investigation. Therefore, further research is required to determine whether the crystals have undergone transformation or if only the microstructure has been affected. The current status of this matter remains unresolved.

5.2.1 Defects

Defects in the form of solidification cracks were observed in all Mn13 samples, including both rolled test bars and cast field samples. Previous literature had already established the poor weldability of Mn13 due to its high coefficient of thermal expansion and slow solidification rate, as discussed in [2]. As the material heated up, its volume expanded, but during solidification, it experienced shrinkage, a phenomenon referred to as intrinsic restraint [45], indicating opposing movements between shrinkage and solidification as depicted in figure 2.13. This phenomenon increased the probability of solidification hot cracks, which are cracks formed due to incomplete bonding of the material. Examination of the crack appearance through SEM, figure; 4.20, 4.21, 4.25, and 4.26 revealed the presence of dendritic secondary arms, suggesting shrinkage during the solidification process. This phenomenon was also observable in OM of the field samples. Furthermore, hardness testing conducted around the cracks on selected field samples showed no significant differences along the line profiles, indicating that no other types of cracking existed apart from voids created during solidification. The hardness profile around the crack is presented in figure 4.9. Additionally, smaller types of solidification hot cracks or incomplete fusion could be observed through SEM, as shown in figure 4.20. However, these cracks or voids were not studied based on hardness tests due to their small size, which could not be detected under the magnification used, but they became visible when using SEM.

Solidification hot cracks are commonly manifested in materials characterised by low thermal conductivity and high thermal expansion [46]. It is noteworthy that Mn13 exhibited low thermal conductivity [30], implying that the presence of slow solidification combined with thermal expansion was more likely to render defects visible. Previous studies demonstrated that the occurrence of cracks was not solely reliant on welding speed and solidification rate but also influenced by alloying elements with low melting temperatures, the presence of microcavities facilitating microcrack nucleation, and the misorientation of grains characterised by high-angle boundaries [46].

Distinct variations were observed in the appearance of cracks between field samples and cylindrical test bars. As mentioned earlier, sample preparation significantly impacted the examination since the samples were not analysed at the center but rather within the thermal pulse region. Nevertheless, cracks were visible in materials where deformation was initiated, thus speculating on the potential impact. Shear stresses induced atomic plane displacements during twisting, leading to increased dislocation density, initiation of slip bands, and formation of deformation twins, as per theoretical understanding. The extent to which atomic displacement affected misorientation was challenging to determine, and grain orientation may have remained unchanged among the original grains tested.

The grain shape, both before and after deformation, remained uniform; however, the grains experienced deformation and might have undergone grain refinement during heat treatment due to recovery and recrystallisation, resulting in the emergence of new grain boundaries with partially altered grain orientation. Nonetheless, perhaps the most significant influence on solidification hot cracking lay in the presence of finer grains, nearly dislocation-free grain, which experienced shrinkage in the opposite direction to the solidification direction.

Liquation cracks were observed at the interface between the PMZ and the HAZ, both in field samples and test bars. Typically, these cracks were associated with multipass welds or reheated welds [45], but such explanations were insufficient in this case as the weld consisted of a single thermal pulse that penetrated the surface only once. The presence of liquation cracks was observed in both virgin materials and used field samples, suggesting that they occurred independently of the material's origin. The crack was likely a consequence of the contrast in tension between the liquified and solidified PMZ, as suggested by [47]. It could have been a combination of stresses resulting from variations within the PMZ between the solidified and liquid metal, along with stresses arising from the expansion of the liquid in the fusion zone.

5.3 Thermal width and depth

Several of the values presented in table 4.2 could not be accurately measured due to inadequate and incorrect etching procedures, resulting in unclear boundaries between distinct zones. The table exclusively displayed thermal pulse values, as the other pulses had been distorted and lacked substantial data. Fluctuations in the fusion zone's size could be attributed to the pulse, not being entirely centered or cut. Values below 2 mm could be considered off-center, whereas values exceeding 2 mm exhibited deviations in the welding equipment.

6

Conclusion and future work

The conclusion encompassed the outcomes of the project's inquiries and highlighted any areas for future investigation aimed at gaining a deeper understanding of the obtained results and the materials involved. The following were the key conclusions derived from the results presented in Chapter 4.

Conclusions:

- Mn13 experiences significant changes when subjected to thermal impact. The microstructure of Mn13 revealed a combination of dendritic and columnar grains that exhibited directional growth from the grains at the interface toward the molten region. Carbide segregation was evident around the dendritic secondary arms and along the HAZ.

- Recrystallisation was only visible in one sample, Mn13_T_3, which was subjected to thermal pulse on a deformed surface. No other images showed this phenomenon, likely due to poor and uneven etching. However, Mn13_V_1 was well etched, and there was no sign of recrystallisation. From this, it can be deduced that slip bands provide sites for recrystallisation. However, to confirm this, several samples need to yield the same result.

- The hardness profiles suggested that the grains formed in the thermal zone were nearly free from dislocations. This conclusion was supported by the significant decrease in hardness observed after the thermal pulse. It was expected that new grains would be formed during melting, which would not possess defects such as dislocations unless the material was exposed to mechanical impact.

- The HAZ in Mn13 showed an increased presence of carbide segregation, but the grains in close proximity to the segregated carbides appeared unchanged compared to virgin state.

- Mn13 and R260 were found to be distinct materials that exhibited significant differences in their response when subjected to a thermal pulse. Phase transformation was observed in R260, with a transition from pearlite to martensite, resulting in a substantial increase in hardness up to 1000 HV. No evidence of carbide segregation was found in R260. In contrast, Mn13 experience microstructural changes that led to a decrease in hardness. Within the thermal pulse, R260 showed no significant difference in hardness when exposed to mechanical impact, whereas Mn13 demonstrated a strong increase in hardness.

- Heating both materials revealed weaknesses in their respective properties. In the case of pearlite, it exhibited high hardness along the surface, resulting in increased brittleness. On the other hand, the presence of carbides in Mn13 led to localised increases in hardness, but this also resulted in unreliable mechanical properties.

- Defects were observed when Mn13 was heated, as confirmed by this study and previous research. The segregation of carbides and the occurrence of common weld defects such as solidification and liquation cracks were observed during the solidification of Mn13. These findings provide evidence of the poor weldability of Mn13.

- R260 formed a WEL upon thermal pulse and rapid cooling, whereas Mn13 did not exhibit any WEL formation during the thermal pulse and rapid cooling.

- Defects became apparent in Mn13 when it was subjected to a thermal pulse, regardless of the manufacturing method used or whether the material had an undeformed or severely deformed surface.

Recommendations for future work:

- In order to obtain validation regarding the phase acquired by Mn13, further investigation is recommended as it was excluded from the current study. The formation of dendritic grains during the welding of Mn13 has been demonstrated in this study and in numerous other studies. To ensure that the material attains the desired properties for its intended application, a more indepth study of the kinetics of dendritic growth in Mn13 could to be carried out.

- Recommendations on the welding process could be found in other studies and in the theory provided by this project in chapter 2. However, information regarding the impact resulting from wheel and rail contact was lacking. The theory established that carbide accumulation and segregation did not occur when the measured temperature was below 300°C. Future research was recommended to explore the specific effects arising from the interaction between wheel and rail and investigate whether carbide segregation and other phenomena were influenced by this contact.

- The execution of the experiments could have been further improved to enhance accuracy, particularly in manual processing. In the case of field tests, automatic settings were employed, resulting in more consistent outcomes. Conversely, for the test bars, manual execution was utilised. It was observed that defects became more pronounced and visible when the experiments were carried out meticulously using automatic settings, which ensured a higher level of uniformity. Furthermore, it should be noted that the field samples were extracted in close proximity to or directly within the center of the thermal pulse. Conversely, the test bars were only taken within the thermal area.

- The SEM analysis provided a clear visualisation of the defects and their characteristics. However, it is important to note that SEM analysis was conducted on a limited number of samples, and it would have been beneficial to examine a larger batch size to detect smaller cracks that may not have been visible through OM. It is worth mentioning that the SEM analysis was exclusively performed on the Mn13 samples and did not provide evidence of the R260 material.

- The etching process on several samples was found to be inadequate, and if sufficient time had been available, it would have been necessary to re-etch them in order to contribute to the conclusions regarding the microstructures.

- Additionally, conducting hardness mapping on both Mn13 and R260 materials would have yielded more comprehensive data on how the hardness profile changed, particularly in relation to whether Mn13 acquired austenitic properties after solidification.

Bibliography

[1] INNOTRACK GUIDELINE. Recommendation of, and scientific basis for, optimisation of switches & crossings–part 2. *Deliverable report D3*, 1, 2006.

[2] Jian-min Li, Mao-fa Jiang, Jun-xiang Ning, and Jun Zhai. Effect of casting speed on dendrite arm spacing of mn13 steel continuous casting slab. *Journal of Iron and Steel Research International*, 27:665–672, 2020.

[3] Johan Ahlström. Residual stresses generated by repeated local heating events–modelling of possible mechanisms for crack initiation. *Wear*, 366:180–187, 2016.

[4] Jun Wu. *Microstructure evolution in pearlitic rail steel due to rail/wheel interaction*. PhD thesis, Delft University of Technology. Department Design Engineering, 2018.

[5] H.W. Zhang, S. Ohsaki, S. Mitao, M. Ohnuma, and K. Hono. Microstructural investigation of white etching layer on pearlite steel rail. *Materials Science and Engineering: A*, 421(1):191–199, 2006. Internal stress and thermo-mechanical behavior in multi-component materials systems, TMS Annual Meeting, 2004.

[6] A. Al-Juboori, H. Zhu, D. Wexler, H. Li, C. Lu, A. McCusker, J. McLeod, S. Pannila, and J. Barnes. Characterisation of white etching layers formed on rails subjected to different traffic conditions. *Wear*, 436-437:202998, 2019.

[7] H.R. Jafarian, M. Sabzi, S.H. Mousavi Anijdan, A.R. Eivani, and N. Park. The influence of austenitization temperature on microstructural developments, mechanical properties, fracture mode and wear mechanism of hadfield high manganese steel. *Journal of Materials Research and Technology*, 10:819–831, 2021.

[8] S Dhar, J Ahlström, X Zhang, HK Danielsen, and D Juul Jensen. Multi-axial fatigue of head-hardened pearlitic and austenitic manganese railway steels: a comparative study. *Metallurgical and Materials Transactions A*, 51:5639–5652, 2020.

[9] Rostyslav Skrypnyk, Magnus Ekh, Jens C.O. Nielsen, and Björn A. Pålsson. Prediction of plastic deformation and wear in railway crossings – comparing the performance of two rail steel grades. *Wear*, 428-429:302–314, 2019.

[10] Wang Kelvin C. P. Zhu Shengyang Zhai, Wanming. 7.2.1.2 kp model, 2022.

[11] Olofsson U. Lewis, R. 3.3.1 introduction, 2009.

[12] Gustavo Tressia and Amilton Sinatora. Effect of the normal load on the sliding wear behavior of hadfield steels. *Wear*, 520:204657, 2023.

[13] David A Porter, Kenneth E Easterling, and Mohamed Y Sherif. *Phase transformations in metals and alloys*. CRC press, 2021.

[14] David A Porter and Kenneth E Easterling. *Phase transformations in metals and alloys (revised reprint)*. CRC press, 2009.

[15] George Krauss. 3.9 diffusion in steel, 2015.

[16] F.C. Campbell. C.2 miller-bravais indices for hexagonal crystal systems, 2008.

[17] Weheba Gamal S. Elshennawy, Ahmad K. 3.1.1 unit cells, 2015.

[18] Honeycombe Robert Bhadeshia, Harry. 1.3 the phase transformation: - and -iron, 2006.

[19] Keith L. Richards. 11.4.7 atomic weight and atomic number, 2018.

[20] Brian Cantor. 1.3 crystal systems, 2020.

[21] Mahmoud Y. Demeri. 9.1.2 stacking faults, 2013.

[22] S. L. Semiatin. ASM International, 2005; 2009.

[23] Jon L. Dossett. 2.3.3 ferrite, 2020.

[24] George Krauss. 5.2 martensitic transformation kinetics, 2015.

[25] J.R. Davis. 10.2.5 martensite, 1998.

[26] Daniel Gren. *Effect of large shear deformation on fatigue crack behavior in pearlitic rail steel.* Chalmers Tekniska Hogskola (Sweden), 2022.

[27] George Krauss. 10.2 continuous cooling transformation diagrams, 2015.

[28] Erika Steyn. *Railway wheel steel behaviour upon thermo-mechanical loadings.* PhD thesis, Department of Industrial and Materials Science, Chalmers University of . . . , 2022.

[29] DK Pal and SK Basu. Hot machining of austenitic manganese steel by shaping. *International Journal of Machine Tool Design and Research*, 11(1):45–61, 1971.

[30] Olofsson U. Lewis, R. 5.4 welding rail, 2009.

[31] Zhimin Ding, Bo Liang, Ruirong Zhao, and Chunhuan Chen. Precipitation of carbides in early aging stages and their crystallographic orientations in hadfield steel mn13. *Metal Science and Heat Treatment*, 57:18–21, 2015.

[32] M.K. Banerjee. 2.8 heat treatment of commercial steels for engineering applications. In MSJ Hashmi, editor, *Comprehensive Materials Finishing*, pages 180–213. Elsevier, Oxford, 2017.

[33] Martin Schilke, Johan Ahlström, and Birger Karlsson. Low cycle fatigue and deformation behaviour of austenitic manganese steel in rolled and in as-cast conditions. *Procedia Engineering*, 2(1):623–628, 2010. Fatigue 2010.

[34] Annette O'Brien. 1.7.3.5 filler metals, 2011.

[35] Lestina Thomas G. Serth, Robert W. 1.2 fourier's law of heat conduction, 2014.

[36] Jones Franklin D. Horton Holbrook L. Ryffel Henry H. Oberg, Erik. Blanking and punching clearance, 2012.

[37] P. K. Mallick. 8.2.3 laser welding, 2021.

[38] Honeycombe Robert Bhadeshia, Harshad. 13.2.1 weld solidification, 2017.

[39] Semiatin S.L. Furrer, D.U. 15.1 approaches to modeling dendritic solidification, 2010.

[40] Enlan Zhao, Haifeng Yang, Yuxing Peng, Lei Wang, Bin Song, Congcong Zhu, and Hao Liu. Microstructure and wear behavior of laser-remelted high-manganese steel. *Journal of Materials Engineering and Performance*, pages 1–10, 2023.

[41] George Krauss. 9.5 solidification - dendrites and interdendritic segregation, 2015.

[42] F.C. Campbell. 5.5 competitive growth of dendrites and eutectics, 2012.

[43] Cahn Robert W. Flemings Merton C. Ilschner Bernhard Kramer Edward J. Mahajan Subhash Buschow, K.H. Jürgen. Microstructure modeling, 2001.

[44] Gildas Guillemot, Oriane Senninger, Christopher A. Hareland, Peter W. Voorhees, and Charles-André Gandin. Thermodynamic coupling in the computation of dendrite growth kinetics for multicomponent alloys. *Calphad*, 77:102429, 2022.

[45] *Hot Cracking*, chapter 3, pages 84–129. John Wiley Sons, Ltd, 2015.

[46] Jasper Ramon, Ritwik Basu, George Vander Voort, and Gururaj Bolar. A comprehensive study on solidification (hot) cracking in austenitic stainless steel welds from a microstructural approach. *International Journal of Pressure Vessels and Piping*, 194:104560, 2021.

[47] Sindo Kou. Solidification and liquation cracking issues in welding. *Jom*, 55:37–42, 2003.

[48] J. Mendez, M. Ghoreshy, W.B.F. Mackay, T.J.N. Smith, and R.W. Smith. Weldability of austenitic manganese steel. *Journal of Materials Processing Technology*, 153-154:596–602, 2004. Proceedings of the International Conference in Advances in Materials and Processing Technologies.

[49] Gitae Park, Seonghoon Jeong, and Changhee Lee. Fusion weldabilities of advanced high manganese steels: a review. *Metals and Materials International*, 27:2046–2058, 2021.

[50] Abdul Faheem Khan, Anwar Manzoor Rana, M Islam, and Tahir Abbas. Microstructural changes in hadfield steel. *Pakistan journal of applied sciences*, 1(3):317–320, 2001.

[51] O. Vargolici, P. Merino, A. Saulot, J. Cavoret, S. Simon, F. Ville, and Y. Berthier. Influence of the initial surface state of bodies in contact on the formation of white etching layers under dry sliding conditions. *Wear*, 366-367:209–216, 2016. Contact Mechanics and Wear of Rail / Wheel Systems, CM2015, August 2015.

[52] Akbar Abrorov, Matluba Kuvoncheva, Ozod Rajabov, Mukhsin Mukhammadov, and Shakhrillo Jumaev. Method of thermal treatment of saw disk teeth of fiber-processing machines by laser quenching. In *IOP Conference Series: Materials Science and Engineering*, volume 862, page 032034. IOP Publishing, 2020.

[53] S. Zitouni, A. Saulot, Samuel Simon, Fabrice Ville, J. Cavoret, Xavier Quost, and Y. Berthier. Mechanical conditions and influence of oxidation on white etching layers formation. *5th World Tribology Congress, WTC 2013*, 3:2197–2200, 01 2014.

[54] Konrad Herrmann. 1.3 interrelationship between material structure and hardness, 2011.

[55] Jones Franklin D. Horton Holbrook L. Ryffel Henry H. Oberg, Erik. Vickers hardness test, 2012.

[56] Adrian P Sutton. 4.4 dislocations, 2021.

[57] Raymond A. Higgins. 4. mechanical deformation and recovery, 1993.

[58] Bill Gunston. Saa, 2009.

[59] Jacob Lubliner. 2.2.1.3 crystal plasticity, 2008.

[60] N/A. slip line, 2012.

[61] Neil Bourne. A.4 plasticity, 2013.
[62] Arthur C. Reardon. 3.2.3 cold working, 2011.
[63] Jerome Mertz. *Introduction to optical microscopy.* Cambridge University Press, 2019.

A

Appendix

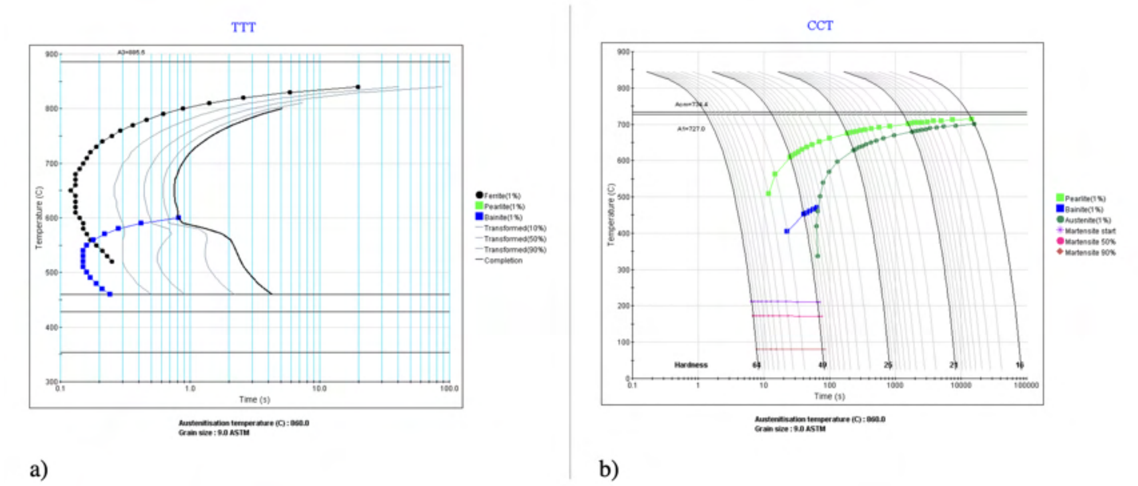

Figure A.1: a) TTT-diagram for R260 b) CTT-diagram for R260 performed in JMatPro software

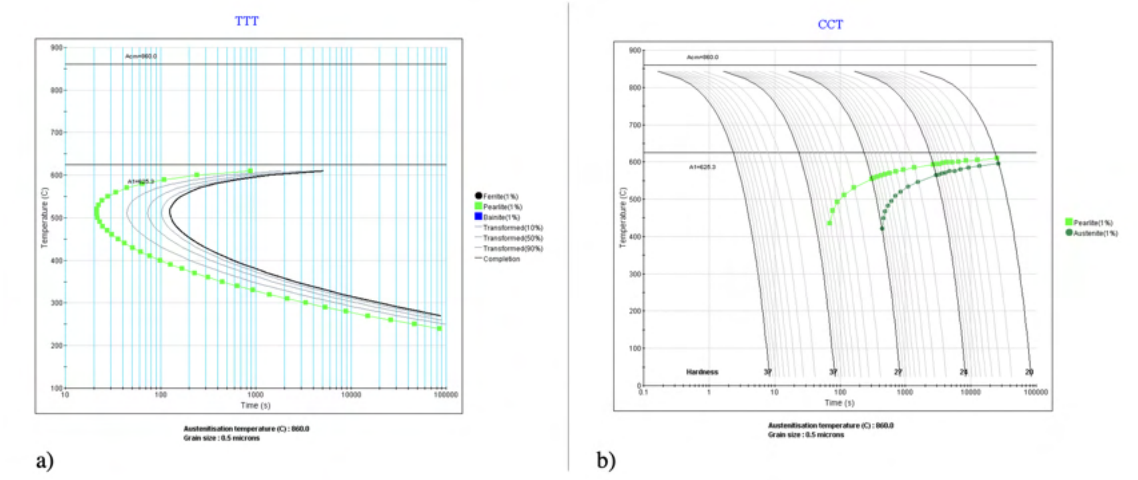

Figure A.2: a) TTT-diagram for Mn13 b) CTT-diagram for Mn13 performed in JMatPro software

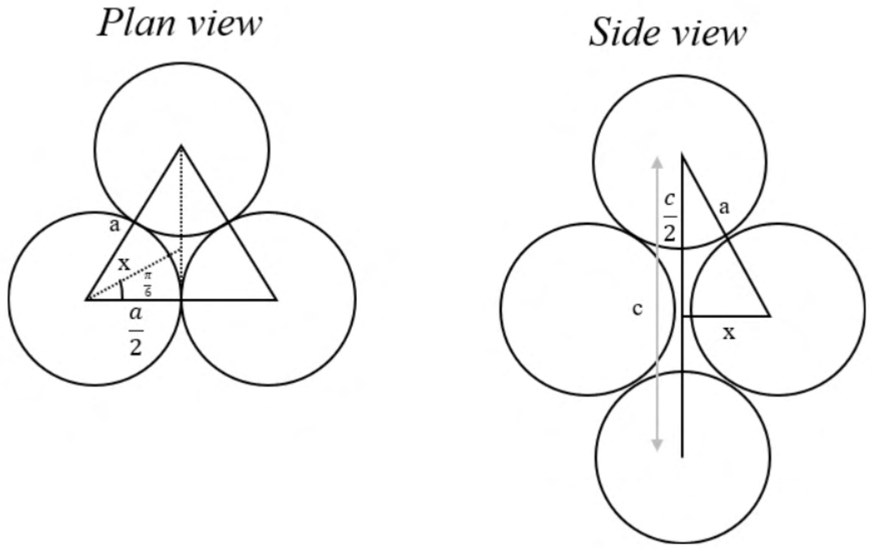

Figure A.3: a) Plan view b) side view of *c/a* value based on HCP crystals

Table A.1: Dimensions and force ratio for each specimen

Material	Specimen number	∅ [mm]	Force$_{\vert 500[Mpa]}$[N]
R260	R1	5.01	9856,8
R260	R2	5.01	9856,8
R260	R3	5.02	9896,2
R260	R4	5.01	9856,8
R260	R5	5.02	9896,2
R260	R6	5.02	9896,2
R260	R7	5.03	9935,6
R260	R8	5.01	9856,8
R260	R9	5.01	9856,8
Mn13	M1	8.03	25321,6
Mn13	M2	8.05	25447,9
Mn13	M3	8.05	25447,9
Mn13	M4	8.05	25447,9
Mn13	M5	8.03	25321,6
Mn13	M6	8.05	25447,9
Mn13	M7	5,08	10134,1
Mn13	M8	6,08	14516,7
Mn13	M9	6,06	14421,3

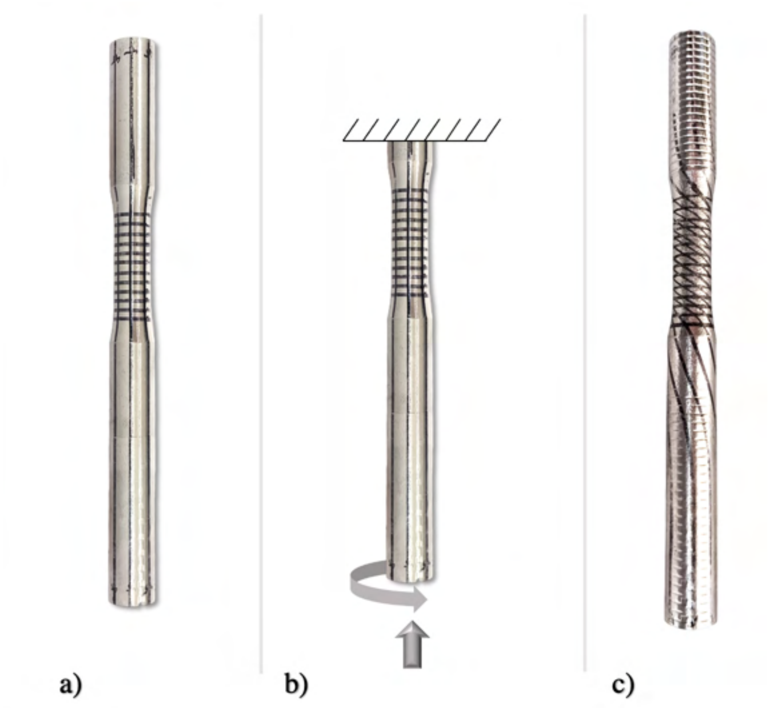

Figure A.4: Methodology of predeformation, a) Before rotation (original grid), b) Forces that are acting on the specimen, c) After rotation (Deformed grid).

B

Appendix B

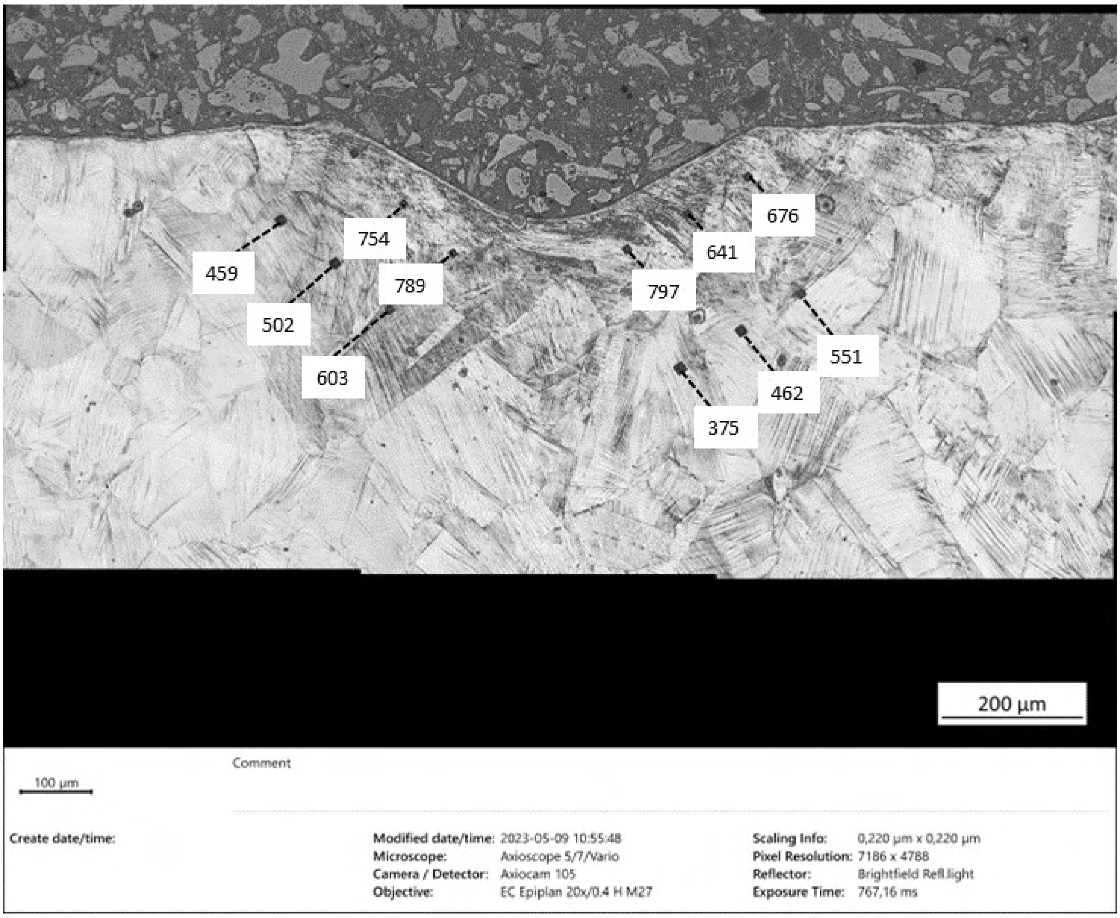

Create date/time:

Modified date/time: 2023-05-09 10:55:48
Microscope: Axioscope 5/7/Vario
Camera / Detector: Axiocam 105
Objective: EC Epiplan 20x/0.4 H M27

Scaling Info: 0,220 µm x 0,220 µm
Pixel Resolution: 7186 x 4788
Reflector: Brightfield Refl.light
Exposure Time: 767,16 ms

Figure B.1: Optical microscope image of Mn13_M5_M$_2$ with microhardness indents visible, specified in HV [0.1]

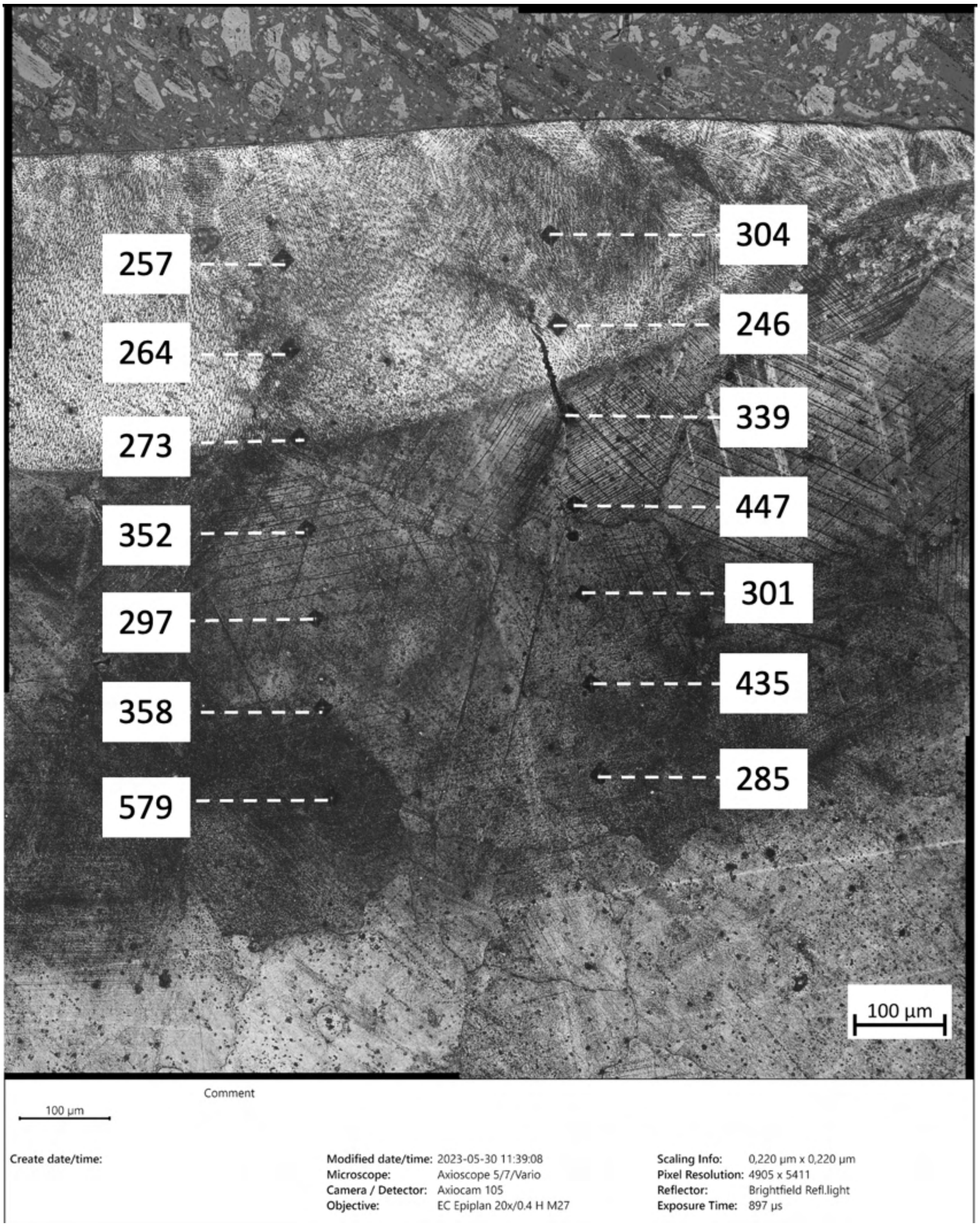

Create date/time:

Modified date/time: 2023-05-30 11:39:08
Microscope: Axioscope 5/7/Vario
Camera / Detector: Axiocam 105
Objective: EC Epiplan 20x/0.4 H M27

Scaling Info: 0,220 µm x 0,220 µm
Pixel Resolution: 4905 x 5411
Reflector: Brightfield Refl.light
Exposure Time: 897 µs

Figure B.2: Optical microscope image of Mn13_F2T_2 with microhardness indents visible, specified in HV [0.1]

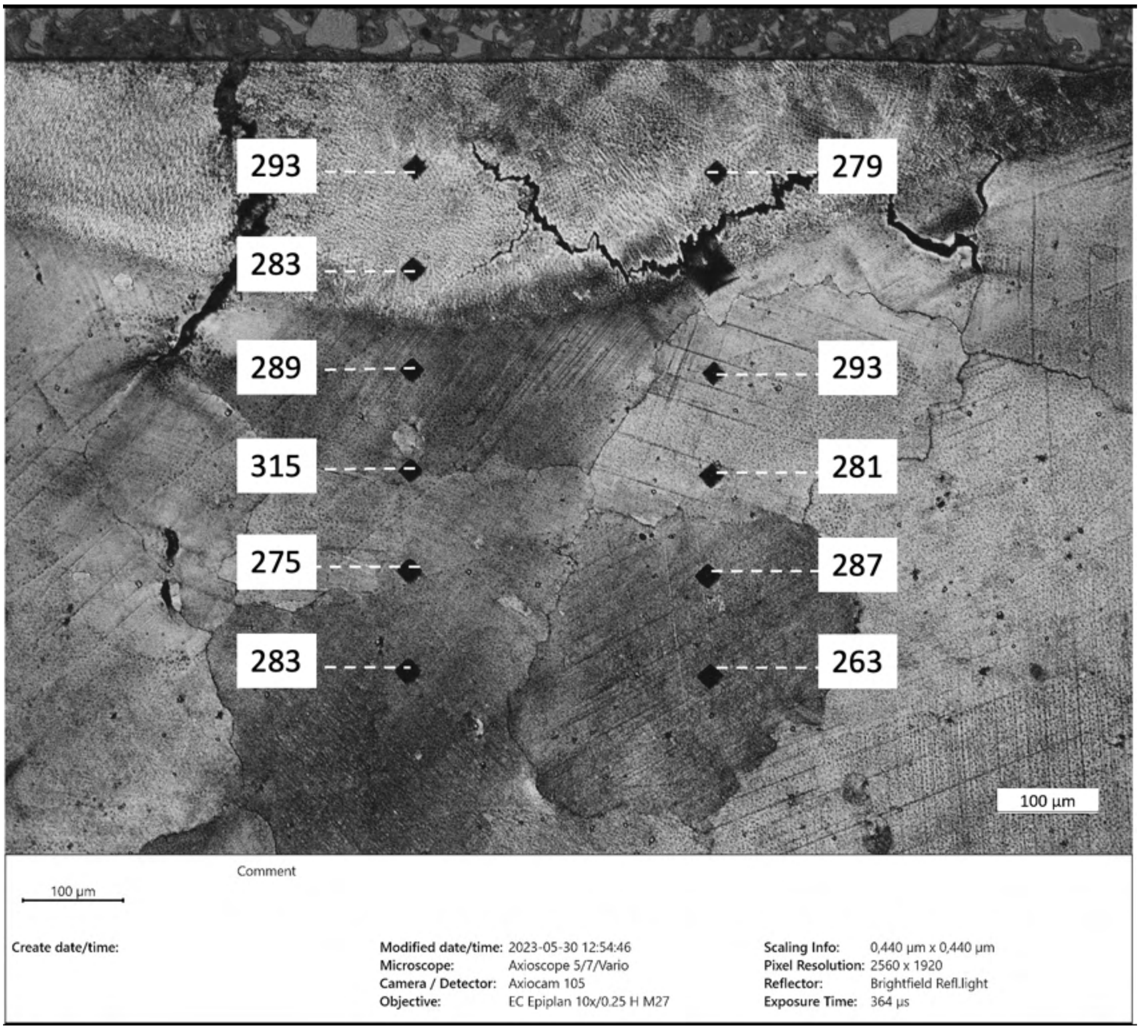

Create date/time:

Modified date/time: 2023-05-30 12:54:46
Microscope: Axioscope 5/7/Vario
Camera / Detector: Axiocam 105
Objective: EC Epiplan 10x/0.25 H M27

Scaling Info: 0,440 µm x 0,440 µm
Pixel Resolution: 2560 x 1920
Reflector: Brightfield Refl.light
Exposure Time: 364 µs

Figure B.3: Optical microscope image of Mn13_F2_M+T_1 with microhardness indents visible, specified in HV [0.1]

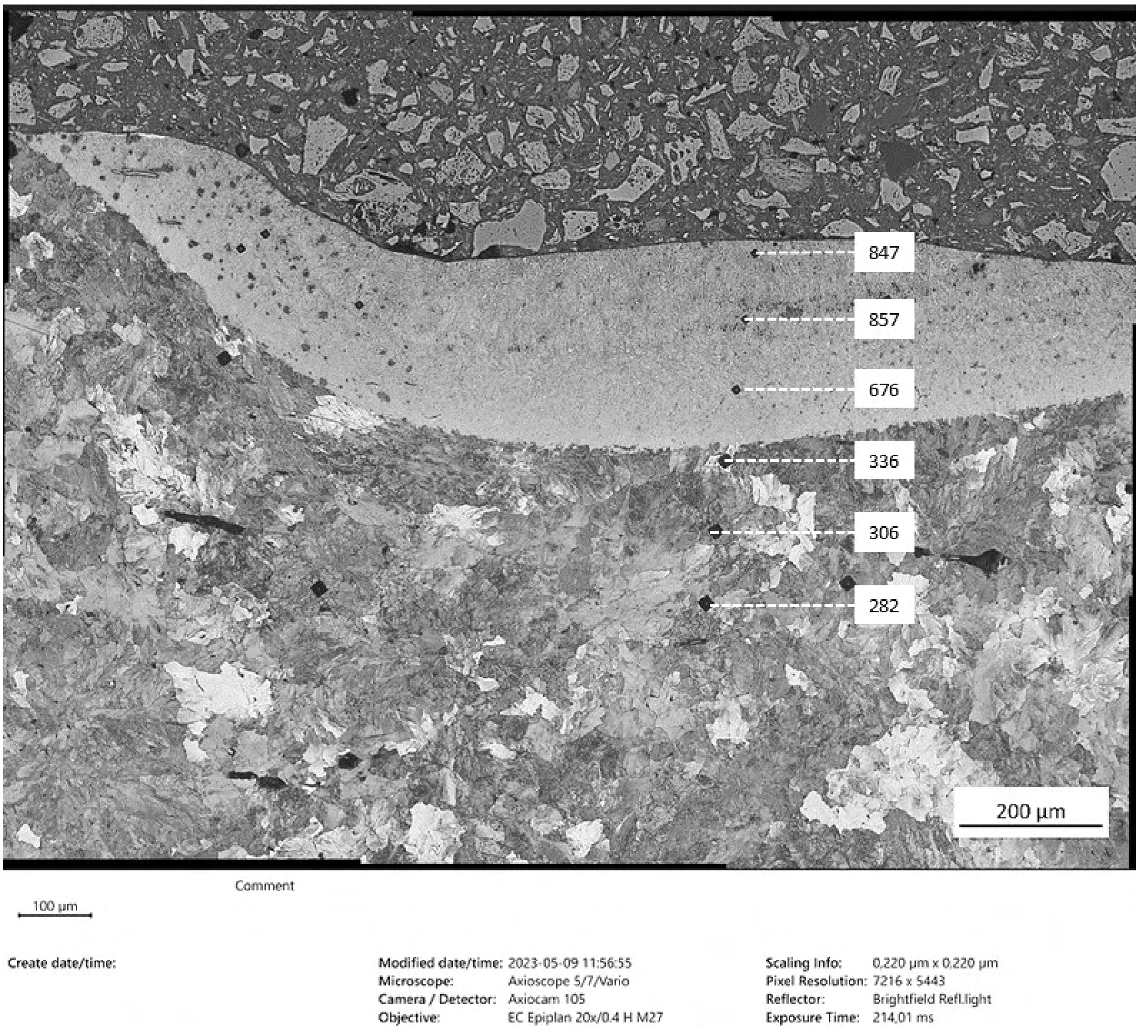

Create date/time:

Modified date/time: 2023-05-09 11:56:55
Microscope: Axioscope 5/7/Vario
Camera / Detector: Axiocam 105
Objective: EC Epiplan 20x/0.4 H M27

Scaling Info: 0,220 µm x 0,220 µm
Pixel Resolution: 7216 x 5443
Reflector: Brightfield Refl.light
Exposure Time: 214,01 ms

Figure B.4: Optical microscope image of R260_R9_V_2 with microhardness indents visible, specified in HV [0.1]

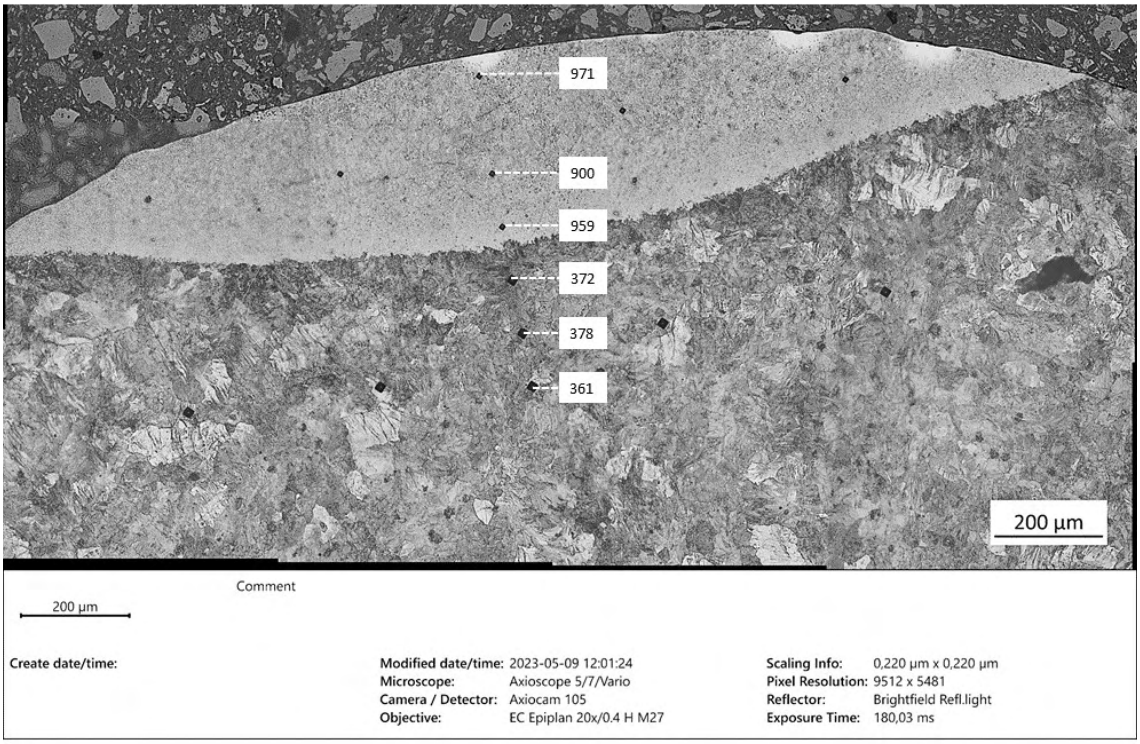

Create date/time:

Modified date/time: 2023-05-09 12:01:24
Microscope: Axioscope 5/7/Vario
Camera / Detector: Axiocam 105
Objective: EC Epiplan 20x/0.4 H M27

Scaling Info: 0,220 µm x 0,220 µm
Pixel Resolution: 9512 x 5481
Reflector: Brightfield Refl.light
Exposure Time: 180,03 ms

Figure B.5: Optical microscope image of R260_R9_T_3 with microhardness indents visible, specified in HV [0.1]

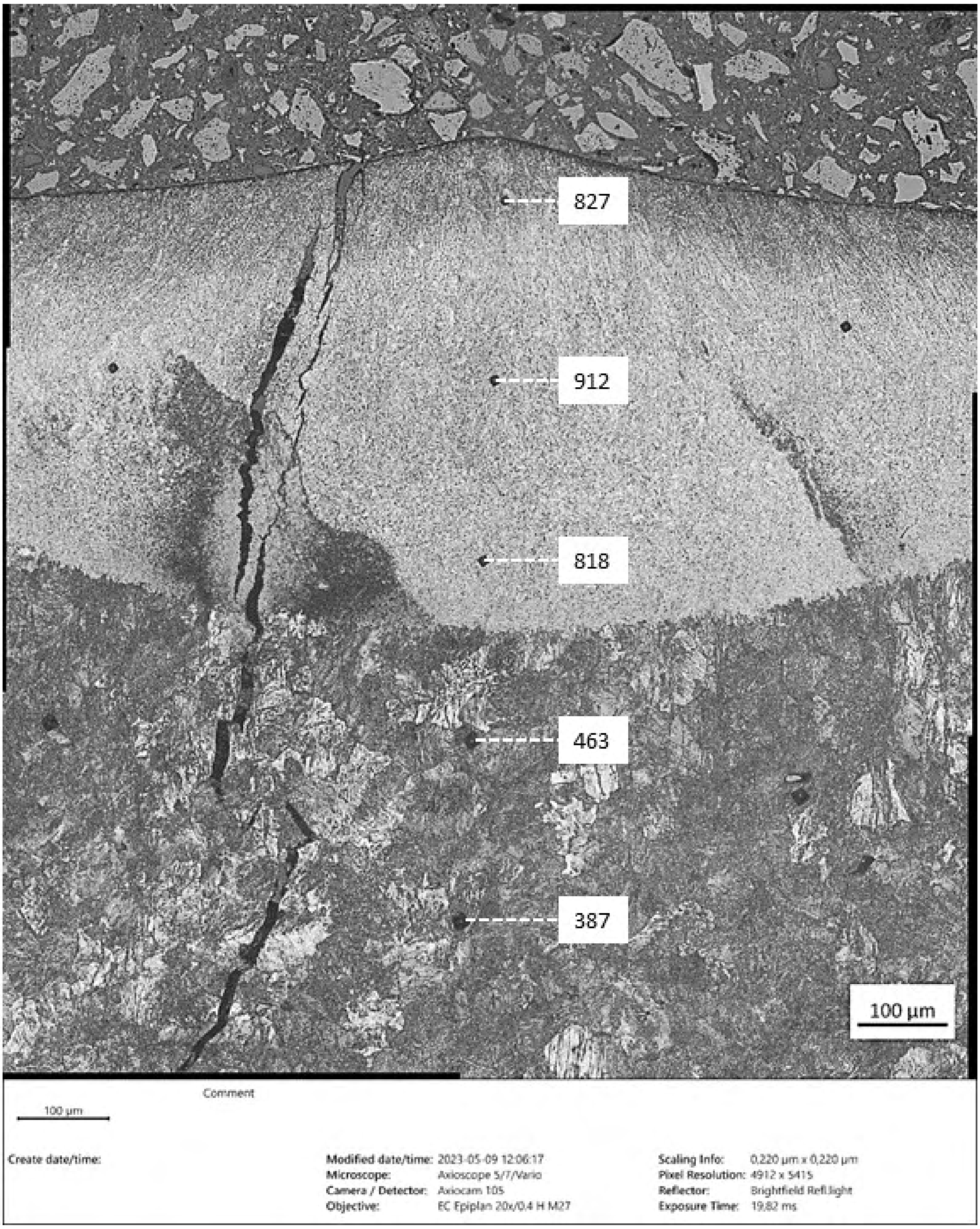

Create date/time:

Modified date/time: 2023-05-09 12:06:17
Microscope: Axioscope 5/7/Vario
Camera / Detector: Axiocam 105
Objective: EC Epiplan 20x/0,4 H M27

Scaling Info: 0,220 µm x 0,220 µm
Pixel Resolution: 4912 x 5415
Reflector: Brightfield Refl.light
Exposure Time: 19,82 ms

Figure B.6: Optical microscope image of R260_R9_T_4 with microhardness indents visible, specified in HV [0.1]

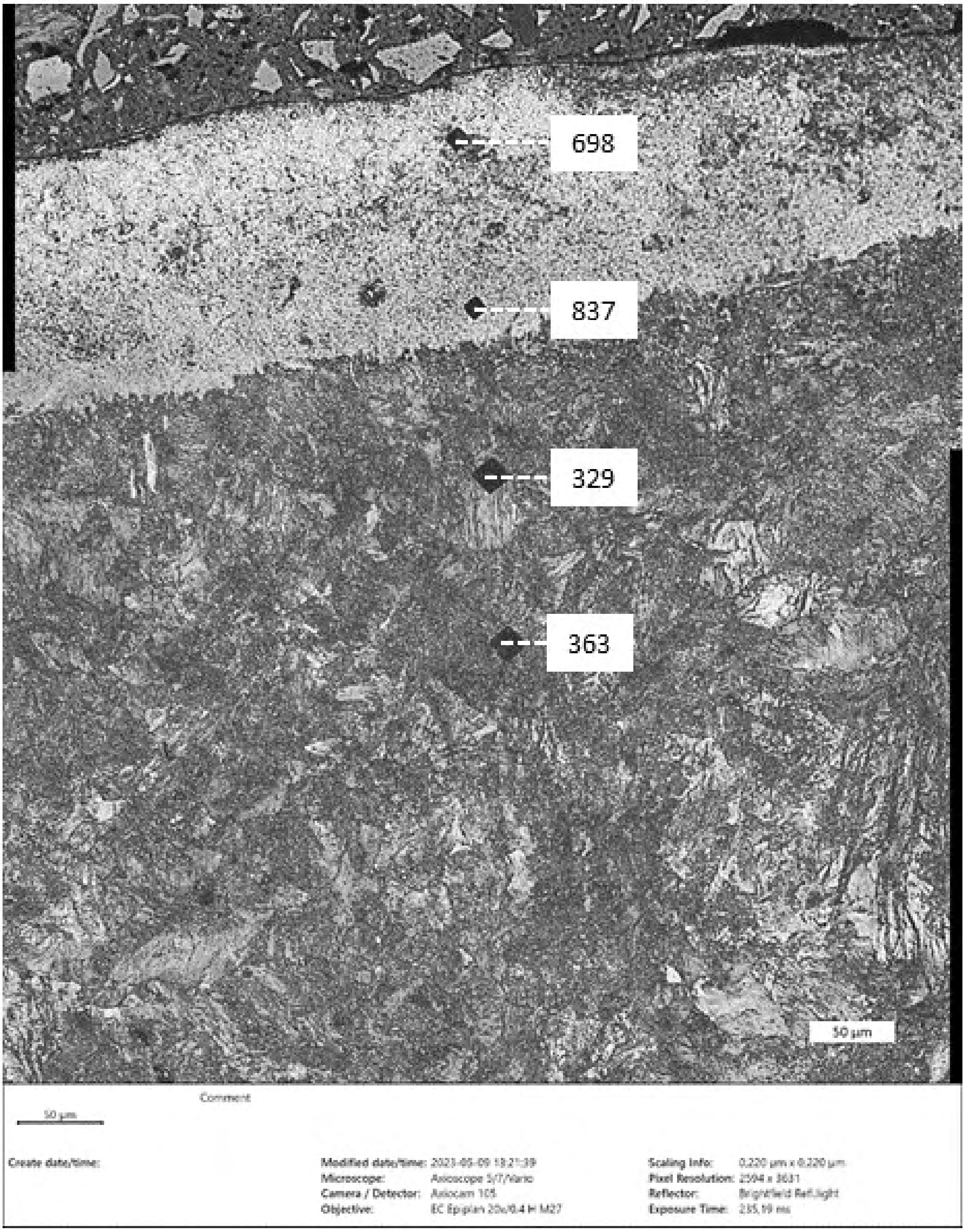

Create date/time:

Modified date/time: 2023-05-09 13:21:39
Microscope: Axioscope 5/7/Vario
Camera / Detector: Axiocam 105
Objective: EC Epiplan 20x/0.4 H M27

Scaling Info: 0.220 µm x 0.220 µm
Pixel Resolution: 2594 x 3631
Reflector: Brightfield Refl.light
Exposure Time: 235.19 ms

Figure B.7: Optical microscope image of R260_R4_T_1 with microhardness indents visible, specified in HV [0.1]

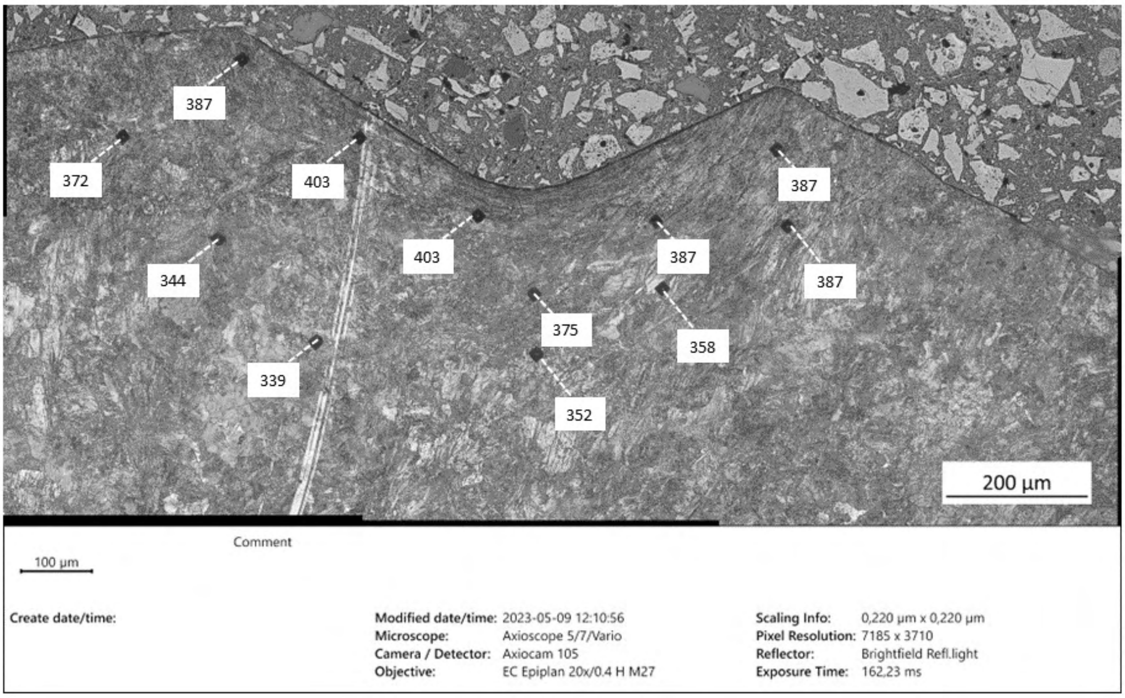

Create date/time:

Modified date/time: 2023-05-09 12:10:56
Microscope: Axioscope 5/7/Vario
Camera / Detector: Axiocam 105
Objective: EC Epiplan 20x/0.4 H M27

Scaling Info: 0,220 µm x 0,220 µm
Pixel Resolution: 7185 x 3710
Reflector: Brightfield Refl.light
Exposure Time: 162,23 ms

Figure B.8: Optical microscope image of R260_R9_M$_1$ with microhardness indents visible, specified in HV [0.1]

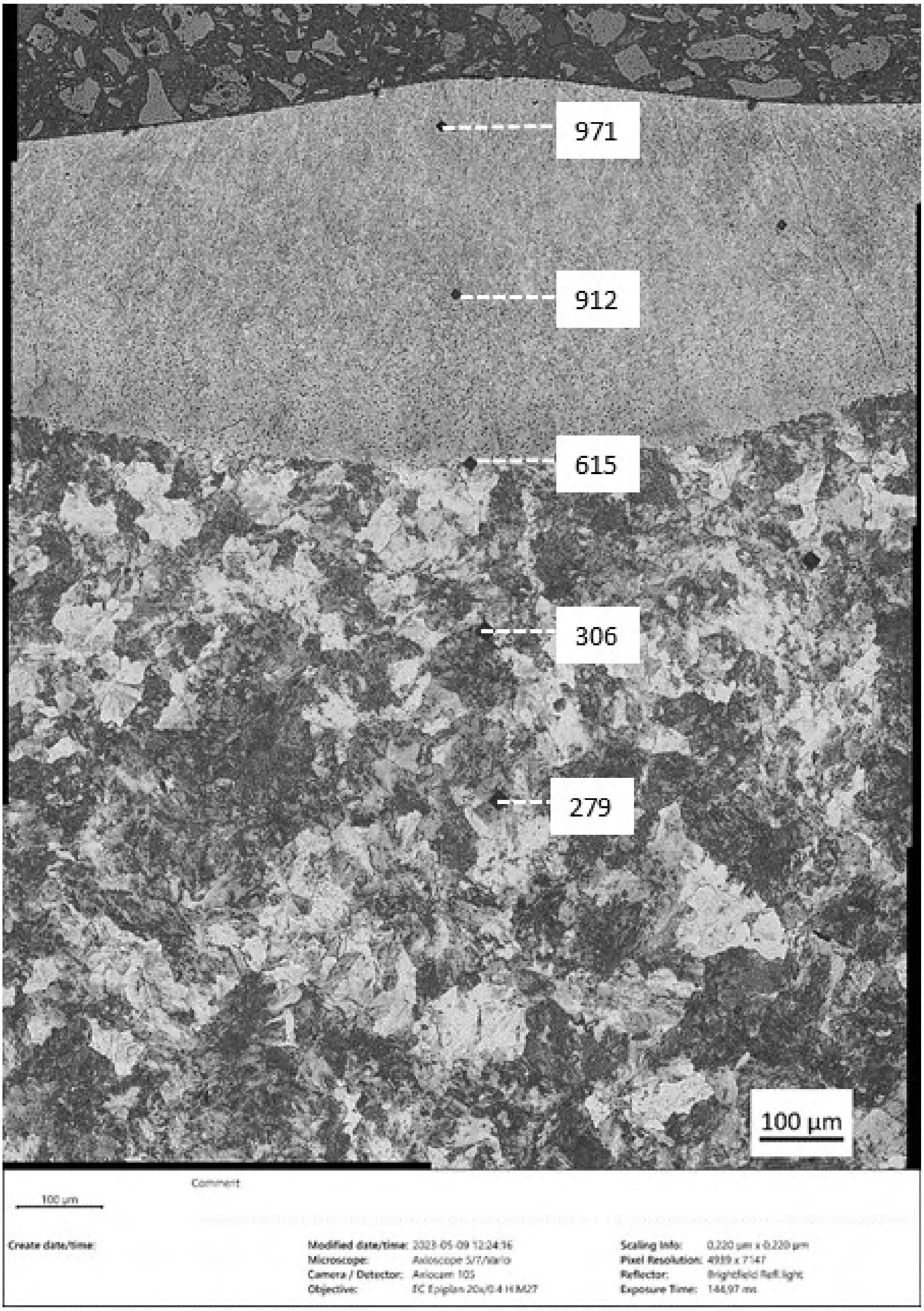

Create date/time:

Modified date/time: 2023-05-09 12:24:16
Microscope: Axioscope 5/7/Vario
Camera / Detector: Axiocam 105
Objective: EC Epiplan 20x/0.4 H M27

Scaling Info: 0,220 µm x 0,220 µm
Pixel Resolution: 4939 x 7147
Reflector: Brightfield Refl.light
Exposure Time: 144,97 ms

Figure B.9: Optical microscope image of R260_Field sample_T_1 with microhardness indents visible, specified in HV [0.1]

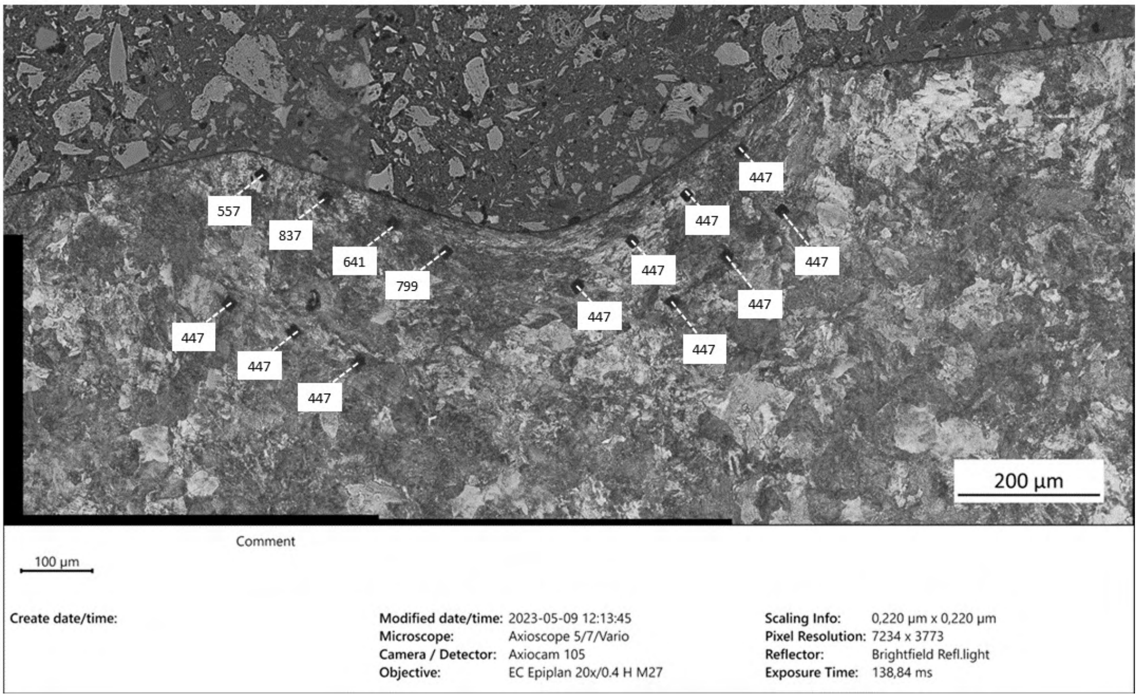

Create date/time:

Modified date/time: 2023-05-09 12:13:45
Microscope: Axioscope 5/7/Vario
Camera / Detector: Axiocam 105
Objective: EC Epiplan 20x/0.4 H M27

Scaling Info: 0,220 µm x 0,220 µm
Pixel Resolution: 7234 x 3773
Reflector: Brightfield Refl.light
Exposure Time: 138,84 ms

Figure B.10: Optical microscope image of R260_Field sample_M_1 with micro-hardness indents visible, specified in HV [0.1]

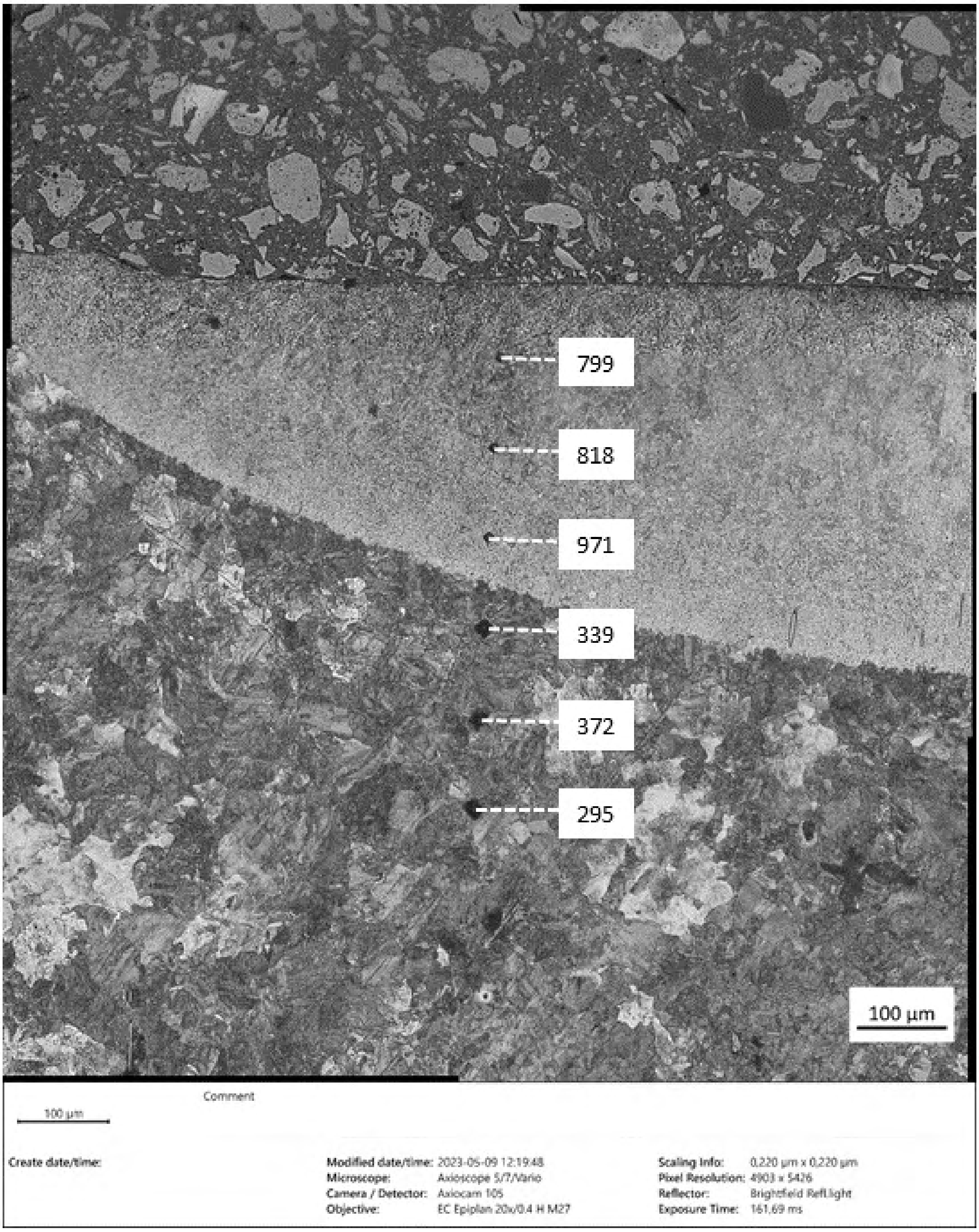

Create date/time:

Modified date/time: 2023-05-09 12:19:48
Microscope: Axioscope 5/7/Vario
Camera / Detector: Axiocam 105
Objective: EC Epiplan 20x/0.4 H M27

Scaling Info: 0,220 µm x 0,220 µm
Pixel Resolution: 4903 x 5426
Reflector: Brightfield Refl.light
Exposure Time: 161,69 ms

Figure B.11: Optical microscope image of R260_Field sample_T+M_1 with microhardness indents visible, specified in HV [0.1]

C

Appendix C

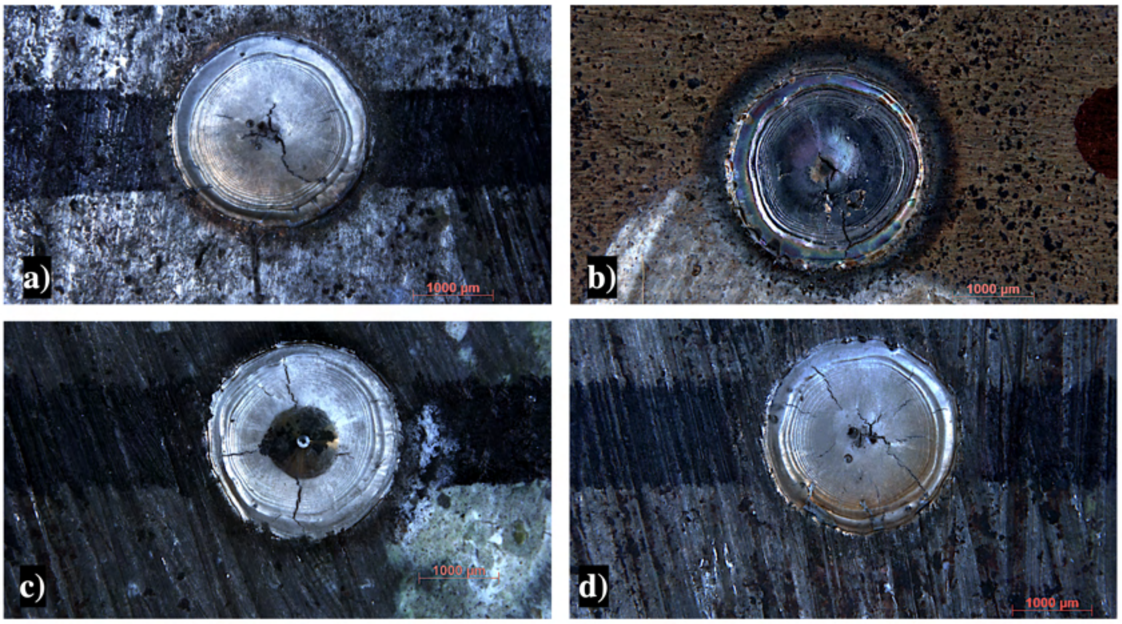

Figure C.1: Presence of surface cracks in the Mn13 field samples

D

Appendix D

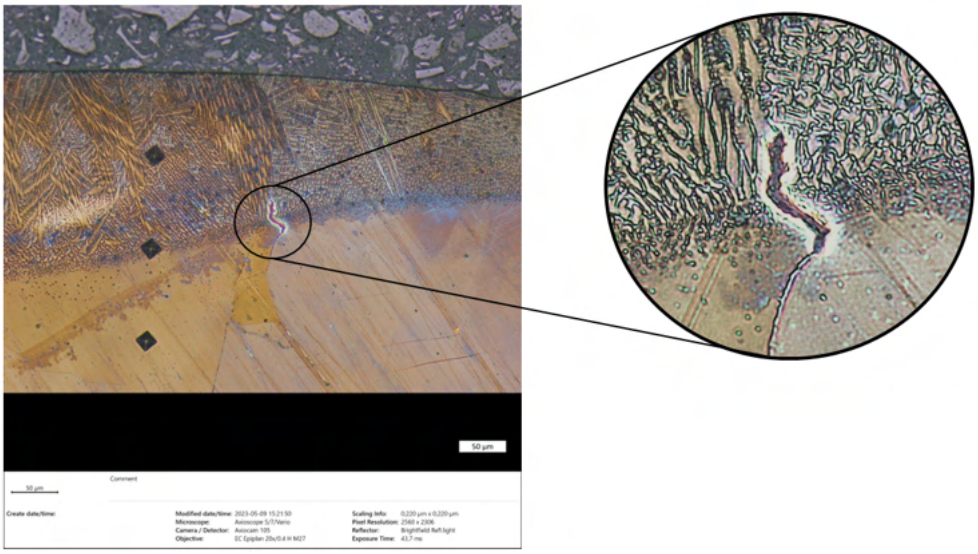

Create date/time:

Modified date/time: 2023-05-09 15:21:50
Microscope: Axioscope 5/7/Vario
Camera / Detector: Axiocam 105
Objective: EC Epiplan 20x/0.4 H M27

Scaling Info: 0,220 µm x 0,220 µm
Pixel Resolution: 2560 x 2306
Reflector: Brightfield Refl.light
Exposure Time: 43,7 ms

Figure D.1: Liquidus crack from Mn13_M5_V1

Create date/time:

Modified date/time: 2023-04-28 11:56:39
Microscope: Axioscope 5/7/Vario
Camera / Detector: Axiocam 105
Objective: EC Epiplan 20x/0.4 H M27

Scaling Info: 0,220 µm x 0,220 µm
Pixel Resolution: 16433 x 3846
Reflector: Brightfield Refl.light
Exposure Time: 59,65 ms

Figure D.2: Microstructure of Mn13_V_2

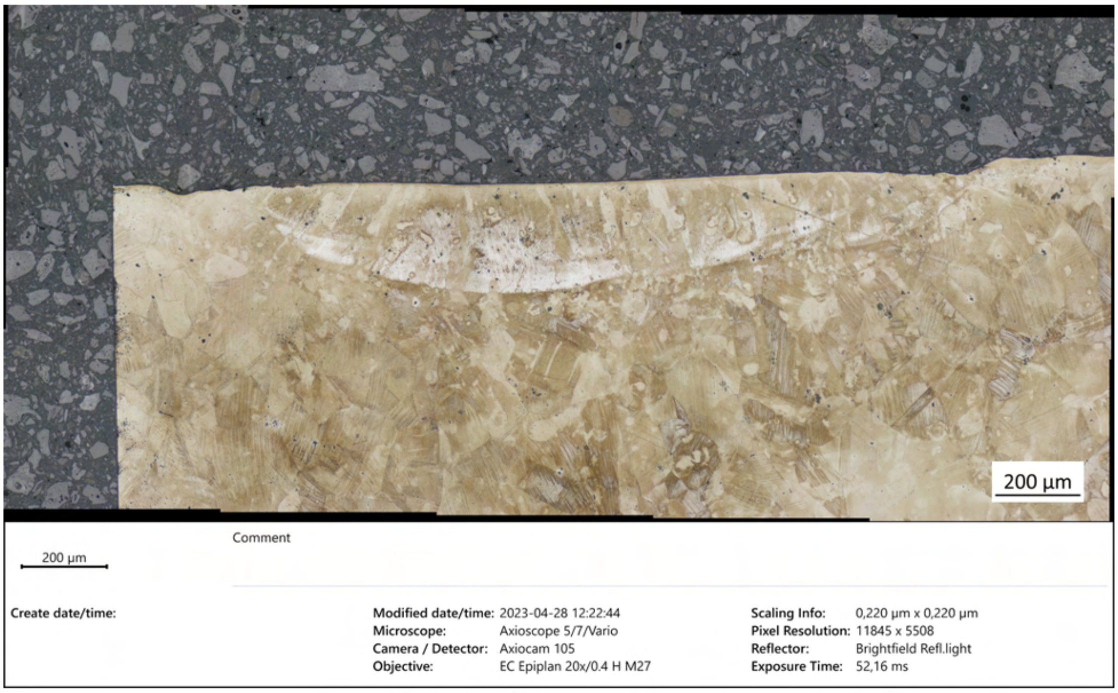

Create date/time:

Modified date/time: 2023-04-28 12:22:44
Microscope: Axioscope 5/7/Vario
Camera / Detector: Axiocam 105
Objective: EC Epiplan 20x/0.4 H M27

Scaling Info: 0,220 µm x 0,220 µm
Pixel Resolution: 11845 x 5508
Reflector: Brightfield Refl.light
Exposure Time: 52,16 ms

Figure D.3: Microstructure of Mn13_T_4

Create date/time:

Modified date/time: 2023-04-28 12:38:17
Microscope: Axioscope 5/7/Vario
Camera / Detector: Axiocam 105
Objective: EC Epiplan 20x/0.4 H M27

Scaling Info: 0,220 µm x 0,220 µm
Pixel Resolution: 16447 x 5578
Reflector: Brightfield Refl.light
Exposure Time: 52,16 ms

Figure D.4: Microstructure of Mn13_M+T_1

Create date/time:

Modified date/time: 2023-04-28 13:06:25
Microscope: Axioscope 5/7/Vario
Camera / Detector: Axiocam 105
Objective: EC Epiplan 20x/0.4 H M27

Scaling Info: 0,220 µm x 0,220 µm
Pixel Resolution: 11842 x 5506
Reflector: Brightfield Refl.light
Exposure Time: 52,16 ms

Figure D.5: Microstructure of Mn13_T_5

Create date/time:

Modified date/time: 2023-04-28 13:28:31
Microscope: Axioscope 5/7/Vario
Camera / Detector: Axiocam 105
Objective: EC Epiplan 20x/0.4 H M27

Scaling Info: 0,220 µm x 0,220 µm
Pixel Resolution: 14134 x 5539
Reflector: Brightfield Refl.light
Exposure Time: 52,02 ms

Figure D.6: Microstructure of Mn13_M+T_2

Create date/time:

Modified date/time: 2023-05-04 11:16:12
Microscope: Axioscope 5/7/Vario
Camera / Detector: Axiocam 105
Objective: EC Epiplan 5x/0.13 H M27

Scaling Info: 0,880 µm x 0,880 µm
Pixel Resolution: 2560 x 1920
Reflector: Brightfield Refl.light
Exposure Time: 119,94 ms

Figure D.7: Microstructure of Mn13_M_1

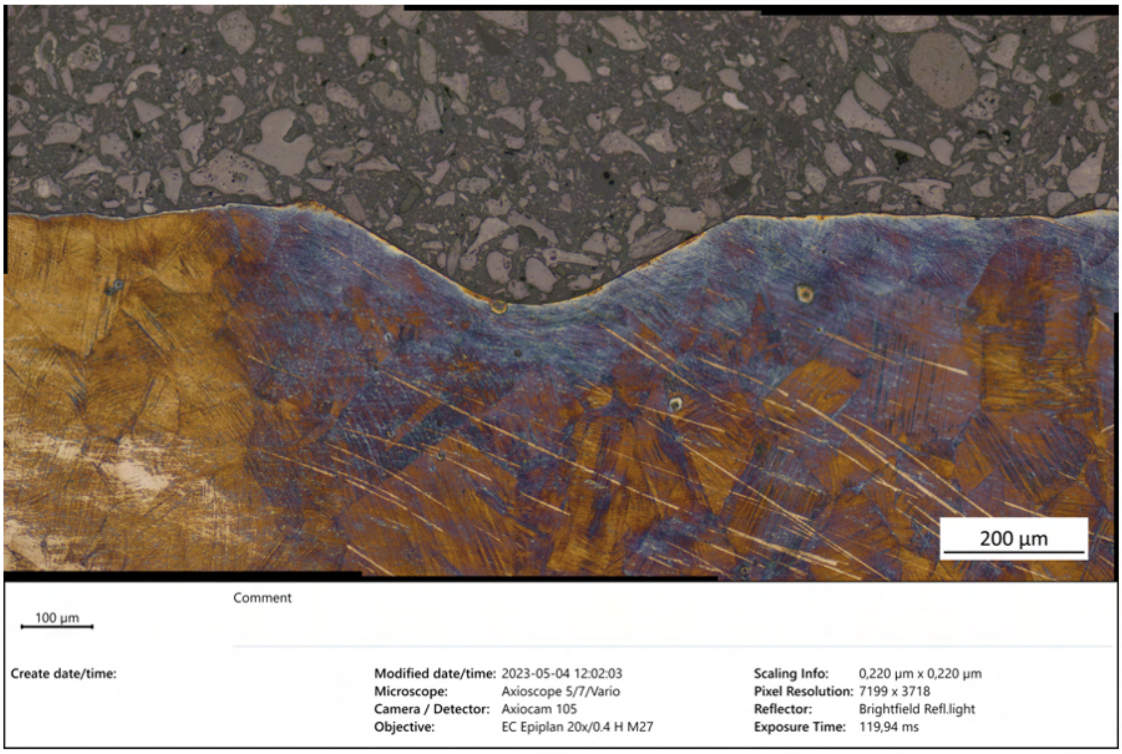

Comment

Create date/time:

Modified date/time: 2023-05-04 12:02:03
Microscope: Axioscope 5/7/Vario
Camera / Detector: Axiocam 105
Objective: EC Epiplan 20x/0.4 H M27

Scaling Info: 0,220 µm x 0,220 µm
Pixel Resolution: 7199 x 3718
Reflector: Brightfield Refl.light
Exposure Time: 119,94 ms

Figure D.8: Microstructure of $Mn13\_M_2$

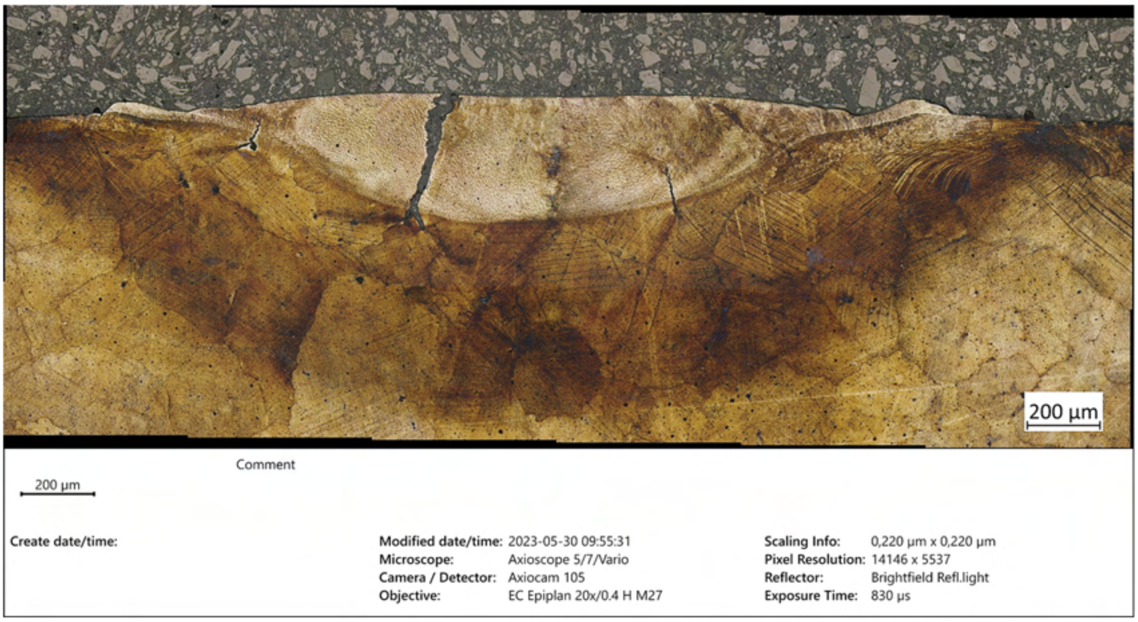

Comment

Create date/time:

Modified date/time: 2023-05-30 09:55:31
Microscope: Axioscope 5/7/Vario
Camera / Detector: Axiocam 105
Objective: EC Epiplan 20x/0.4 H M27

Scaling Info: 0,220 µm x 0,220 µm
Pixel Resolution: 14146 x 5537
Reflector: Brightfield Refl.light
Exposure Time: 830 µs

Figure D.9: Microstructure of $Mn13\_field\ sample\_F_2\_T_1$

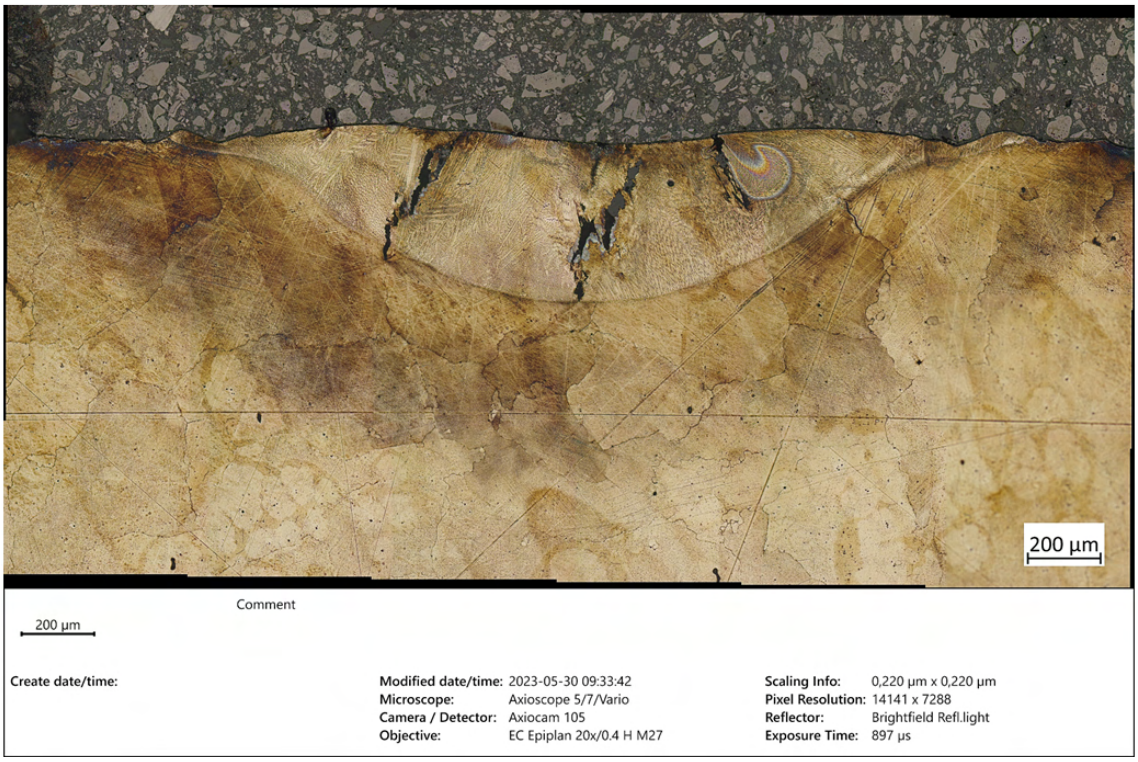

Create date/time:

Modified date/time: 2023-05-30 09:33:42
Microscope: Axioscope 5/7/Vario
Camera / Detector: Axiocam 105
Objective: EC Epiplan 20x/0.4 H M27

Scaling Info: 0,220 µm x 0,220 µm
Pixel Resolution: 14141 x 7288
Reflector: Brightfield Refl.light
Exposure Time: 897 µs

Figure D.10: Microstructure of Mn13_field sample_F_2T_2

Create date/time:

Modified date/time: 2023-05-30 10:40:52
Microscope: Axioscope 5/7/Vario
Camera / Detector: Axiocam 105
Objective: EC Epiplan 20x/0.4 H M27

Scaling Info: 0,220 µm x 0,220 µm
Pixel Resolution: 18655 x 5551
Reflector: Brightfield Refl.light
Exposure Time: 830 µs

Figure D.11: Microstructure of Mn13_field sample _F_2T_3

Comment

Create date/time:

Modified date/time: 2023-05-30 10:59:58
Microscope: Axioscope 5/7/Vario
Camera / Detector: Axiocam 105
Objective: EC Epiplan 20x/0.4 H M27

Scaling Info: 0,220 µm x 0,220 µm
Pixel Resolution: 16422 x 3840
Reflector: Brightfield Refl.light
Exposure Time: 697 µs

Figure D.12: Microstructure of Mn13_field sample _F_2_T+M_1, but mechanical indent is not visible

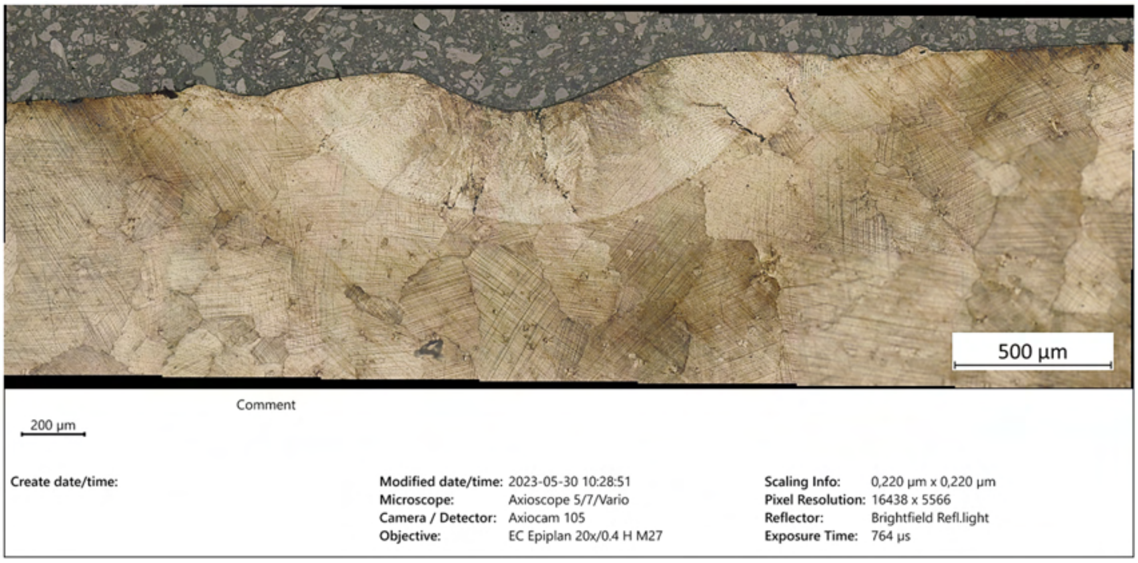

Comment

Create date/time:

Modified date/time: 2023-05-30 10:28:51
Microscope: Axioscope 5/7/Vario
Camera / Detector: Axiocam 105
Objective: EC Epiplan 20x/0.4 H M27

Scaling Info: 0,220 µm x 0,220 µm
Pixel Resolution: 16438 x 5566
Reflector: Brightfield Refl.light
Exposure Time: 764 µs

Figure D.13: Microstructure of Mn13_field sample _F_1_T+M_1

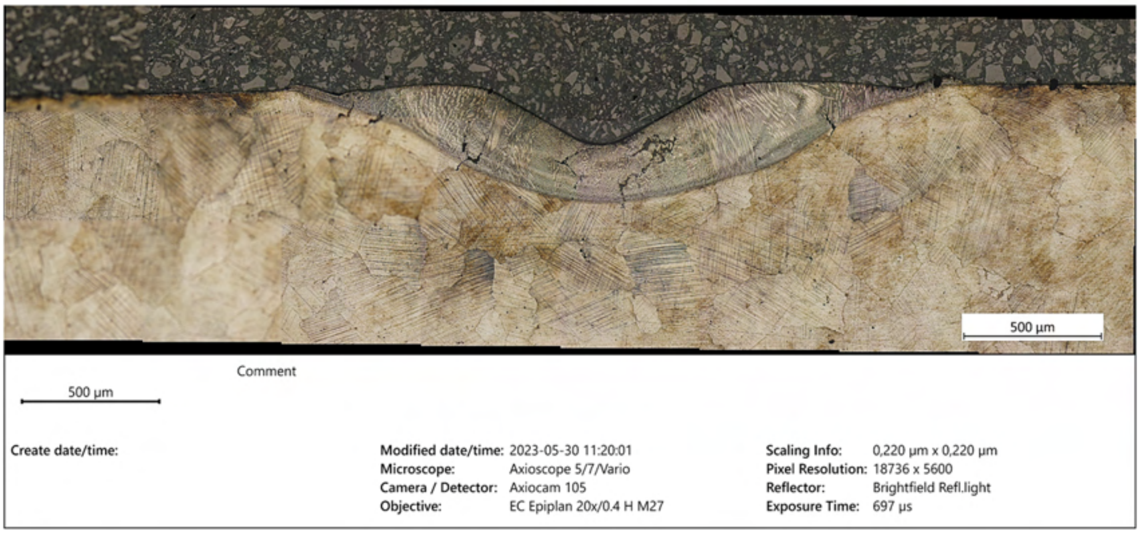

Create date/time:

Modified date/time: 2023-05-30 11:20:01
Microscope: Axioscope 5/7/Vario
Camera / Detector: Axiocam 105
Objective: EC Epiplan 20x/0.4 H M27

Scaling Info: 0,220 µm x 0,220 µm
Pixel Resolution: 18736 x 5600
Reflector: Brightfield Refl.light
Exposure Time: 697 µs

Figure D.14: Microstructure of Mn13_field sample _F_2_T+M_2

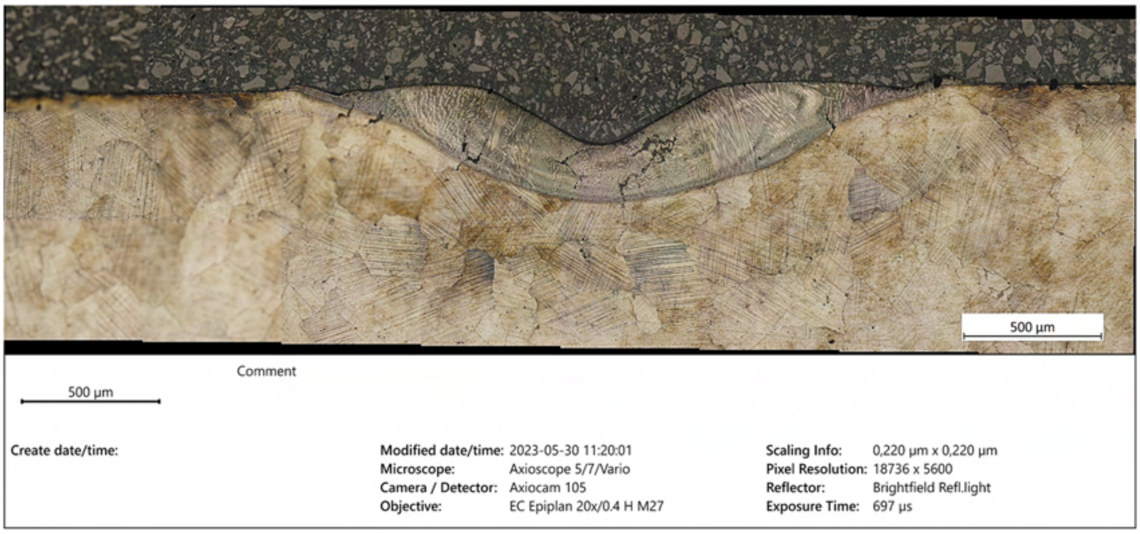

Create date/time:

Modified date/time: 2023-05-30 11:20:01
Microscope: Axioscope 5/7/Vario
Camera / Detector: Axiocam 105
Objective: EC Epiplan 20x/0.4 H M27

Scaling Info: 0,220 µm x 0,220 µm
Pixel Resolution: 18736 x 5600
Reflector: Brightfield Refl.light
Exposure Time: 697 µs

Figure D.15: Microstructure of Mn13_field sample _F_2_T+M_3

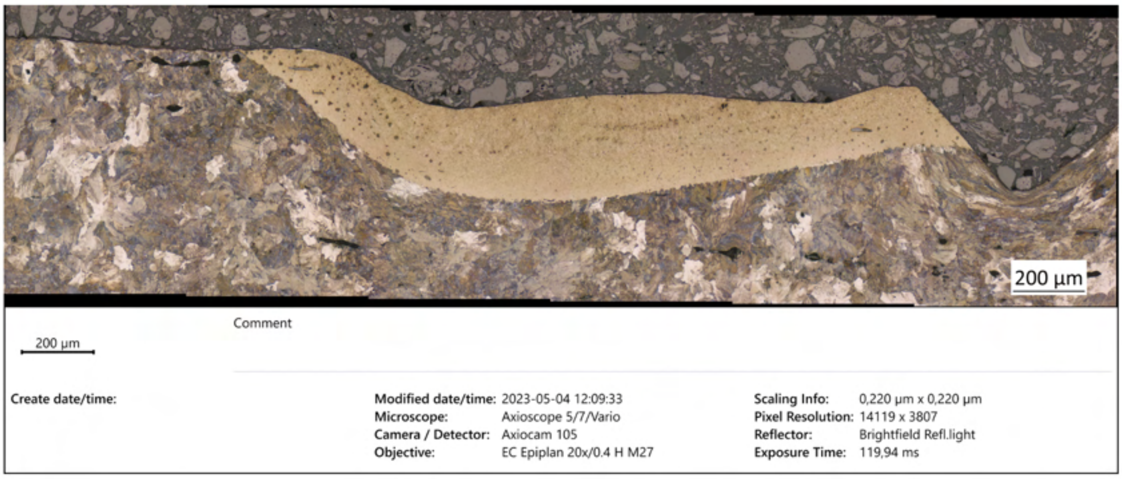

Comment

Create date/time:

Modified date/time: 2023-05-04 12:09:33
Microscope: Axioscope 5/7/Vario
Camera / Detector: Axiocam 105
Objective: EC Epiplan 20x/0.4 H M27

Scaling Info: 0,220 µm x 0,220 µm
Pixel Resolution: 14119 x 3807
Reflector: Brightfield Refl.light
Exposure Time: 119,94 ms

Figure D.16: Microstructure of R260_V_2

Comment

Create date/time:

Modified date/time: 2023-04-28 14:55:44
Microscope: Axioscope 5/7/Vario
Camera / Detector: Axiocam 105
Objective: EC Epiplan 20x/0.4 H M27

Scaling Info: 0,220 µm x 0,220 µm
Pixel Resolution: 25714 x 7432
Reflector: Brightfield Refl.light
Exposure Time: 100,02 ms

Figure D.17: Microstructure of R260_R9_T_4

Comment

Create date/time:

Modified date/time: 2023-04-28 15:14:17
Microscope: Axioscope 5/7/Vario
Camera / Detector: Axiocam 105
Objective: EC Epiplan 20x/0.4 H M27

Scaling Info: 0,220 µm x 0,220 µm
Pixel Resolution: 11808 x 3773
Reflector: Brightfield Refl.light
Exposure Time: 100,02 ms

Figure D.18: Microstructure of R260_R4_T_1

Comment

Create date/time:

Modified date/time: 2023-04-28 15:08:15
Microscope: Axioscope 5/7/Vario
Camera / Detector: Axiocam 105
Objective: EC Epiplan 20x/0.4 H M27

Scaling Info: 0,220 µm x 0,220 µm
Pixel Resolution: 11799 x 3782
Reflector: Brightfield Refl.light
Exposure Time: 100,02 ms

Figure D.19: Microstructure of R260_R4_M_1

Comment

date/time:

Modified date/time: 2023-04-28 15:43:47
Microscope: Axioscope 5/7/Vario
Camera / Detector: Axiocam 105
Objective: EC Epiplan 20x/0.4 H M27

Scaling Info: 0,220 µm x 0,220 µm
Pixel Resolution: 16444 x 5559
Reflector: Brightfield Refl.light
Exposure Time: 100,02 ms

Figure D.20: Microstructure of R260_Field sample_T+M_1

Comment

Create date/time:

Modified date/time: 2023-04-28 15:20:11
Microscope: Axioscope 5/7/Vario
Camera / Detector: Axiocam 105
Objective: EC Epiplan 20x/0.4 H M27

Scaling Info: 0,220 µm x 0,220 µm
Pixel Resolution: 16438 x 5573
Reflector: Brightfield Refl.light
Exposure Time: 100,02 ms

Figure D.21: Microstructure of R260_Field sample_T_1

Comment

Create date/time:

Modified date/time: 2023-04-28 15:22:42
Microscope: Axioscope 5/7/Vario
Camera / Detector: Axiocam 105
Objective: EC Epiplan 5x/0.13 H M27

Scaling Info: 0,880 µm x 0,880 µm
Pixel Resolution: 2560 x 1920
Reflector: Brightfield Refl.light
Exposure Time: 100,02 ms

Figure D.22: Microstructure of R260_Field sample_M_1